



## Evaluating the Accuracy of Hybrid Finite Element/Particle-In-Cell Methods for Modeling Incompressible Stokes Flow

Journal:	<i>Geophysical Journal International</i>
Manuscript ID	GJI-19-0141.R1
Manuscript Type:	Research Paper
Date Submitted by the Author:	24-Jun-2019
Complete List of Authors:	Gassmüller, Rene; University of California, Davis, Department of Earth and Planetary Sciences Lokavarapu, Harsha; University of California Davis, Department of Earth and Planetary Sciences Bangerth, Wolfgang; Colorado State University, Department of Mathematics Puckett, Elbridge; University of California Davis, Department of Mathematics
Keywords:	Numerical approximations and analysis < GEOPHYSICAL METHODS, Numerical solutions < GEOPHYSICAL METHODS, Numerical modelling < GEOPHYSICAL METHODS, Dynamics of lithosphere and mantle < TECTONOPHYSICS, Mantle processes < GENERAL SUBJECTS

submitted to *Geophys. J. Int.*

# Evaluating the Accuracy of Hybrid Finite Element/Particle-In-Cell Methods for Modeling Incompressible Stokes Flow

Rene Gassmöller<sup>1,\*</sup>

Harsha Lokavarapu<sup>1</sup>

Wolfgang Bangerth<sup>2</sup>

Elbridge Gerry Puckett<sup>3</sup>

<sup>1</sup> *Department of Earth and Planetary Science, U. C. Davis, Davis, CA 95616, USA.*

<sup>2</sup> *Department of Mathematics, Colorado State University, Fort Collins, CO 80523, USA.*

<sup>3</sup> *Department of Mathematics, U. C. Davis, Davis, CA 95616, USA.*

\* *Corresponding author.*

## SUMMARY

Combining finite element methods for the incompressible Stokes equations with particle-in-cell methods is an important technique in computational geodynamics that has been widely applied in mantle convection, lithosphere dynamics, and crustal-scale modeling. In these applications, particles are used to transport along properties of the medium such as the temperature, chemical compositions, or other material properties; the particle methods are therefore used to reduce the advection equation to an ordinary differential equation for each particle, resulting in a problem that is simpler to solve than the original equation for which stabilization techniques are necessary to avoid oscillations.

On the other hand, replacing field-based descriptions by quantities only defined at

1  
2  
3  
4 2 *R. Gassmüller, H. Lokavarapu, W. Bangerth, E. G. Puckett*

5 the locations of particles introduces numerical errors. These errors have previously  
6 been investigated, but a complete understanding from both the theoretical and prac-  
7 tical sides was so far lacking. In addition, we are not aware of systematic guidance  
8 regarding the question of how many particles one needs to choose per mesh cell to  
9 achieve a certain accuracy.  
10

11 In this paper we modify two existing instantaneous benchmarks and present a new  
12 analytic benchmark for time-dependent incompressible Stokes flow in order to com-  
13 pare the convergence rate and accuracy of various combinations of finite element,  
14 particle advection, and particle interpolation methods. Using these benchmarks, we  
15 find that in order to retain the optimal accuracy of the finite element formulation,  
16 one needs to use a sufficiently accurate particle interpolation algorithm. Addition-  
17 ally, we observe and explain that for our higher-order finite-element methods it is  
18 necessary to increase the number of particles per cell as the mesh resolution increases  
19 (i.e., as the grid cell size decreases) to avoid a reduction in convergence order.  
20  
21

22 Our methods and results allow designing new particle-in-cell methods with specific  
23 convergence rates, and also provide guidance for the choice of common building  
24 blocks and parameters such as the number of particles per cell. In addition, our new  
25 time-dependent benchmark provides a simple test that can be used to compare dif-  
26 ferent implementations, algorithms, and for the assessment of new numerical meth-  
27 ods for particle interpolation and advection. We provide a reference implementation  
28 of this benchmark in ASPECT (the “Advanced Solver for Problems in Earth’s  
29 ConvecTion”), an open source code for geodynamic modeling.  
30  
31

32 **Key words:** Numerical approximations and analysis, Numerical solutions, Numer-  
33 ical modelling, Dynamics of lithosphere and mantle, Mantle processes  
34  
35  
36  
37  
38  
39  
40  
41  
42  
43  
44  
45  
46  
47

## 48 1 INTRODUCTION

49 Computational geodynamic models are important tools to understand the dynamic processes  
50 observed in the solid Earth; for example, to model mantle convection, lithosphere dynam-  
51 ics, and crustal deformation. Most of these models involve solving the Stokes equations with  
52  
53  
54  
55  
56  
57  
58  
59  
60

*Evaluating hybrid finite element mesh/particle-in-cell methods* 3

variable rock properties (such as viscosity and density) for the velocity and pressure. These equations are then coupled to the time evolution of an advection-diffusion equation for the temperature, and, more generally, the advection of additional quantities that influence rock properties, such as chemical composition [McNamara & Zhong(2005), Tackley(1998), Dannberg & Gassmüller(2018)], grain size [Rozel et al.(2011), Thielmann et al.(2015), Dannberg et al.(2017), Mulyukova & Bercovici(2018)], or melt fraction and depletion [Fischer & Gerya(2016), Gassmüller et al.(2016)].

Consequently, a number of different techniques, with various advantages and disadvantages, have been developed to solve advection or advection-diffusion equations. Among these are techniques that directly solve the advection equations using stabilized finite element or finite difference methods [Brooks & Hughes(1982), Guermond & Pasquetti(2011), Kronbichler et al.(2012)], volume-of-fluid methods [Hirt & Nichols(1981)], but notably also ones in which “particles” are used to describe the motion of the material with its associated properties. Among these latter methods are particle-in-cell or marker-and-cell methods [Evans et al.(1957), Harlow & Welch(1965)], and interface tracking methods such as marker-chain [Poliakov & Podladchikov(1992)]. For a recent comparison see [Puckett et al.(2017)].

Particle-in-cell (PIC) methods in particular have been widely used for geodynamic computations [Tackley & King(2003), Moresi et al.(2003), Gerya & Yuen(2003), McNamara & Zhong(2004), Popov & Sobolev(2008), Samuel(2018)], since they are conceptually simple and do not require specialized algorithms or other techniques to stabilize the solution of the strongly advection-dominated equation. In PIC or related methods, the advected property is transported on a set of discrete particles that are advected with the flow. Since each particle’s movement is independent of all of the other particles, this converts the partial differential equation for the advection of the quantity or quantities carried by the particles into a set of ordinary differential equations for each particle’s location and, possibly, the evolution of the quantity. When the particles’ properties are required for the solution of the Stokes equations for the next time step, they are interpolated or projected back onto the discrete grid. After the Stokes solve, the locations and properties of the particles are updated, e.g. by interpolating the newly computed solution or an appropriately determined update back onto the particles.

Despite the long history of researchers using PIC methods in geodynamic codes, many challenges continue to exist in the implementation and application of these methods. Among these are that PIC methods are difficult to combine with adaptively refined and dynamically changing meshes, since the number of particles per cell may vary widely during a computation and the numerical error and convergence properties of the method are difficult to determine

1  
2  
3  
4 *R. Gassmüller, H. Lokavarapu, W. Bangerth, E. G. Puckett*

5  
6 precisely (see also [Gassmüller et al.(2018)]). At a more fundamental level, we are not aware  
7 of a systematic study that considers the different contributions to the overall numerical error  
8 in a PIC scheme. The excellent paper by Thielmann, May, and Kaus [Thielmann et al.(2014)]  
9 provides many answers in this regard, but leaves open others that relate, in particular, to the  
10 question of what convergence orders one can expect in time-dependent Stokes flow, and when  
11 appropriately varying the number of particles per cell. A separate recent study by Samuel  
12 (see [Samuel(2018)]) is concerned with improvements of the PIC method for time-dependent  
13 shear flow and reducing the required number of particles, but does not quantify the influence  
14 of the accumulated particle error on the Stokes solution. We therefore consider the current  
15 study an extension of [Thielmann et al.(2014)] in which we provide both a theoretical analysis  
16 and numerical evidence that support each other, and complementary to [Samuel(2018)] in  
17 that we investigate the particle error contributions on time-dependent flow.  
18  
19

20  
21 Specifically, we quantitatively determine the accuracy of particle-in-cell methods cou-  
22 pled to finite element-based Stokes solvers in order to untangle the influence of the following  
23 building blocks of PIC methods on the accuracy of the solution: (1) the number and dis-  
24 tribution of particles, (2) the interpolation of particle-based properties to field-based prop-  
25 erties, and (3) the integration of the motion of the particles over time. In order to achieve  
26 this we start by reproducing the instantaneous benchmark results SolCx and SolKz [Duretz  
27 et al.(2011), Zhong(1996)], and discuss how the convergence rate of the computed solution  
28 depends on different finite element and interpolation algorithm combinations. Our numeri-  
29 cal results generally reproduce our theoretical predictions and demonstrate that in order to  
30 recover the intrinsic convergence rate of a given finite element, we need both a sufficiently  
31 accurate particle interpolation algorithm and sufficiently many particles per cell. Crucially,  
32 however, we also show that for the chosen algorithms the number of particles per cell needs  
33 to grow with the mesh resolution in order to retain the optimal convergence order for higher  
34 order elements, leading to a method in which the cost of particle advection grows faster than  
35 the cost of the mesh-based computations if higher accuracy is required.  
36  
37

38  
39 We then extend these considerations to the time-dependent case by developing a new  
40 benchmark, and using it to evaluate the coupled finite element/PIC scheme. All of our re-  
41 sults are implemented in the open-source geodynamic modeling code ASPECT [Kronbichler  
42 et al.(2012), Heister et al.(2017)]. It is our intention that these results will act as reference  
43 results for future code comparison studies of time-independent or time-dependent PIC advec-  
44 tion algorithms, and will allow researchers to design PIC methods that use a combination of  
45 techniques to ensure optimal accuracy of the numerical method as a whole.  
46  
47  
48  
49  
50  
51  
52  
53  
54  
55  
56  
57  
58  
59  
60

This paper continues as follows: In Section 2, we present the continuous model we wish to solve. Section 3 then describes in detail how we compute numerical approximations to the solution of the model, and we end the section with a theoretical analysis of error contributions and the convergence orders one can predict using this analysis. Section 4 then uses stationary benchmarks to confirm that the theoretical analysis indeed correctly describes what one sees in practical computations. Section 5 extends these results to time-dependent problems: we first present a new, *time-dependent* benchmark (the derivation of which may be found in Appendix A) with an analytical solution. This benchmark then allows us to evaluate the error and convergence rates for time-dependent computations of incompressible Stokes flow coupled to a PIC advection method. We conclude in Section 6.

## 2 GOVERNING EQUATIONS

Geologic deformation over long time scales is commonly modeled by the incompressible Stokes equations for a slow-moving fluid, using a spatially and temporally variable viscosity that depends nonlinearly on both the strain rate and pressure of the fluid, as well as temperature, chemical composition, and possibly other factors. The driving force for the flow is provided by a buoyancy term that results from the spatial variability of the density, again due to temperature, pressure, and chemical composition differences.

The incompressible Stokes equations that describe this type of flow are given by a force balance and a mass continuity equation:

$$-\nabla \cdot (2\eta \varepsilon(\mathbf{u})) + \nabla p = \rho \mathbf{g}, \quad (1)$$

$$\nabla \cdot \mathbf{u} = 0, \quad (2)$$

where  $\mathbf{u}$  is the velocity,  $p$  the pressure,  $\rho$  the density,  $\eta$  the viscosity, and  $\mathbf{g}$  the gravity. Furthermore,  $\varepsilon(\mathbf{u}) = \frac{1}{2}(\nabla \mathbf{u} + \nabla \mathbf{u}^T)$  is the symmetric gradient of the velocity and denotes the strain rate within the fluid.

In more realistic applications, the mass continuity equation (2) has to be replaced by an equation that allows for compressible effects. However, as this is tangential to the purpose of the current paper, we will simply assume that the fluid is incompressible. In either case, the equations above are augmented by appropriate boundary conditions.

A complete description of mantle convection would couple the equations above to a set of advection-diffusion equations for the temperature and chemical compositions, as well as possibly other relevant quantities such as grain size distributions, frozen stress tensors, etc., all of which are transported along with the velocity  $\mathbf{u}$  (see [Schubert et al.(2001)]). If we

6 *R. Gassmöller, H. Lokavarapu, W. Bangerth, E. G. Puckett*

denote (the components of) these fields by  $\phi_c = \phi_c(\mathbf{x}, t)$ ,  $c = 1, \dots, C$ , then each such  $\phi_c$  typically satisfies an advection-diffusion equation of the form

$$\frac{D\phi_c}{Dt} - \nabla \cdot (\kappa_c \nabla \phi_c) = \frac{\partial \phi_c}{\partial t} + \mathbf{u} \cdot \nabla \phi_c - \nabla \cdot (\kappa_c \nabla \phi_c) = H_c, \quad (3)$$

augmented by appropriate initial conditions  $\phi_c(\mathbf{x}, 0) = \phi_{c,0}(\mathbf{x})$  and, if necessary, boundary conditions.  $H_c$  is a source term that in general depends both on the flow variables as well as some or all of the other  $\phi_{c'}$ . For example, if  $\phi_c$  denotes the temperature, then the source term might include contributions due to friction heating and adiabatic compression, while if  $\phi_c$  represents a particular material type's volume fraction, it might increase its value at the cost of that of other materials.

The importance of these additional fields lies in the fact that in realistic descriptions of convection in the Earth, the viscosity  $\eta$  and density  $\rho$  in the Stokes equations above not only depend on strain rate  $\varepsilon(\mathbf{u})$  and pressure  $p$ , but also on these additional variables  $\phi_c$ . Consequently, the resulting set of equations is coupled, nonlinear, and time dependent. An accurate solution of the complete model therefore requires an accurate way of advecting along these additional quantities.

In typical applications the equation is dominated by the advection term  $\mathbf{u} \cdot \nabla \phi_c$ , and the contributions by the diffusion term  $-\nabla \cdot (\kappa_c \nabla \phi_c)$  are rather small (if  $\phi_c$  denotes the temperature) or are completely negligible (for example if  $\phi_c$  denotes a chemical composition). In this paper, we are concerned with solving these equations for quantities for which the diffusion term can be neglected; in this case, the equation above simplifies to

$$\frac{D\phi_c}{Dt} = \frac{\partial \phi_c}{\partial t} + \mathbf{u} \cdot \nabla \phi_c = H_c. \quad (4)$$

Consequently, this paper is devoted to solving the coupled set of Stokes and advection equations, (1)–(2) and (4), accurately. In particular, we will consider approximating the solution of (4) using particle methods and how these methods affect the accuracy of solving (1)–(2) using field-based finite element methods when the two approaches are coupled.

In the following sections, we will not make use of the fact that we may, in fact, have more than one additional property. As a consequence, we will drop the index  $c$  on the quantities  $\phi_c$ . However, everything we will say below remains true for cases with multiple such properties.

### 3 NUMERICAL METHODOLOGY

Equations (1)–(2) and (4) can be solved by direct discretization via finite element, finite volume, or finite difference methods, or a variety of other methods (see, for example [Donea & Huerta(2003), Deubelbeiss & Kaus(2008), Gerya(2009), Ismail-Zadeh & Tackley(2010)]).

However, discretizing advection problems such as (4) without introducing oscillations or excessive diffusion is not trivial. As discussed above, many mantle convection codes have instead used particle schemes to advect along properties of rocks. In these schemes, a number of particles  $k = 1 \dots N$  are characterized by their location  $\mathbf{x}_k(t)$  and associated properties  $\phi_k(t)$ . Their location and value then evolves according to the ordinary differential equation

$$\frac{d}{dt}\mathbf{x}_k(t) = \mathbf{u}(\mathbf{x}_k(t), t), \quad \mathbf{x}_k(0) = \mathbf{x}_{k,0}, \quad (5)$$

$$\frac{d}{dt}\phi_k(t) = H, \quad \phi_k(0) = \phi_{k,0}, \quad (6)$$

where  $H$  is a function of both particle-based quantities  $[\mathbf{x}_k(t), \phi_k(t)]$ , field-based quantities  $[\mathbf{u}(\mathbf{x}_k(t), t), \varepsilon(\mathbf{u}(\mathbf{x}_k(t), t)), p(\mathbf{x}_k(t), t)]$ , and possibly other variables such as the time  $t$ . Conversely, coefficients in the Stokes system (1)–(2) such as the viscosity  $\eta$  and density  $\rho$  at arbitrary points  $\mathbf{x}$  (e.g., at quadrature points) may depend not only on field quantities such as velocity and pressure at  $\mathbf{x}$ , but also on the quantities  $\phi_k$  of particles located “close” to  $\mathbf{x}$ .

While conceptually simple to implement, this approach requires (i) transferring data from field-based quantities to particle locations when evaluating the right hand sides of (5) and (6) at  $\mathbf{x}_k$ , (ii) integrating particle locations and properties in time according to (5) and (6), and finally (iii) transferring data back from particle locations to quadrature points when evaluating coefficients of (1)–(2) at arbitrary locations  $\mathbf{x}$  during assembly of matrices and right hand sides for the Stokes equation.

All of these three steps introduce errors into the solution process: In the first step, the exact solution  $\mathbf{u}(t)$  is not available, and one has to use numerical approximations  $\mathbf{u}_h(t^n)$  that were found by approximating the solution of the Stokes equations at discrete times  $t^n$ . This error therefore depends on the accuracy of the spatial discretization used for the computed velocity field, and of the time-stepping scheme. In the second step, the numerical integration of (5) yields a trajectory  $\mathbf{x}_h(t)$  that is different from  $\mathbf{x}(t)$  even if the velocity were known exactly, depending on the accuracy of the ODE solver scheme; likewise, we obtain an approximation  $\phi_{h,k}(t)$  different from the exact solution  $\phi_k(t)$  of (6). Finally, no particle will typically be located on a quadrature point  $\mathbf{x}$  at time  $t$ , and the required property  $\phi(\mathbf{x}, t)$  will need to be interpolated in one of many possible, approximate ways from the properties  $\phi_k(t)$  of nearby particles.



8 *R. Gassmüller, H. Lokavarapu, W. Bangerth, E. G. Puckett*

We will assess these errors quantitatively in Section 4 and Section 5 in a number of benchmarks, for different Stokes discretizations, different initial particle locations, ODE solvers, and particle interpolation methods, all of which we will describe in remainder of this section.

### 3.1 Discretization of the Stokes system

The advection of particles can only be as accurate as the underlying velocity field that is used to advect them. In this work, the velocity is obtained by using finite elements to discretize and solve the Stokes equations. Specifically, we will employ the common  $Q_k \times Q_{k-1}$  “Taylor-Hood” element [Taylor & Hood(1973)] in which the velocity and pressure are discretized by continuous finite elements of degrees  $k$  and  $k - 1$  on quadrilaterals or hexahedra, respectively. For comparison to the existing results of [Thielmann et al.(2014)], we will also use  $Q_k \times P_{-(k-1)}$  elements in which the pressure is discretized using discontinuous polynomials of (total) degree  $k - 1$ . Based on finite-element theory we expect both the  $Q_k \times Q_{k-1}$  and the  $Q_k \times P_{-(k-1)}$  elements to show optimal convergence order [Bercovier & Pironneau(1979)]; i.e., to show a decay of the velocity and pressure errors, when measured in the  $L_2$  norm, as  $h^{k+1}$  and  $h^k$ , respectively, where  $h$  is the element size of the mesh. We show in Section 4 and 5 that this is indeed the case for our implementation and model setups. In all of our experiments we assume that the Stokes equation is solved either with a direct solver, or with a sufficiently tight tolerance on an iterative solver, so that the only remaining error stems from the spatial discretization of the flow field intrinsic to the used finite-element.

### 3.2 Generation of particles

In time dependent problems, particles are transported along with the flow; after some time, they will no longer be at specific locations. Therefore, algorithms that reconstruct coefficients from particles’ properties need to be general and deal with both arbitrary particle numbers and locations on each cell. However, the test cases we will consider in Section 4, will only solve a single time step without advecting particles. Thus, the particles are located where they were created, and we need to make sure not to rely on a specific particle distribution that controls our results.

We will consider two strategies for choosing the initial particle locations  $\mathbf{x}_k(0) = \mathbf{x}_{k,0}$ :

(i) Create a number of particles  $N_K$  on a regular grid of points within the cell  $\hat{K}$  in the reference domain, from where they are mapped to the corresponding points on each cell  $K$  of the triangulation.

(ii) Create a number of particles  $N_K$  within each cell  $K$ , with locations drawn from a uniform probability distribution on  $K$ ; here,  $N_K$  is equal to the fraction of the volume occupied by cell  $K$  relative to the volume of the global domain  $\Omega$ , times the global number of particles  $N$ .

The practical implementation of both algorithms in arbitrary geometries is described in [Gassmüller et al.(2018)]. Note, that approach (i) will lead to a constant particle count per cell, while approach (ii) will lead to a roughly constant particle density per area.

Choosing between the two strategies allows us to determine the influence of different particle distributions on the accuracy of the solution. As we will see, for our benchmarks models with uniform mesh resolution these differences are in fact pretty small, although they would become important for adaptive meshes, and after a finite amount of shear. Furthermore, for the time-dependent benchmark cases in Section 5, initial particle locations are less critical as particles are moving from their starting positions; for easier reproducibility, we therefore always generate particles at regular grid locations (approach (i)) in the time dependent cases.

### 3.3 Advection of particles

As described above, the advection of particles involves solving (5) for their position, which we do using a Runge-Kutta method of second (RK2) or fourth order (RK4). As expected and as shown for our implementation before (see supporting information of [Gassmüller et al.(2018)]) the error of particle positions for a given static flow field reduces as  $\Delta t^2$  and  $\Delta t^4$  for RK2 and RK4 respectively. However, because we will use a second order accurate BDF2 time-stepping scheme for our Stokes solution, any particle advection method is limited for a time-varying velocity field to be second order accurate in time. Since the exact solution of the benchmark in Section 5 is time-independent, this will not be a limiting factor for our experiments. Nevertheless, this limitation has to be considered for realistic applications. We also note that our discrete velocity solutions are only divergence-free in an integral sense, and evaluating the velocity at the particle locations introduces a spurious velocity divergence that can lead to the clustering of particles in certain flow patterns. This phenomenon can be improved using velocity corrections known as conservative velocity interpolation [Meyer & Jenny(2004), Wang et al.(2015), Pusok et al.(2017)]. However, even perfectly known and divergence free velocities can form shear patterns that lead to particle clustering; this can be addressed with appropriate particle weighting, splitting, and merging schemes [Samuel(2018)]. We did not employ such methods in our benchmarks, as we limited our benchmarks to moderate strain, and we were mostly concerned with the optimal convergence rate possible with the unmodified advection

1  
2  
3  
4  
5  
6  
7  
8  
9  
10  
11  
12  
13  
14  
15  
16  
17  
18  
19  
20  
21  
22  
23  
24  
25  
26  
27  
28  
29  
30  
31  
32  
33  
34  
35  
36  
37  
38  
39  
40  
41  
42  
43  
44  
45  
46  
47  
48  
49  
50  
51  
52  
53  
54  
55  
56  
57  
58  
59  
60

10 *R. Gassmöller, H. Lokavarapu, W. Bangerth, E. G. Puckett*

schemes. Nevertheless, it would be an interesting future study to quantify the influence of such velocity modifications on the accuracy of the particle advection, while ensuring that they do not affect the convergence rate.

### 3.4 Interpolation of particle data

Since particles carry material properties  $\phi_k$  that enter the assembly of the linear systems used to solve for the field-based quantities, we need to define how these material properties can be evaluated at quadrature points  $\mathbf{x}$  that do not, in general, coincide with the location of any of the particles. This operation is often called “interpolation” from particle locations to the mesh, though a better term may in fact be “projection”; we will use the terms interchangeably. In particular, let  $K$  be a cell,  $I_K \subseteq [1, N]$  be the set of those particle indices (among the overall  $N$  particles) that are located on  $K$ , and  $N_K = |I_K|$  be their number. Then we consider the following two strategies to evaluate property  $\phi$  at an arbitrary location  $\mathbf{x}$  based on the information  $\{\phi_k\}_{k \in I_K}$  that is available on  $K$  alone:

(i) Piecewise constant averages: To obtain  $\phi(\mathbf{x})$  on cell  $K$ , we average the material properties among all particles located on  $K$ :

$$\phi|_K = \frac{1}{N_K} \sum_{k \in I_K} \phi_k. \quad (7)$$

The value  $\phi(\mathbf{x})$  is then computed by finding the cell  $K$  within which  $\mathbf{x}$  is located, and taking the local average on  $K$ . In theory one could use different averaging schemes than arithmetic averaging, for example harmonic or geometric averaging. However, since it was shown before that these schemes converge with the same order (though varying absolute accuracy) to the correct solution [Thielmann et al.(2014)] (see also the related discussion in [Heister et al.(2017)]), here we limit ourselves to arithmetic averaging.

(ii) Least squares (bi-/tri-)linear interpolation: In this algorithm, we seek a function  $\phi$  that is (bi-/tri-)linear on each cell  $K$ . We will allow it to be discontinuous between cells, and in that case it can be computed locally on each cell independently. Specifically, we seek  $\phi|_K$  so that it minimizes the squared error,

$$\epsilon^2 = \sum_{k \in I_K} [\phi|_K(\mathbf{x}_k) - \phi_k]^2, \quad (8)$$

where  $\mathbf{x}_k$  is the location of particle  $k$  with associated property  $\phi_k$ .

The minimizer  $\phi|_K$  is found by solving a  $4 \times 4$  matrix in 2 dimensions, or an  $8 \times 8$  matrix in three dimensions, for the coefficients of the (bi-/tri-)linear least-squares approximation. To obtain material property values at an arbitrary  $\mathbf{x}$  in  $K$  then only requires evaluating

$\phi|_K(\mathbf{x})$ , i.e., evaluating the (bi-/tri-)linear shape functions of the approximand times their corresponding coefficient values. As observed before [Thielmann et al.(2014)] this algorithm generates over-/undershooting close to strong property gradients, which need to be handled in some form, for example by a strict limiter for the interpolated property. However, all of the benchmark results we show below are either sufficiently smooth or have property gradients aligned with the mesh, therefore we did not need to apply the limiter here. Note that in contrast to [Thielmann et al.(2014)] we include the mixed polynomial terms  $xy$  (and, in three space dimensions,  $xz$ ,  $yz$ ,  $xyz$ ) in the interpolation function to stay consistent with the polynomial space of our pressure element. This modification potentially explains why our method performs better for lower number of particles per cell, as discussed in Section 4.1.

### 3.5 An error analysis

In this section, let us provide some theoretical considerations for how the particle-based scheme outlined above might affect the overall error in the finite element solution of the Stokes problem. Our goal here is to derive error convergence orders for the  $L_2$  norm errors in velocity and pressure, i.e., for

$$\|\mathbf{u} - \mathbf{u}_h\|_{L_2} = \left( \int |\mathbf{u}(\mathbf{x}, t) - \mathbf{u}_h(\mathbf{x}, t)|^2 dx \right)^{1/2}, \quad (9)$$

$$\|p - p_h\|_{L_2} = \left( \int |p(\mathbf{x}, t) - p_h(\mathbf{x}, t)|^2 dx \right)^{1/2}. \quad (10)$$

We will test the statements we will derive in computational experiments in the sections to follow.

Before stating concrete error inequalities, let us present the conceptual framework in which these are presented. In particular, in Section 4 we will consider the numerical approximation of the solution of a stationary Stokes problem (1)–(2) using the finite element method in which we do not know the exact density  $\rho$  and viscosity  $\eta$ , but only have this information available at the locations of particles. (In Section 5, where we consider time dependent benchmarks, we will in fact only know the exact density and viscosity at points  $\mathbf{x}_k$  whose coordinates are only approximately known; we ignore this for the moment.) This can be stated as follows: In the numerical problem that we will solve using the finite element method, we will use a density  $\rho_h = I_h R_h \rho$  and viscosity  $\eta_h = I_h R_h \eta$ , where the operator  $R_h f$  restricts the values of a function  $f$  to the locations of particles, and the operator  $I_h$  interpolates the values of a function defined only at particle locations to the entire domain so that it can be evaluated at arbitrary quadrature points for use in the finite element method;  $I_h$  can be one of the two

12 *R. Gassmöller, H. Lokavarapu, W. Bangerth, E. G. Puckett*

options discussed in the previous subsection. The question is how the replacement of  $\rho, \eta$  by  $\rho_h, \eta_h$  affects the accuracy with which we can compute numerical approximations  $\mathbf{u}_h, p_h$  via the finite element method.

Let us then concisely define what problem we solve. In particular, let  $\mathcal{L}_\eta$  be the solution operator of the Stokes equations (1)–(2), i.e., for a given right hand side  $\rho\mathbf{g}$  and viscosity  $\eta$ , we have that  $\{\mathbf{u}, p\} = \mathcal{L}_\eta(\rho\mathbf{g})$  solves the Stokes equations. Furthermore, let  $\mathcal{L}_\eta^h$  be the *discrete* solution operator, i.e.,  $\{\mathbf{u}_h, p_h\} = \mathcal{L}_\eta^h(\rho\mathbf{g})$  is the finite element solution of these equations. The question we want to answer is how the exact solution  $\mathcal{L}_\eta(\rho\mathbf{g})$  relates to the finite element approximation  $\mathcal{L}_{\eta_h}^h(\rho_h\mathbf{g})$  in which we have replaced density and viscosity as discussed above. Specifically, we will measure this error in the “energy norm”:

$$\|\mathcal{L}_\eta(\rho\mathbf{g}) - \mathcal{L}_{\eta_h}^h(\rho_h\mathbf{g})\|^2 = \eta_0 \|\nabla(\mathbf{u} - \mathbf{u}_h)\|_{L_2}^2 + \|p - p_h\|_{L_2}^2, \quad (11)$$

where  $\eta_0$  is a suitably chosen reference viscosity that ensures that the two terms are appropriately balanced and have matching physical units. We will later relate this norm to the  $L_2$  norms of both the velocity and pressure errors (instead of the  $H^1$  seminorm of the velocity and the  $L_2$  norm of the pressure).

To answer the question about the size of the error, let us first consider the following auxiliary problem: It is well known that replacing a sufficiently smooth function  $\rho$  or  $\eta$  by a suitable (i) piecewise constant or (ii) piecewise (bi-/tri-)linear approximation on a mesh of maximal mesh size  $h$  incurs an error proportional to  $h$  and  $h^2$ , respectively, when measuring the error in the  $L_2$  norm. In other words, if we denote these approximants by  $P_h\rho$  and  $P_h\eta$ , then

$$\begin{aligned} \|\rho - P_h\rho\|_{L_2} &= \mathcal{O}(h^r), \\ \|\eta - P_h\eta\|_{L_2} &= \mathcal{O}(h^r), \end{aligned} \quad (12)$$

where  $r = 1$  for approximation option (i) and  $r = 2$  for option (ii) of the previous subsection. Concisely, we define  $P_h$  locally on each cell  $K$  as follows, when applied to an arbitrary function  $f$ :

$$\begin{aligned} \text{option (i): } P_h f|_K &= \frac{1}{|K|} \int_K f \\ \text{option (ii): } P_h f|_K &= \arg \min_{\varphi_h \in Q_1(K)} \frac{1}{2} \|f - \varphi_h\|_{L_2(K)}^2 \end{aligned} \quad (13)$$

Note that  $P_h$  is equal to  $I_h R_h$  if one were to consider infinitely many particles equally distributed on each cell  $K$  because then the points-based least-squares approximations (7) and (8) agree with the integral-based least-squares approximations in (13). Below, we will also

need estimates such as (12) in other norms, and consequently state the following results:

$$\begin{aligned}\|f - P_h f\|_{H^1} &= \mathcal{O}(h^{r-1}), \\ \|f - P_h f\|_{H^{-1}} &= \mathcal{O}(h^{r+1}),\end{aligned}\tag{14}$$

where the first denotes the error in the gradient of  $f$ .

Using this argument, we can now decompose the overall error into four components. Namely, we will write the error as follows:

$$(\eta_0 \|\nabla(\mathbf{u} - \mathbf{u}_h)\|_{L_2}^2 + \|p - p_h\|_{L_2}^2)^{1/2}\tag{15}$$

$$= \|\mathcal{L}_\eta(\rho \mathbf{g}) - \mathcal{L}_{\eta_h}^h(\rho_h \mathbf{g})\|\tag{16}$$

$$\leq \underbrace{\|\mathcal{L}_\eta(\rho \mathbf{g}) - \mathcal{L}_\eta(P_h \rho \mathbf{g})\|}_{(1)}\tag{17}$$

$$+ \underbrace{\|\mathcal{L}_\eta(P_h \rho \mathbf{g}) - \mathcal{L}_{P_h \eta}(P_h \rho \mathbf{g})\|}_{(2)}\tag{18}$$

$$+ \underbrace{\|\mathcal{L}_{P_h \eta}(P_h \rho \mathbf{g}) - \mathcal{L}_{\eta_h}(\rho_h \mathbf{g})\|}_{(3)}\tag{19}$$

$$+ \underbrace{\|\mathcal{L}_{\eta_h}(\rho_h \mathbf{g}) - \mathcal{L}_{\eta_h}^h(\rho_h \mathbf{g})\|}_{(4)}.\tag{20}$$

Here, the four norm terms on the right correspond, respectively, to (1) the error introduced by replacing  $\rho$  by the projection  $P_h \rho$  when solving the continuous Stokes equations, (2) the error introduced by replacing  $\eta$  by the projection  $P_h \eta$  when solving the continuous Stokes equations, (3) the error introduced by further substituting  $P_h \rho, P_h \eta$  by  $\rho_h = I_h R_h \rho, \eta_h = I_h R_h \eta$  when solving the continuous Stokes equations, and (4) the error introduced by the finite element solution instead of the exact solution of two problems with the same coefficients. Let us determine the size of these terms individually, in increasing order of difficulty.

For the discretization error, (4), it is well known that when using either  $Q_k \times Q_{k-1}$  or  $Q_k \times P_{-(k-1)}$  finite elements, we have

$$\|\mathcal{L}_{\eta_h}(\rho_h \mathbf{g}) - \mathcal{L}_{\eta_h}^h(\rho_h \mathbf{g})\| = \mathcal{O}(h^k),\tag{21}$$

where  $h$  is the diameter of the largest cell of the mesh. It is worth mentioning that this statement is only correct if the solution is sufficiently smooth (for example,  $\mathbf{u} \in H^{k+1}$  and  $p \in H^k$ ).

The replacement error for the density (1) is also easy. To this end, one needs to know that

1  
2  
3  
4  
5  
6  
7  
8  
9  
10  
11  
12  
13  
14  
15  
16  
17  
18  
19  
20  
21  
22  
23  
24  
25  
26  
27  
28  
29  
30  
31  
32  
33  
34  
35  
36  
37  
38  
39  
40  
41  
42  
43  
44  
45  
46  
47  
48  
49  
50  
51  
52  
53  
54  
55  
56  
57  
58  
59  
60

14 *R. Gassmöller, H. Lokavarapu, W. Bangerth, E. G. Puckett*

the Stokes operator is linear and stable in the  $H^{-1}$  norm, i.e., that

$$\|\mathcal{L}_\eta f_1 - \mathcal{L}_\eta f_2\| = \|\mathcal{L}_\eta(f_1 - f_2)\| \leq C \|f_1 - f_2\|_{H^{-1}}. \quad (22)$$

with some constant  $C < \infty$ . Since  $f_1 = \rho$  and  $f_2 = P_h \rho$ , we can use (14) to obtain that the first error term satisfies

$$\|\mathcal{L}_\eta(\rho \mathbf{g}) - \mathcal{L}_\eta(P_h \rho \mathbf{g})\| = \mathcal{O}(h^{r+1}). \quad (23)$$

The replacement error for the viscosity, (2), is more difficult to analyze. However, it is reasonable to assume that the solutions of two Stokes equations with viscosities  $\eta_1, \eta_2$  differ by an amount proportional to  $\|\eta_1 - \eta_2\|_{L_2}$ . This would here suggest, invoking (12), that

$$\|\mathcal{L}_{P_h \eta}(P_h \rho \mathbf{g}) - \mathcal{L}_\eta(P_h \rho \mathbf{g})\| \leq D \|\eta - P_h \eta\|_{L_2} = \mathcal{O}(h^r), \quad (24)$$

again with some constant  $D$ . We have no proof of this statement, though it seems reasonable using standard arguments in the analysis of elliptic PDEs (see, for example, [Gilbarg & Trudinger(1983)]). The use of the  $L_2$  norm – or maybe the  $L_\infty$  norm, for which one obtains the same estimate – seems natural when analyzing PDE solutions this way. One might be tempted to ask whether one could replace  $\|\eta - P_h \eta\|_{L_2}$  by  $\|\eta - P_h \eta\|_{H^{-1}}$  and thereby gain an order of convergence. But it will turn out, based on our numerical examples, that the estimate is indeed correct as stated regarding the order of convergence.

This leaves the error (3) due to replacing the projections  $P_h \rho, P_h \eta$  by the interpolants  $\rho_h = I_h R_h \rho, \eta_h = I_h R_h \eta$ . Similar arguments as for the errors (1) and (2) yield that

$$\begin{aligned} \|\mathcal{L}_{P_h \eta}(P_h \rho \mathbf{g}) - \mathcal{L}_{\eta_h}(\rho_h \mathbf{g})\| \\ \leq C \|P_h \rho - I_h R_h \rho\|_{H^{-1}} + D \|P_h \eta - I_h R_h \eta\|_{L_2}. \end{aligned} \quad (25)$$

The exact size of these terms depends on how many particle locations we have on each cell, as well as how they are located. All we know is that if we increase the number of points, and if these points are uniformly distributed, then  $I_h R_h \rightarrow P_h$  and consequently the entire error term goes to zero. For finite numbers of particles per cell (*PPC*), we will simply denote the right hand side as  $E(h, PPC)$  with the expectation that asymptotically  $E(h, PPC) \rightarrow 0$  as  $PPC \rightarrow \infty$  or  $h \rightarrow 0$ .

Taking all of this together then yields that we should expect the following error behavior in the energy norm of the Stokes problem:

$$\begin{aligned} (\eta_0 \|\nabla(\mathbf{u} - \mathbf{u}_h)\|_{L_2}^2 + \|p - p_h\|_{L_2}^2)^{1/2} \\ = \mathcal{O}(h^{r+1}) + \mathcal{O}(h^r) + \mathcal{O}(E(h, PPC)) + \mathcal{O}(h^k). \end{aligned} \quad (26)$$

This immediately yields the desired behavior of the pressure error in the  $L_2$  norm:

$$\|p - p_h\|_{L_2} = \mathcal{O}(h^{r+1}) + \mathcal{O}(h^r) + \mathcal{O}(E(h, PPC)) + \mathcal{O}(h^k). \quad (27)$$

The velocity error in the  $L_2$  norm requires marginally more work. Using the standard Nitsche trick [Brenner & Scott(2007)] to obtain the  $L_2$  error from the  $H^1$  error provides us with an extra power of  $h$  and then yields

$$\|\mathbf{u} - \mathbf{u}_h\|_{L_2} = \mathcal{O}(h^{r+2}) + \mathcal{O}(h^{r+1}) + \mathcal{O}(h E(h, PPC)) + \mathcal{O}(h^{k+1}). \quad (28)$$

The next section of this paper is in essence an exploration of these last two relationships using concrete testcases.

#### 4 INSTANTANEOUS BENCHMARKS

The first set of benchmarks we will consider only solves a single time step; thus, the positions of particles are known *exactly*. The benchmarks are therefore intended to test the influence of initial particle distributions, Stokes discretizations, and the transfer of information from particles to field-based quantities.

Specifically, we will consider the SolKz and SolCx benchmarks [Revenaugh & Parsons(1987), Zhong(1996)] that have previously been used to test the accuracy of Stokes solvers in the presence of a spatially variable viscosity [Duretz et al.(2011), Kronbichler et al.(2012)]. For both benchmarks, an exact solution for the velocity and pressure fields is available. We can then compare the convergence order we obtain if (i) we use the exact density and viscosity when assembling the finite element linear system for the Stokes system, or (ii) we use viscosity and density values that are interpolated from a set of nearby particles that have each been initialized using the exact values at their respective location. In the first of these cases, only contribution (4) of the errors considered in Section 3.5 is present, whereas in the second case, all four contributions matter.

As we will show, and as anticipated in Section 3.5, the way we interpolate from nearby particles to quadrature points greatly matters in retaining (or not retaining) the convergence order of the finite element scheme. To assess this quantitatively, we will evaluate the difference between the known, exact solution and the computed, approximate solution in the  $L_2$  norm as defined in Section 3.5, considering both the velocity and pressure. The involved integrals are approximated through quadrature using a Gauss formula with two more quadrature points in



1  
2  
3  
4 16 *R. Gassmöller, H. Lokavarapu, W. Bangerth, E. G. Puckett*

5 each coordinate direction than the polynomial degree of the velocity element; this guarantees  
6 both an accurate evaluation of the integral and avoids inadvertent super-convergence effects.  
7

8 We will defer to the next section a discussion of time dependent cases where we also have  
9 to deal with the additional error introduced by inexact advection of particle locations.  
10  
11

#### 12 13 4.1 SolKz

14  
15 The SolKz benchmark [Duretz et al.(2011)] uses a smoothly varying viscosity on a 2D square  
16 domain with height and width of one. It uses tangential boundary conditions, a vertical gravity  
17 of 1, and chooses the density field in such a way that one can construct an exact solution for  
18 the Stokes equation with the given viscosity.  
19  
20

21 Specifically, the viscosity varies with depth  $y$  as

$$22 \quad \eta(x, y) = e^{2By}, \quad (29)$$

23  
24 where  $B$  is chosen such that the viscosity ratio between top and bottom is  $10^6$ . The density  
25 is given by  
26  
27

$$28 \quad \rho(x, y) = -\sin(2y) \cos(3\pi x). \quad (30)$$

29  
30 We begin by investigating the influence of the initial particle locations on the convergence  
31 rate of the velocity and pressure solution for either of the two interpolation methods discussed  
32 before. We show these results in Table 1 for different mesh resolutions. The methods converge  
33 with different rates, and indeed at the rates predicted by (27) and (28). The initial particle  
34 locations do not influence the convergence rate significantly, though the absolute errors are  
35 somewhat larger for random particle locations, likely because some cells receive unfavorable  
36 particle locations (e.g., a high particle density in only a small volume of the cell). We also  
37 observe that for smaller numbers of particles per cell than the one shown here, the difference  
38 between the results obtained using regular and random particle locations is larger. This is  
39 intuitive, as for an infinite number of particles the two methods should generate similar particle  
40 locations, namely particles in every possible location, while for few particles all of them could  
41 be randomly generated in a very small part of the cell, leaving a large region unsampled.  
42 Having established that the choice of initial particle locations does not influence the achieved  
43 convergence rate, we will conduct all other experiments with a regular particle distribution,  
44 as this delivers more reproducible model results.  
45  
46  
47  
48  
49  
50  
51  
52  
53  
54  
55

56 Given that both viscosity and density in this benchmark are smooth, we expect the ve-  
57 locity and pressure fields to also be sufficiently smooth for a finite element method to obtain  
58 the optimal convergence order if the coefficients are evaluated exactly at each quadrature  
59  
60

**Table 1.** Velocity errors  $\|\mathbf{u} - \mathbf{u}_h\|_{L_2}$  and pressure errors  $\|p - p_h\|_{L_2}$  for the SolKz benchmark using the  $Q_2 \times P_{-1}$  Stokes element ( $k = 2$ ), for arithmetic averaging ( $r = 1$ ) and bilinear least squares ( $r = 2$ ) interpolation methods, and for regular and random particle distributions as discussed in Section 3.2.  $PPC$  (particles per cell),  $k$ , and  $r$  are as defined in Section 3.5.

Arithmetic average ( $r = 1$ )					
$h$	$PPC$	regular		random	
		$\ \mathbf{u} - \mathbf{u}_h\ _{L_2}$	rate	$\ \mathbf{u} - \mathbf{u}_h\ _{L_2}$	rate
$\frac{1}{8}$	100	$7.05 \cdot 10^{-6}$	-	$7.08 \cdot 10^{-6}$	-
$\frac{1}{16}$	100	$1.86 \cdot 10^{-6}$	1.92	$1.95 \cdot 10^{-6}$	1.86
$\frac{1}{32}$	100	$4.81 \cdot 10^{-7}$	1.95	$4.87 \cdot 10^{-7}$	2.00
$\frac{1}{64}$	100	$1.22 \cdot 10^{-7}$	1.98	$1.29 \cdot 10^{-7}$	1.92
$\frac{1}{128}$	100	$3.05 \cdot 10^{-8}$	2.00	$2.93 \cdot 10^{-8}$	2.13
$\frac{1}{256}$	100	$7.63 \cdot 10^{-9}$	2.00	$7.91 \cdot 10^{-9}$	1.89
		$\ p - p_h\ _{L_2}$		$\ p - p_h\ _{L_2}$	
$\frac{1}{8}$	100	$1.91 \cdot 10^{-2}$	-	$1.92 \cdot 10^{-2}$	-
$\frac{1}{16}$	100	$1.24 \cdot 10^{-2}$	0.62	$1.24 \cdot 10^{-2}$	0.63
$\frac{1}{32}$	100	$6.57 \cdot 10^{-3}$	0.92	$6.60 \cdot 10^{-3}$	0.91
$\frac{1}{64}$	100	$3.33 \cdot 10^{-3}$	0.98	$3.35 \cdot 10^{-3}$	0.98
$\frac{1}{128}$	100	$1.67 \cdot 10^{-3}$	1.00	$1.68 \cdot 10^{-3}$	1.00
$\frac{1}{256}$	100	$8.37 \cdot 10^{-4}$	1.00	$8.40 \cdot 10^{-4}$	1.00
Bilinear least squares ( $r = 2$ )					
$h$	$PPC$	regular		random	
		$\ \mathbf{u} - \mathbf{u}_h\ _{L_2}$	rate	$\ \mathbf{u} - \mathbf{u}_h\ _{L_2}$	rate
$\frac{1}{8}$	100	$1.72 \cdot 10^{-6}$	-	$1.68 \cdot 10^{-6}$	-
$\frac{1}{16}$	100	$2.46 \cdot 10^{-7}$	2.81	$2.49 \cdot 10^{-7}$	2.75
$\frac{1}{32}$	100	$3.50 \cdot 10^{-8}$	2.81	$3.52 \cdot 10^{-8}$	2.82
$\frac{1}{64}$	100	$4.56 \cdot 10^{-9}$	2.94	$4.71 \cdot 10^{-9}$	2.90
$\frac{1}{128}$	100	$5.95 \cdot 10^{-10}$	2.94	$6.55 \cdot 10^{-10}$	2.85
$\frac{1}{256}$	100	$8.41 \cdot 10^{-11}$	2.82	$1.05 \cdot 10^{-10}$	2.64
		$\ p - p_h\ _{L_2}$		$\ p - p_h\ _{L_2}$	
$\frac{1}{8}$	100	$4.53 \cdot 10^{-3}$	-	$4.72 \cdot 10^{-3}$	-
$\frac{1}{16}$	100	$1.30 \cdot 10^{-3}$	1.80	$1.33 \cdot 10^{-3}$	1.83
$\frac{1}{32}$	100	$3.42 \cdot 10^{-4}$	1.93	$3.49 \cdot 10^{-4}$	1.93
$\frac{1}{64}$	100	$8.67 \cdot 10^{-5}$	1.98	$8.84 \cdot 10^{-5}$	1.98
$\frac{1}{128}$	100	$2.17 \cdot 10^{-5}$	2.00	$2.22 \cdot 10^{-5}$	1.99
$\frac{1}{256}$	100	$5.43 \cdot 10^{-6}$	2.00	$5.54 \cdot 10^{-6}$	2.00

point during the assembly of linear systems. In accordance with earlier studies [Thielmann et al.(2014)] we will call this the “*direct method*”, and in the notation of Section 3.5 and Equation (12) it corresponds to  $r = \infty$  because the projection of the coefficients onto the function that is actually evaluated is the identity operation. The results of Section 3.5 then

18 *R. Gassmöller, H. Lokavarapu, W. Bangerth, E. G. Puckett*

**Table 2.** Velocity errors  $\|\mathbf{u} - \mathbf{u}_h\|_{L_2}$  and pressure errors  $\|p - p_h\|_{L_2}$  for the SolKz benchmark using the  $Q_2 \times P_{-1}$  (top rows), and  $Q_3 \times Q_2$  (bottom rows) Stokes elements. *PPC* (particles per cell),  $k$ , and  $r$  are as defined in Section 3.5.

$Q_2 \times P_{-1} (k = 2)$									
$\ \mathbf{u} - \mathbf{u}_h\ _{L_2}$	direct method ( $r = \infty$ )		arithmetic average ( $r = 1$ )			bilinear least squares ( $r = 2$ )			
	$h$	error	rate	<i>PPC</i>	error	rate	<i>PPC</i>	error	rate
$\frac{1}{8}$	$1.51 \cdot 10^{-6}$	-	4	$6.32 \cdot 10^{-6}$	-	4	$2.24 \cdot 10^{-6}$	-	
$\frac{1}{16}$	$2.50 \cdot 10^{-7}$	2.60	4	$1.61 \cdot 10^{-6}$	1.97	4	$3.61 \cdot 10^{-7}$	2.63	
$\frac{1}{32}$	$3.52 \cdot 10^{-8}$	2.80	4	$4.15 \cdot 10^{-7}$	1.96	9	$4.62 \cdot 10^{-8}$	2.97	
$\frac{1}{64}$	$4.53 \cdot 10^{-9}$	3.00	4	$1.05 \cdot 10^{-7}$	1.98	25	$5.3 \cdot 10^{-9}$	3.12	
$\frac{1}{128}$	$5.7 \cdot 10^{-10}$	3.00	4	$2.63 \cdot 10^{-8}$	2.00	49	$6.75 \cdot 10^{-10}$	2.97	
$\frac{1}{256}$	$7.23 \cdot 10^{-11}$	3.00	4	$6.58 \cdot 10^{-9}$	2.00	100	$8.41 \cdot 10^{-11}$	3.00	
$\frac{1}{512}$	$9.14 \cdot 10^{-12}$	3.00	4	$1.64 \cdot 10^{-10}$	2.00	196	$1.05 \cdot 10^{-11}$	3.00	
$\ p - p_h\ _{L_2}$									
$\frac{1}{8}$	$5.02 \cdot 10^{-3}$	-	4	$1.93 \cdot 10^{-2}$	-	4	$4.58 \cdot 10^{-3}$	-	
$\frac{1}{16}$	$1.33 \cdot 10^{-3}$	1.90	4	$1.24 \cdot 10^{-2}$	0.64	4	$1.31 \cdot 10^{-3}$	1.80	
$\frac{1}{32}$	$3.44 \cdot 10^{-4}$	2.00	4	$6.58 \cdot 10^{-3}$	0.92	9	$3.43 \cdot 10^{-4}$	1.94	
$\frac{1}{64}$	$8.68 \cdot 10^{-5}$	2.00	4	$3.33 \cdot 10^{-3}$	0.98	25	$8.67 \cdot 10^{-5}$	1.98	
$\frac{1}{128}$	$2.17 \cdot 10^{-5}$	2.00	4	$1.67 \cdot 10^{-3}$	1.00	49	$2.17 \cdot 10^{-5}$	2.00	
$\frac{1}{256}$	$5.43 \cdot 10^{-6}$	2.00	4	$8.37 \cdot 10^{-4}$	1.00	100	$5.43 \cdot 10^{-6}$	2.00	
$\frac{1}{512}$	$1.36 \cdot 10^{-6}$	2.00	4	$4.19 \cdot 10^{-4}$	1.00	196	$1.36 \cdot 10^{-6}$	2.00	
$Q_3 \times Q_2 (k = 3)$									
$\ \mathbf{u} - \mathbf{u}_h\ _{L_2}$	direct method ( $r = \infty$ )		arithmetic average ( $r = 1$ )			bilinear least squares ( $r = 2$ )			
	$h$	error	rate	<i>PPC</i>	error	rate	<i>PPC</i>	error	rate
$\frac{1}{8}$	$3.1 \cdot 10^{-7}$	-	4	$5.78 \cdot 10^{-6}$	-	9	$1.26 \cdot 10^{-6}$	-	
$\frac{1}{16}$	$2.48 \cdot 10^{-8}$	3.64	4	$1.36 \cdot 10^{-6}$	2.08	9	$1.64 \cdot 10^{-7}$	2.94	
$\frac{1}{32}$	$1.59 \cdot 10^{-9}$	3.96	4	$3.34 \cdot 10^{-7}$	2.03	16	$2.09 \cdot 10^{-8}$	2.97	
$\frac{1}{64}$	$9.9 \cdot 10^{-11}$	4.00	4	$8.27 \cdot 10^{-8}$	2.01	36	$2.27 \cdot 10^{-9}$	3.20	
$\frac{1}{128}$	$6.23 \cdot 10^{-12}$	3.99	4	$2.06 \cdot 10^{-8}$	2.01	81	$2.52 \cdot 10^{-10}$	3.17	
$\frac{1}{256}$			4	$5.13 \cdot 10^{-9}$	2.00	169	$3.01 \cdot 10^{-11}$	3.07	
$\frac{1}{512}$			4	$1.28 \cdot 10^{-9}$	2.00	361	$3.66 \cdot 10^{-12}$	3.04	
$\ p - p_h\ _{L_2}$									
$\frac{1}{8}$	$7.04 \cdot 10^{-4}$	-	4	$1.86 \cdot 10^{-2}$	-	9	$1.37 \cdot 10^{-3}$	-	
$\frac{1}{16}$	$1.15 \cdot 10^{-4}$	2.61	4	$8.27 \cdot 10^{-3}$	1.17	9	$1.18 \cdot 10^{-3}$	0.21	
$\frac{1}{32}$	$1.68 \cdot 10^{-5}$	2.78	4	$3.06 \cdot 10^{-3}$	1.43	16	$3.52 \cdot 10^{-4}$	1.74	
$\frac{1}{64}$	$2.3 \cdot 10^{-6}$	2.89	4	$1.11 \cdot 10^{-3}$	1.47	36	$9.19 \cdot 10^{-5}$	1.94	
$\frac{1}{128}$	$3.03 \cdot 10^{-7}$	2.92	4	$3.99 \cdot 10^{-4}$	1.48	81	$2.32 \cdot 10^{-5}$	1.98	
$\frac{1}{256}$	$3.89 \cdot 10^{-8}$	2.96	4	$1.43 \cdot 10^{-4}$	1.48	169	$5.83 \cdot 10^{-6}$	2.00	
$\frac{1}{512}$	$4.94 \cdot 10^{-9}$	2.98	4	$5.07 \cdot 10^{-5}$	1.49	361	$1.46 \cdot 10^{-6}$	2.00	

predict that, for both the  $Q_k \times Q_{k-1}$  and the  $Q_k \times P_{-(k-1)}$  elements, the velocity and pressure errors decay as  $h^{k+1}$  and  $h^k$ , respectively. Indeed, we show this experimentally in the leftmost columns of Table 2 for  $Q_2 \times P_{-1}$  (in the top rows), and for  $Q_3 \times Q_2$  (in the bottom rows). These results – as well as those in the remainder of the paper – omit data points where the error is less than approximately  $10^{-12}$ , since at that point round-off errors, ill-conditioning of the linear systems, and the finite tolerance of iterative solvers begin to dominate the overall error.

Next, we investigate the case where the viscosity and density are not obtained from an exactly prescribed function, but are instead interpolated from nearby particles. The corresponding convergence orders for the velocity and pressure errors are shown in the second and third set of columns in Table 2. For these results, we use between 4 and 361 particles per cell (*PPC*), distributed on a regular, equidistant grid. For models in which results depend on increasing *PPC* we always choose the smallest, most efficient number of particles that reaches the largest possible convergence rate.

The table then shows that a cellwise arithmetic average interpolation for the  $Q_2 \times P_{-1}$  element reduces the convergence of the velocity error to second order. We have verified that this remains so if the number of particles per cell were larger than the one used in the table. In other words using a cell-wise constant averaging is suboptimal by one order no matter how many *PPC* are used, and this also makes sense in view of the discussion in Section 3.5 that suggests that the best order that can be achieved is  $\min\{k + 1, r + 1\}$  for the velocity and  $\min\{k, r\}$  for the pressure (see equations (27) and (28)). For the element used here, we have  $k = 2$ , and cellwise constant interpolation implies  $r = 1$ , so we need to expect the observed reduction in convergence order. Using a bilinear least-squares interpolation ( $r = 2$ ) shows an interesting behavior that was briefly observed, but not fully explored before [Thielmann et al.(2014)]: At low resolutions and for a constant number of particles per cell the velocity error decreases with nearly the expected rate of the direct method, but then degrades to second order convergence (not shown in the table, but see Figure 1 and compare also Figure 6b of [Thielmann et al.(2014)]). However, here we show that increasing the number of particles per cell approximately linearly with increasing resolution recovers the expected convergence rate of the Stokes element (last set of columns in Table 2 and Figure 1, top). This is a behavior that to our knowledge has not been described using geodynamic benchmark results before. We also note that our implementation seems to be less sensitive to the number of particles per cell since our convergence rate remains optimal to  $h = \frac{1}{512}$  for *PPC* = 256, while the implementation in [Thielmann et al.(2014)] degrades to second order at  $h \approx \frac{1}{128}$  for the

20 *R. Gassmöller, H. Lokavarapu, W. Bangerth, E. G. Puckett*

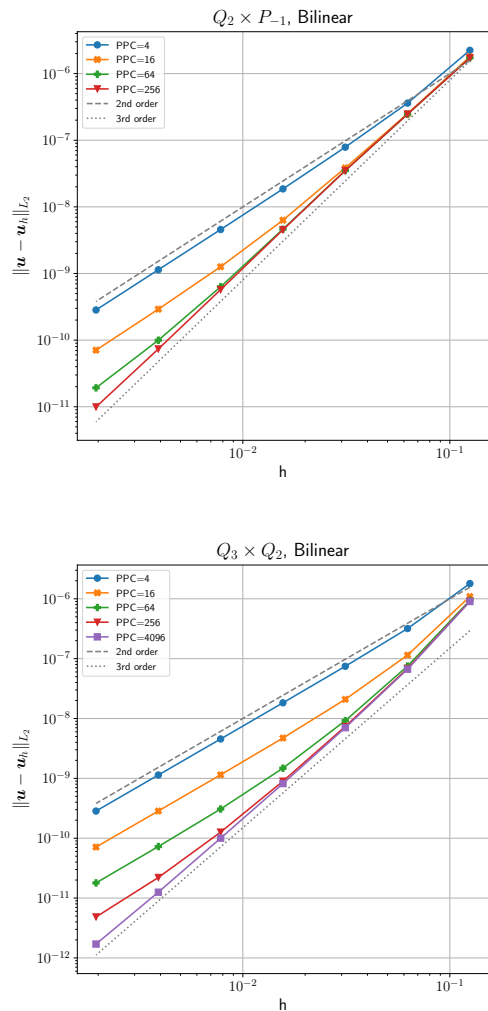


**Figure 1.** Velocity errors  $\|u - u_h\|_{L_2}$  for the SolKz benchmark for the  $Q_2 \times P_{-1}$  element ( $k = 2$ , top) and for the  $Q_3 \times Q_2$  element ( $k = 3$ , bottom), using bilinear interpolation ( $r = 2$ ). The error is plotted as a function of both mesh resolution ( $h$ ) and number of particles per cell ( $PPC$ ).

same number of particles per cell. We speculate that this is caused by our use of a bilinear approximation, instead of a linear one, as discussed in Section 3.4. The pressure error for the  $Q_2 \times P_{-1}$  element shown in Table 2 behaves as expected, it is suboptimal by one order for the arithmetic averaging and is identical to the direct method for the bilinear least squares interpolation; both results are independent of  $PPC$  (not shown in the table). All of these results are of course consistent with the predictions of Section 3.5 if one assumes a specific relationship for  $E(h, PPC)$  as further discussed below.

Recomputing the results above for the  $Q_3 \times Q_2$  Stokes element reveals some similarities, but also noteworthy variations. For the velocity, the direct method decreases the error with

## Evaluating hybrid finite element mesh/particle-in-cell methods 21

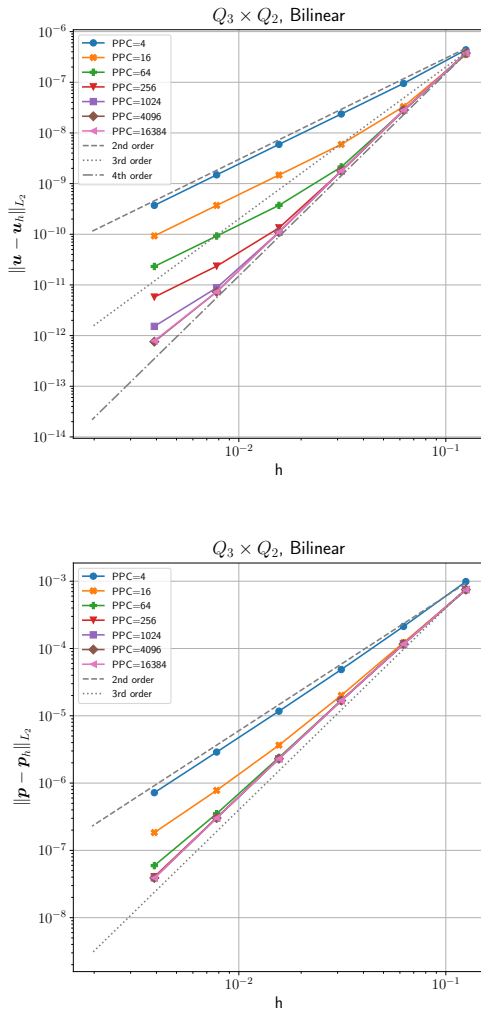


**Figure 2.** Velocity errors  $\|\mathbf{u} - \mathbf{u}_h\|_{L_2}$  (top) and pressure errors  $\|p - p_h\|_{L_2}$  (bottom) for the SolKz benchmark for the  $Q_3 \times Q_2$  element ( $k = 3$ ) and bilinear interpolation ( $r = 2$ ). The error is plotted as a function of both mesh resolution ( $h$ ) and number of particles per cell ( $PPC$ ). In contrast to Fig. 1, here we interpolate only the density from particles (that is, we use the exact viscosity in the assembly of the finite element linear system), and we recover 4th order convergence rate in velocity and 3rd order in pressure.

the expected fourth order. The arithmetic average interpolation method again achieves second order accuracy, which for this element is sub-optimal by two orders. The bilinear least-squares interpolation results in second order convergence with constant  $PPC$  (not shown in Table 2, but shown in Figure 1, bottom), and third order convergence with increasing  $PPC$ . However, as expected it is impossible to recover the fourth order convergence rate of the direct method with increasing  $PPC$ ; this is consistent with the theoretical prediction that the velocity error

22 *R. Gassmöller, H. Lokavarapu, W. Bangerth, E. G. Puckett*

converges at best with a rate of  $\min\{k + 1, r + 1\}$ , for  $k = 3$  and  $r = 2$ . As for the  $Q_2 \times P_{-1}$  element, these results are all consistent with the predictions of equations (27) and (28); the exception is that for arithmetic averaging, one would expect a first order convergence order for the pressure when in fact we observe order 1.5.

To further clarify the effect of the number of particles per cell on the convergence rate when using the bilinear interpolation scheme ( $r = 2$ ), Fig. 1 shows convergence data for the velocity error  $\|\mathbf{u} - \mathbf{u}_h\|_{L_2}$  as a function of both the mesh resolution ( $h$ ) and the number of particles per cell ( $PPC$ ). The plots show that the optimal convergence order can indeed be recovered for the  $Q_2 \times P_{-1}$  – but not the  $Q_3 \times Q_2$  – element, if one uses sufficiently many particles per cell. For both elements, the velocity error is well described by the approximation  $\|\mathbf{u} - \mathbf{u}_h\|_{L_2} = \mathcal{O}(h^3) + \mathcal{O}(h^2 PPC^{-1})$ . This can be compared with (28), predicting  $\mathcal{O}(h^{\min\{k+1, r+1\}}) + \mathcal{O}(h E(h, PPC))$ , to postulate a specific form for  $E(h, PPC)$ , namely  $E(h, PPC) = h PPC^{-1}$ . For the two parts of Fig. 1, we have  $k = 2$  or  $3$  and  $r = 2$ .

Figure 1 only shows velocity errors. We do not show corresponding figures for convergence data for the pressure error because for a bilinear reconstruction, the pressure converges at a fixed rate and is essentially independent of the number of particles per cell. Increasing the number of particles therefore does not increase the accuracy of the pressure, unlike for the velocity.

As a consequence of all of these considerations, for a fixed number of particles per cell – i.e., the only case that can be considered scalable to large problems with fine meshes –, both elements only yield an asymptotic convergence rate of  $\|\mathbf{u} - \mathbf{u}_h\|_{L_2} = \mathcal{O}(h^2)$ . In addition, it is worth mentioning that using 196, 361, or even 4,096 particles per cell would make particle advection in time dependent problems far more expensive than solving the Stokes equation, and that using the corresponding  $14^3 = 2,744$ ,  $19^3 = 6,859$  or even  $64^3 = 262,144$  particles per cell in three space dimensions is not a realistic option. Consequently, unless additional measures are taken, any practical use of particle methods combined with higher order finite elements will be prohibitively expensive for high mesh resolutions, or suffer from a sub-optimal convergence rate.

## Evaluating hybrid finite element mesh/particle-in-cell methods 23

**Table 3.** Velocity errors  $\|\mathbf{u} - \mathbf{u}_h\|_{L_2}$  and pressure errors  $\|p - p_h\|_{L_2}$  for the SolCx benchmark using the  $Q_2 \times P_{-1}$  Stokes element (top rows), and the  $Q_3 \times Q_2$  Stokes element (bottom rows). *PPC* (particles per cell),  $k$ , and  $r$  are as defined in Section 3.5.

$Q_2 \times P_{-1}$ ( $k = 2$ )								
$\ \mathbf{u} - \mathbf{u}_h\ _{L_2}$	direct method ( $r = \infty$ )		arithmetic average ( $r = 1$ )			bilinear least squares ( $r = 2$ )		
$h$	error	rate	<i>PPC</i>	error	rate	<i>PPC</i>	error	rate
$\frac{1}{8}$	$1.32 \cdot 10^{-5}$	-	4	$3.16 \cdot 10^{-5}$	-	4	$1.36 \cdot 10^{-5}$	-
$\frac{1}{16}$	$1.66 \cdot 10^{-6}$	2.99	4	$7.30 \cdot 10^{-6}$	2.12	4	$1.93 \cdot 10^{-6}$	2.81
$\frac{1}{32}$	$2.08 \cdot 10^{-7}$	3.00	4	$1.79 \cdot 10^{-6}$	2.03	9	$2.36 \cdot 10^{-7}$	3.03
$\frac{1}{64}$	$2.60 \cdot 10^{-8}$	3.00	4	$4.44 \cdot 10^{-7}$	2.01	25	$2.79 \cdot 10^{-8}$	3.08
$\frac{1}{128}$	$3.26 \cdot 10^{-9}$	3.00	4	$1.11 \cdot 10^{-7}$	2.00	49	$3.50 \cdot 10^{-9}$	3.00
$\frac{1}{256}$	$4.08 \cdot 10^{-10}$	3.00	4	$2.77 \cdot 10^{-8}$	2.00	100	$4.39 \cdot 10^{-10}$	3.00
$\frac{1}{512}$	$5.13 \cdot 10^{-11}$	3.00	4	$6.92 \cdot 10^{-9}$	2.00	196	$5.87 \cdot 10^{-11}$	2.90
$\ p - p_h\ _{L_2}$								
$\frac{1}{8}$	$1.48 \cdot 10^{-3}$	-	4	$3.16 \cdot 10^{-3}$	-	4	$1.53 \cdot 10^{-3}$	-
$\frac{1}{16}$	$3.7 \cdot 10^{-4}$	2.00	4	$8.00 \cdot 10^{-4}$	1.99	4	$3.83 \cdot 10^{-4}$	2.00
$\frac{1}{32}$	$9.22 \cdot 10^{-5}$	2.00	4	$2.00 \cdot 10^{-4}$	2.00	9	$9.29 \cdot 10^{-5}$	2.05
$\frac{1}{64}$	$2.30 \cdot 10^{-5}$	2.00	4	$5.00 \cdot 10^{-5}$	2.00	25	$2.30 \cdot 10^{-5}$	2.01
$\frac{1}{128}$	$5.75 \cdot 10^{-6}$	2.00	4	$1.25 \cdot 10^{-5}$	2.00	49	$5.75 \cdot 10^{-6}$	2.00
$\frac{1}{256}$	$1.44 \cdot 10^{-6}$	2.00	4	$3.12 \cdot 10^{-6}$	2.00	100	$1.44 \cdot 10^{-6}$	2.00
$\frac{1}{512}$	$3.59 \cdot 10^{-7}$	2.00	4	$7.80 \cdot 10^{-7}$	2.00	196	$3.59 \cdot 10^{-7}$	2.00
$Q_3 \times Q_2$ ( $k = 3$ )								
$\ \mathbf{u} - \mathbf{u}_h\ _{L_2}$	direct method ( $r = \infty$ )		arithmetic average ( $r = 1$ )			bilinear least squares ( $r = 2$ )		
$h$	error	rate	<i>PPC</i>	error	rate	<i>PPC</i>	error	rate
$\frac{1}{8}$	$6.04 \cdot 10^{-7}$	-	4	$3.15 \cdot 10^{-5}$	-	100	$9.10 \cdot 10^{-7}$	-
$\frac{1}{16}$	$4.03 \cdot 10^{-8}$	3.90	4	$7.29 \cdot 10^{-6}$	2.11	400	$5.84 \cdot 10^{-8}$	3.96
$\frac{1}{32}$	$2.60 \cdot 10^{-9}$	4.00	4	$1.79 \cdot 10^{-6}$	2.03	1600	$3.70 \cdot 10^{-9}$	3.98
$\frac{1}{64}$	$1.67 \cdot 10^{-10}$	4.00	4	$4.44 \cdot 10^{-7}$	2.01	6400	$2.34 \cdot 10^{-10}$	3.97
$\frac{1}{128}$	$1.98 \cdot 10^{-11}$	3.10	4	$1.11 \cdot 10^{-7}$	2.00	25600	$1.93 \cdot 10^{-11}$	3.60
$\frac{1}{256}$			4	$2.77 \cdot 10^{-8}$	2.00			
$\ p - p_h\ _{L_2}$								
$\frac{1}{8}$	$8.81 \cdot 10^{-3}$	-	4	$8.87 \cdot 10^{-3}$	-	100	$8.89 \cdot 10^{-3}$	-
$\frac{1}{16}$	$6.22 \cdot 10^{-3}$	0.50	4	$6.18 \cdot 10^{-3}$	0.52	400	$6.22 \cdot 10^{-3}$	0.51
$\frac{1}{32}$	$4.39 \cdot 10^{-3}$	0.50	4	$4.38 \cdot 10^{-3}$	0.50	1600	$4.39 \cdot 10^{-3}$	0.50
$\frac{1}{64}$	$3.1 \cdot 10^{-3}$	0.50	4	$3.10 \cdot 10^{-3}$	0.50	6400	$3.1 \cdot 10^{-3}$	0.50
$\frac{1}{128}$	$2.19 \cdot 10^{-3}$	0.50	4	$2.19 \cdot 10^{-3}$	0.50	25600	$2.19 \cdot 10^{-3}$	0.50
$\frac{1}{256}$			4	$1.55 \cdot 10^{-3}$	0.50			



24 *R. Gassmöller, H. Lokavarapu, W. Bangerth, E. G. Puckett*

## 4.2 SolCx

The second instantaneous benchmark we investigate is SolCx, where the viscosity is described by

$$\eta(x, y) = \begin{cases} 1 & \text{if } x < 0.5 \\ 10^6 & \text{if } x \geq 0.5, \end{cases} \quad (31)$$

and the density by

$$\rho(x, y) = -\sin(\pi y) \cos(\pi x), \quad (32)$$

all again on the unit square  $\Omega = (0, 1)^2$ . The complete derivation of the exact solution uses a propagator matrix method and is described in [Zhong(1996)]. The defining property of this benchmark is that the discontinuous viscosity implies a nearly discontinuous pressure field and a velocity field that has a kink. Consequently, we can generally not expect optimal convergence rates unless (i) the mesh is aligned with the discontinuity and (ii) we use a pressure finite element that is discontinuous. While these properties reduce the usefulness of the benchmark for general problems, it is useful for our investigation for an unrelated reason: While the density of the benchmark problem can only be approximated with the expected accuracy of the particle interpolation methods mentioned in Section 3.4 (namely  $O(h)$  for arithmetic averaging and  $O(h^2)$  for the bilinear least squares method), the viscosity is cell-wise constant if one uses a mesh that is aligned with the interface, as we will do here. The viscosity can therefore be interpolated exactly from particles to cells independent of the interpolation method. This allows us to separate influences from density and viscosity errors on the pressure and velocity solution. Specifically, within the analysis of Section 3.5, this implies that the error contribution labeled (2) does not exist for this benchmark and that, consequently, equations (27) and (28) can be replaced by

$$\|\mathbf{u} - \mathbf{u}_h\|_{L_2} = \mathcal{O}(h^{r+2}) + \mathcal{O}(h E(h, PPC)) + \mathcal{O}(h^{k+1}), \quad (33)$$

$$\|p - p_h\|_{L_2} = \mathcal{O}(h^{r+1}) + \mathcal{O}(E(h, PPC)) + \mathcal{O}(h^k). \quad (34)$$

In other words, as a function of the interpolation order  $r$ , the expected convergence order is one higher than in the general case represented by the SolKz benchmark discussed in the previous subsection.

Table 3 demonstrates convergence of the velocity and pressure for the  $Q_2 \times P_{-1}$  element (top rows), and the  $Q_3 \times Q_2$  element (bottom rows).

Starting with the  $Q_2 \times P_{-1}$  element ( $k = 2$ ) and the direct method ( $r = \infty$ , left-most columns of the top half of the table), the velocity error decreases with  $O(h^3)$  and the pressure

error with  $O(h^2)$  as expected and as reported previously [Kronbichler et al.(2012)], although half an order higher than reported in [Thielmann et al.(2014)]. Similarly, and as predicted by (33) and (34) above, when using particles and bilinear reconstructions ( $r = 2$ , right-most columns of the table), we obtain the same convergence rates as for the direct method. The one exception that violates our theoretical predictions is when using particles and arithmetic averaging ( $r = 1$ , middle columns) where the theory predicts third and second order convergence for velocity and pressure, respectively, but we only obtain second order for both. The table shows this for a constant number of particles per cell, suggesting that perhaps the term involving  $E(h, PPC)$  limits the convergence order; however, we have verified that even with large values of  $PPC$ , the convergence rate remains at two for the velocity. While we lack an understanding of why theory and practice do not agree here, we note that our data are consistent with previous results in [Thielmann et al.(2014)].

As described before [Kronbichler et al.(2012), Thielmann et al.(2014)], using a continuous pressure element like  $Q_3 \times Q_2$  ( $k = 3$ ) in general does not result in the optimal convergence rate for the pressure error because of the discontinuity in the pressure solution. Indeed, all methods to evaluate coefficients (independently of  $PPC$  choice) now only reach a pressure convergence rate of  $\mathcal{O}(h^{1/2})$  as shown in the bottom half of Table 3. Nevertheless, as expected for this benchmark despite the suboptimal pressure solution, the velocity error is still able to converge with the expected rates for the direct method ( $r = \infty$ , left-most columns) and the bilinear least-squares method ( $r = 2$ , right-most columns), namely  $\mathcal{O}(h^4)$ . However, in order to obtain the latter result, we now need to increase  $PPC \propto h^{-2}$ : using a constant number of particles per cell yields a suboptimal convergence order of  $\mathcal{O}(h^2)$ , whereas using  $PPC \propto h^{-1}$  results in  $\mathcal{O}(h^3)$ .

The outlier is again the velocity error when using the piecewise constant averaging ( $r = 1$ ) where one would expect third order convergence but we only observe second order.

The convergence orders predicted for the bilinear interpolation of the density – using  $PPC \propto h^{-2}$  – were one order higher than we saw for the SolKz benchmark when using  $PPC \propto h^{-1}$ . This conclusion followed from the fact that the viscosity interpolation for SolCx is exact, and remains unchanged if one tried to solve the benchmark with  $PPC \propto h^{-2}$ . In order to verify that this interpretation is in fact correct, we repeat the SolKz benchmark with a density that is interpolated from particles, but a viscosity that is exact (i.e., using the particles for density, but the direct method for viscosity) – see the results shown in Fig. 2. The  $Q_2 \times P_{-1}$  element shows no difference to the computations with interpolated viscosity, as they already reached the convergence order implied by the discretization error (not shown

1  
2  
3  
4 26 *R. Gassmöller, H. Lokavarapu, W. Bangerth, E. G. Puckett*

5 in the figure). However, the  $Q_3 \times Q_2$  element now also reaches the optimal convergence order  
6 for velocity (namely, 4) and pressure (i.e., 3). Moreover, to achieve this, we now also require  
7  $PPC \propto h^{-2}$  for the SolKz benchmark. All of this follows from the theoretical considerations  
8 of Section 3.5 and shows the usefulness of separating the total error into components that can  
9 be tested individually.

10  
11  
12  
13  
14 Finally, we have run additional tests in which the mesh cells are not aligned with the  
15 viscosity jump (by using an odd number of cells in each direction), and have confirmed previous  
16 results that a non-aligned jump limits the convergence order to  $\mathcal{O}(h^1)$  for the velocity and  
17  $\mathcal{O}(h^{1/2})$  for the pressure [Kronbichler et al.(2012), Thielmann et al.(2014)]. The choice of finite  
18 element, particle method, and number of particles per cell does not influence this result and  
19 does not limit the convergence order any further.

20  
21  
22  
23  
24 In summary, these experiments show the importance of the choice of  $PPC$  and particle  
25 interpolation method in practical applications, and that their optimal choices differ depending  
26 on whether the particles only carry density, or also viscosity information, and also depend on  
27 the continuity of the viscosity. In particular, we may need to grow the number of particles per  
28 cell as  $\mathcal{O}(h^{-1})$  or even  $\mathcal{O}(h^{-2})$  to retain the convergence order of the finite element scheme  
29 if the expected convergence order is better than  $\mathcal{O}(h^2)$ . This requires choosing between one  
30 of three options: (i) One needs to use a potentially very large number of particles per cell to  
31 retain the accuracy of the Stokes discretization, in particular if high accuracy is required or the  
32 computations are in three space dimensions. This may be prohibitively expensive, however:  
33 for example, in the  $Q_3 \times Q_2$  solution of the SolCx case with  $h = \frac{1}{128}$  and  $PPC = 25,600$  (see  
34 Table 3), the particle operations associated with the one time step we solve account for some  
35 95% of the overall run time. (ii) One accepts the loss of accuracy by using too few particles per  
36 cell, although that then calls into question the use of higher order polynomial spaces in the  
37 Stokes discretization. (iii) One develops methods with higher accuracy to project properties  
38 from particle locations to fields. An alternative is to use field-based – instead of a particle-  
39 based – descriptions of the temperature, chemical composition, or other advected quantities  
40 as discussed in [Kronbichler et al.(2012)]; in that case, the effort for the Stokes solve and the  
41 advection solve is automatically balanced.

42  
43  
44  
45  
46  
47  
48  
49  
50  
51  
52  
53 Finally, we want to emphasize that higher-order PIC (HOPIC) schemes with a constant  
54 number of particles per cell have been successfully developed for other applications like the  
55 shallow-water equation, and the vortex formulation of the Navier-Stokes equations [Edwards &  
56 Bridson(2012)]. In other words, we do not argue that the dependence on  $PPC$  is an intrinsic  
57 property of *any* higher-order PIC schemes, but is rather a consequence of the algorithmic  
58  
59  
60

differences between our methods and those implemented in [Edwards & Bridson(2012)]. It is apparent that determining the precise differences responsible provides a useful direction for future research.

## 5 TIME DEPENDENT BENCHMARKS

The previous section presented benchmarks that assess different strategies for the transfer of information from (stationary) particle locations back to the finite element mesh, along with the error that was introduced by this operation. On the other hand, in realistic applications, particles will be advected along, and consequently the overall error will contain contributions that are due to the transfer of particle information to the mesh, but also due to the fact that we only know particle locations up to the numerical error introduced in the integration of particle trajectories, as discussed in Section 3. We will here numerically test how large this overall error is, and what effect it has on the numerical solution of the Stokes equation when feeding information back to the Stokes solver.

To this end, we derive two different time-independent solutions to the Stokes equations (1)–(2), in an annulus and in a box, in which the exact density  $\rho$  is constant on streamlines. As we noted before a spatially varying viscosity would limit the convergence rate we could achieve with our interpolation methods, and might obscure the error of the particle advection method; consequently, we choose a constant viscosity. If one were to solve the Stokes equations with this setup, the solution would of course not change with time: because  $\rho$  is constant along streamlines, and because it is advected along these streamlines, it does not actually change with time. However, if the density (as part of the right hand side) is inexactly interpolated from particles in each time step, and particles are inexactly advected along with the computed velocity, then the numerical solution *will* change with time, and we can assess the accuracy of the particle-in-cell algorithm using the difference between exact (time independent) and computed (time dependent) solution. In our experiments, we will evaluate this numerical error for different values of the (largest) grid size  $h_{\max}$  and different numbers of particles per cell (*PPC*).

Given that we use a viscosity that is constant, the same considerations apply as for the SolCx benchmark in Section 4.2. Namely, one might expect that if the time discretization error is negligible, we could obtain the same convergence rates as shown in (33)–(34):

$$\begin{aligned} \|\mathbf{u}(t) - \mathbf{u}_h(t)\|_{L_2} &= \mathcal{O}(h^{\min\{k+1, r+2\}}) + \mathcal{O}(h E(h, PPC)), \\ \|p(t) - p_h(t)\|_{L_2} &= \mathcal{O}(h^{\min\{k, r+1\}}) + \mathcal{O}(E(h, PPC)). \end{aligned} \quad (35)$$

28 *R. Gassmüller, H. Lokavarapu, W. Bangerth, E. G. Puckett*

### 5.1 A time dependent benchmark in an annulus

For the first concrete realization of the approach outlined above, we need to construct a testcase with a steady-state velocity field that depends on a spatially non-constant density that we can advect along either as a field or with particles. We start by choosing the domain as a two-dimensional annulus with inner and outer radii  $R_1 = 1$  and  $R_2 = 2$ , respectively.

In this situation, we can express the equations and the solution in a cylindrical coordinate system in terms of the radius  $r$  and the azimuthal angle  $\theta$ . A solution of equations (1)–(2) can then be obtained by setting

$$\eta = 1, \quad \rho(r, \theta) = 48r^5, \quad \mathbf{g}(r, \theta) = \frac{r^3}{384}\mathbf{e}_r + \mathbf{e}_\theta, \quad (36)$$

where  $\mathbf{e}_r$  and  $\mathbf{e}_\theta$  are the radial and azimuthal unit vectors, respectively. Such a gravity vector is not the gradient of a gravity potential and consequently not physical, but this is of no importance here. The Stokes system can then be solved using a separation of variables approach and yields

$$\mathbf{u}(r, \theta) = 0\mathbf{e}_r - r^7\mathbf{e}_\theta, \quad p(r, \theta) = \frac{r^9}{72} - \frac{512}{72}, \quad (37)$$

for the velocity and pressure. In other words, the flow field is circular around the center with a velocity that varies with radius. Importantly, while all solution fields in question are polynomials in  $r$  and  $\theta$ , their degrees are sufficiently high so as to not be in the finite element spaces we use. The benchmark is then completely defined by prescribing  $\eta$  and  $\mathbf{g}$  as above, along with prescribed tangential velocity boundary values on the inner and outer boundaries of the annulus, and the initial distribution of  $\rho$ . Note, that while it seems unintuitive for a gravity in  $e_\theta$  direction to cause a flow in  $-e_\theta$  direction, one can think of this flow as being driven by the prescribed tangential velocity at the outer boundary, which is gradually reduced by the gravity with decreasing radius. A detailed derivation and visualization of this solution can be found in Appendix A and Fig. A1.

All experiments in this section show the error between the (stationary) exact solution  $\mathbf{u}$ ,  $p$ , and  $\rho$  and the (time-dependent) numerical approximation  $\mathbf{u}_h$ ,  $p_h$ , and  $\rho_h$  at time  $t = \frac{4\pi}{27} \approx 0.0982$ , which equals two complete revolutions of particles on the outer edge  $r = R_2$ .

### 5.2 Results of the time dependent annulus benchmark

If we use the exact (and unchanging) density when computing the numerical solution of the Stokes equation, one expects convergence to the exact solution with an appropriate power of

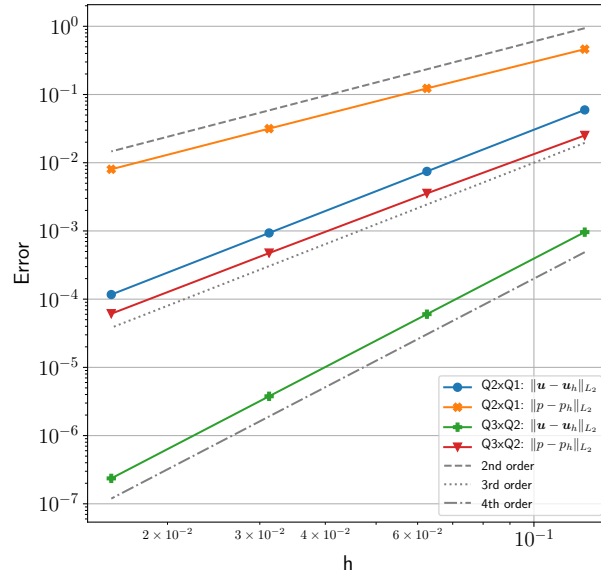


**Figure 3.** Convergence rates for the velocity  $\|\mathbf{u} - \mathbf{u}_h\|_{L_2}$  and pressure  $\|p - p_h\|_{L_2}$  for the time-dependent benchmark on the annulus using  $Q_2 \times Q_1$  and  $Q_3 \times Q_2$  element combinations, respectively. The results shown here use the exact density.

the mesh size. We verify that our solver achieves the expected convergence orders in Figure 3 for both  $Q_2 \times Q_1$  and  $Q_3 \times Q_2$  elements.

On the other hand, if the density in each time step is interpolated from particles to quadrature points, then the solution will vary from time step to time step due to the fact that particle locations are advected along with the numerical approximation of the velocity field  $\mathbf{u}$ .

Figure 4 shows convergence results for the  $Q_2 \times Q_1$  element ( $k = 2$ ) for the velocity and pressure. As was shown in the instantaneous benchmarks above (Section 4), the orders of convergence of the velocity and pressure error directly depend on the interpolation scheme, which also determines the convergence order for the error in density. The rates we observe in the figure exactly correspond to the predictions of (35) and (12), with one exception: For the velocity error with piecewise constant interpolation of the density (top left panel), we would have expected third order convergence ( $\min\{k + 1, r + 2\} = 3$ ) if the temporal error were negligible, whereas we only observe second order. Furthermore, this result is independent of PPC. We are unsure about the reasons for this, but note that it is consistent with observing the same phenomenon for the SolCx benchmark which uses a similar setup (see Section 4.2).

As expected, for the bilinear interpolation ( $r = 2$ ), the optimal convergence rate is only

30 *R. Gassmöller, H. Lokavarapu, W. Bangerth, E. G. Puckett*

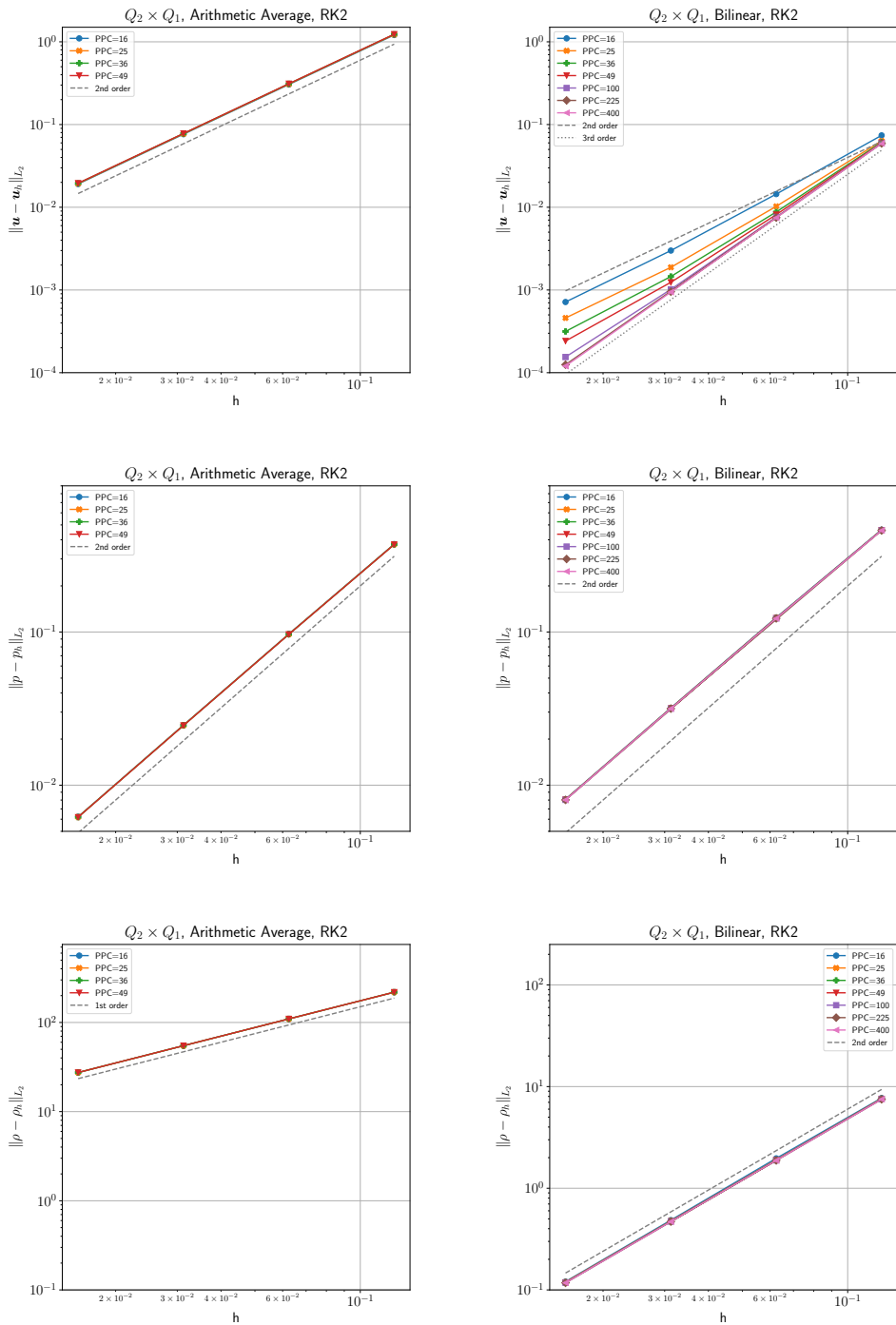


**Figure 4.** The convergence rate of  $\|\mathbf{u} - \mathbf{u}_h\|_{L_2}$  (top),  $\|p - p_h\|_{L_2}$  (middle), and  $\|\rho - \rho_h\|_{L_2}$  (bottom) measured at  $t = 4\pi/2^7$  for the time dependent benchmark. Density is carried on particles and is interpolated as cell-wise arithmetic average ( $r = 1$ , left) and bilinear least-squares interpolation ( $r = 2$ , right). All models use a  $Q_2 \times Q_1$  element ( $k = 2$ ) and RK2 to advect particles. Note that only with bilinear least-squares interpolation and an increasing number of particles per cell ( $PPC$ ) is the third order convergence rate of velocity recovered. In all cases,  $\|p - p_h\|_{L_2}$  converges at second-order rate with no apparent influence due to the number of  $PPC$  (i.e., all dots fall on each other), while the convergence rate of  $\|\rho - \rho_h\|_{L_2}$  depends on the interpolation scheme, but not on  $PPC$ .

recovered if the number of particles per cell is increased as the mesh is refined and the number of cells increases. This observation is consistent with our instantaneous benchmarks above, and the observation in [Thielmann et al.(2014)] that the convergence rate is suboptimal for constant  $PPC$ . All of these results are identical for the RK2 and RK4, advection schemes, which is why we only present the RK2 results.

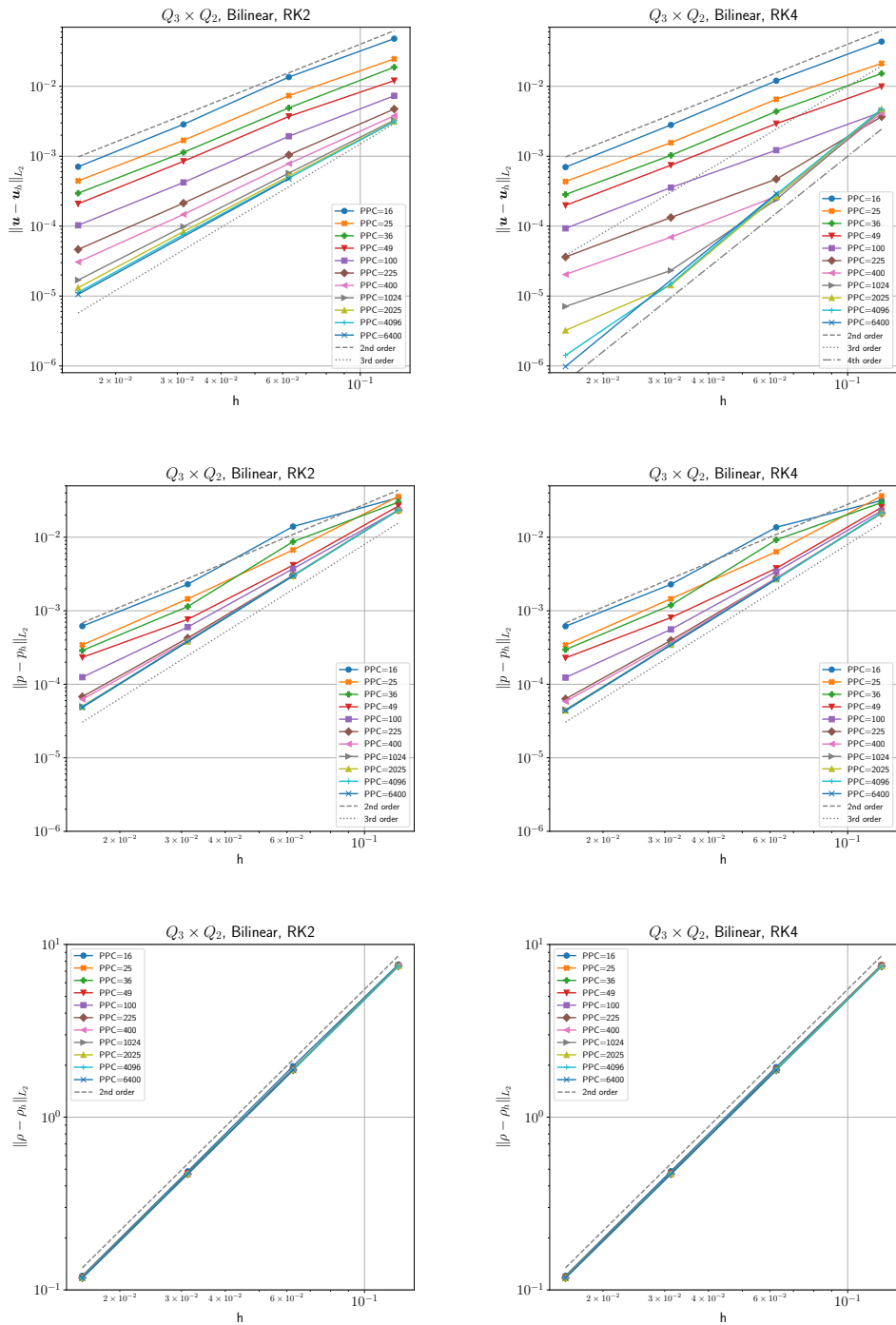
Figure 5 shows the corresponding results for the  $Q_3 \times Q_2$  element ( $k = 3$ ). For lack of any new information we omit the arithmetic averaging case ( $r = 1$ ) and instead compare the RK2 integration scheme to the RK4 integrator. We start by pointing out that the integration scheme (RK2 vs. RK4), the  $PPC$  (16 to 6400), and the finite element ( $Q_2 \times Q_1$  vs.  $Q_3 \times Q_2$ ) do not change the convergence rate of the density: it remains second-order accurate. However pressure and velocity show significant differences as predicted by (35). The only case where we obtain a lower convergence order than predicted by (35) is the velocity error when using the RK2 integrator (top left panel), which only reduces with third order where we would have expected fourth order ( $\min\{k + 1, r + 2\} = 4$ ). Interestingly, however, the expected order can be recovered by using the RK4 integrator and an increasing number of particles per cell (top right panel), suggesting that it is the temporal error that we neglected in deriving (35) that is responsible for the reduced order.

Figure 6 plots selected information from the two previous figures as velocity error over number of  $PPC$  for different finite elements, particle integration schemes, and mesh resolutions. In general all of the computations we made show a linear decrease of velocity error with increasing  $PPC$  (i.e.,  $E(h, PPC) \propto (PPC)^{-1}$  for fixed  $h$ ), which eventually transitions into a constant error at a model-specific number of  $PPC$  when the error sources (1), (2), and (4) of Section 3.5 begin to dominate over the error of the particle interpolation. The number of  $PPC$  at which the transition occurs can be interpreted as *optimal*, in the sense that it recovers the design rate of the finite element with the minimum number of particles. As can be seen from this figure, the optimal number of  $PPC$  is dependent on the finite element type and in the case of the  $Q_3 \times Q_2$  element also the particle integrator and in all configurations the mesh size. Most likely it will also depend on the problem one is solving. Therefore, the optimal number of  $PPC$  can not be accurately determined for practical applications except by performing a convergence series test with increasing  $PPC$  for the specific problem at the final resolution.

However, we propose that it is possible to determine a nearly optimal number of  $PPC$  for most problems on a coarse resolution, and then appropriately scale this number to the target resolution, considering the convergence order of the finite element ( $k$ ), the interpolation scheme



32 *R. Gassmöller, H. Lokavarapu, W. Bangerth, E. G. Puckett*



**Figure 5.** Panels as in Fig. 4, but for a  $Q_3 \times Q_2$  element ( $k = 3$ ). All models use the bilinear least squares interpolation ( $r = 2$ ). Columns represent RK2 (left) and RK4 (right) particle integration. Note that only with RK4, bilinear least-squares interpolation and an increasing number of particles per cell ( $PPC$ ) is the fourth order convergence rate of the velocity recovered. All properties with a design convergence rate higher than 2 require an increasing  $PPC$  to reach their design rate, while constant  $PPC$  only allows for second order convergence. The density is limited to second-order accuracy due to the chosen interpolation scheme ( $r = 2$ ).

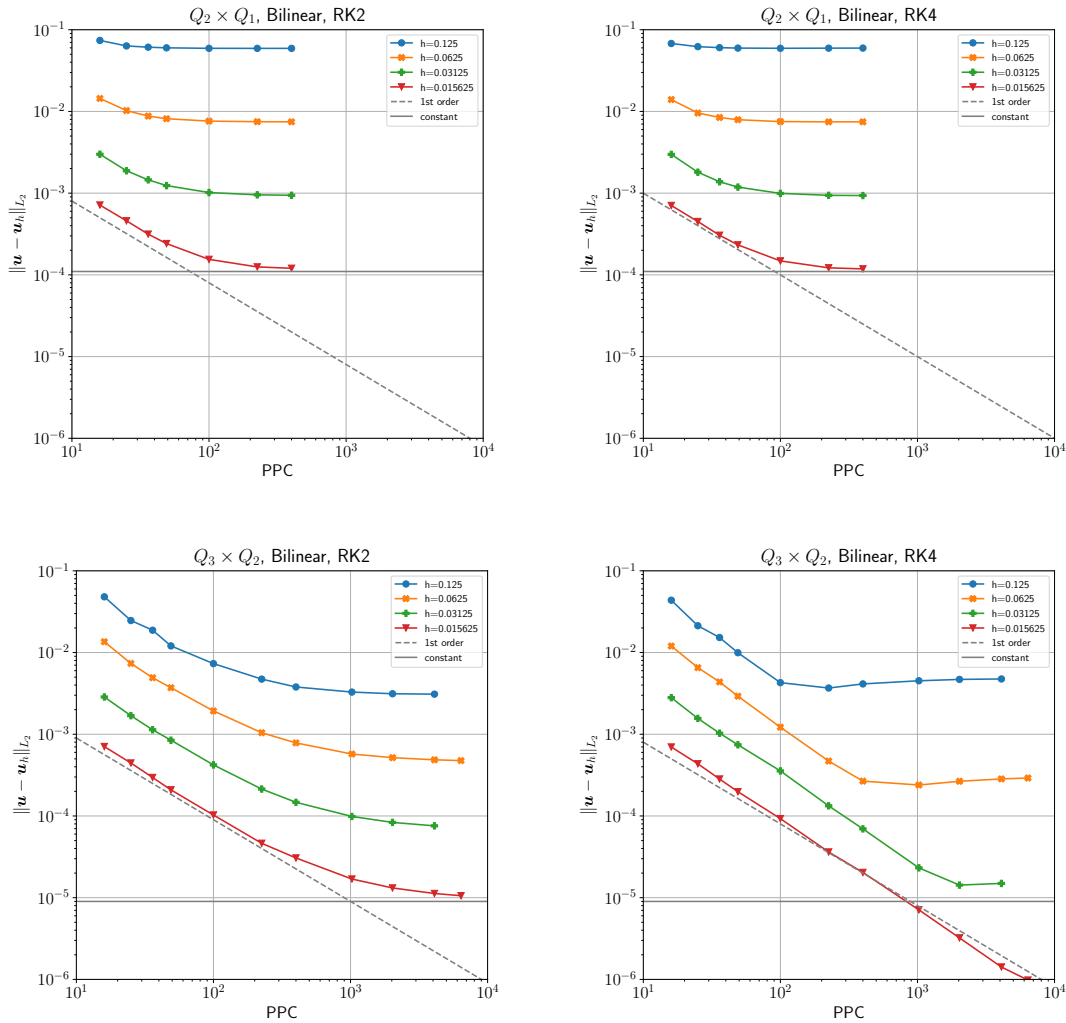


**Figure 6.** Convergence plots for velocity in the  $L_2$  norm for the time dependent annulus benchmark in dependence of the number of particles per cell ( $PPC$ ). Models were computed using a  $Q_2 \times Q_1$  finite element ( $k = 2$ , top) and  $Q_3 \times Q_2$  element ( $k = 3$ , bottom) respectively and particles were advected using a RK2 integration scheme (left) and RK4 integration scheme (right). Note that the required  $PPC$  to reach the minimum error for a given mesh refinement depends on the finite element and the mesh resolution  $h$  itself. The time integration scheme only plays a role if its convergence rate is lower than the convergence rate of the velocity element.

( $r$ ), and the type of properties carried on the particle (density or viscosity). To illustrate this consider the case presented in the top right panel of Figure 4, which uses the default values for  $k$  (namely, 2),  $r$  (2), and the RK2 integration scheme of our reference implementation in ASPECT. The series of models with increasing  $PPC$  shows that when using  $PPC = 16$ , the error is already sufficiently close to the error when using larger numbers of  $PPC$  for  $h = \frac{1}{8}$  to consider this number appropriate for this resolution. As determined above, the

1  
2  
3  
4 34 *R. Gassmöller, H. Lokavarapu, W. Bangerth, E. G. Puckett*

5  $PPC$ -dependent error term discussed in Section 3.5 scales as  $E(h, PPC) = \mathcal{O}(h^2 PPC^{-1})$ ;  
6 consequently, we need to chose  $PPC \propto h^{-1}$  to achieve the expected velocity error convergence  
7 order of  $\mathcal{O}(h^3)$ . Thus, choosing  $PPC = 32$  for  $h = \frac{1}{16}$  is a natural choice, as is  $PPC = 64$  for  
8  $h = \frac{1}{32}$  (in fact we would have done so for the figure, but our particle generation algorithm  
9 requires  $PPC$  to be the square of a natural number, which is why we chose closeby numbers).  
10 We hypothesize that the optimal values of  $PPC$  that we have found in this section will be  
11 close to optimal values for a variety of smooth problems, at least for the two-dimensional  
12 cases we have considered here. Therefore, while Section 3.5 provided the maximum possible  
13 convergence order one could expect, this section provided guidance on how to choose  $PPC$   
14 to actually achieve this convergence order.  
15  
16  
17  
18  
19  
20

21 Concluding this section we want to emphasize that for higher-order methods and high  
22 mesh resolutions, choosing a higher  $PPC$  might be a more important and cheaper (though  
23 less visible) improvement in accuracy than a higher mesh resolution  $h$ . Conversely choosing a  
24 low  $PPC$  can result in a significant (but usually invisible) degradation of the accuracy of the  
25 solution.  
26  
27  
28  
29  
30  
31  
32  
33  
34

### 35 5.3 A time dependent benchmark in a box

36 For the second realization of the time-dependent benchmark approach outlined above, we  
37 choose the domain as the two-dimensional unit box  $\Omega = (0, 1)^2$ .  
38  
39

40 For this situation, we can express the equations and the solution in a Cartesian coordinate  
41 system. A solution of equations (1)–(2) can then be obtained by setting  
42  
43

$$44 \quad \eta = 1, \quad (38)$$

$$45 \quad \rho(x, y) = \sin(\pi x) \sin(\pi y), \quad (39)$$

$$46 \quad \mathbf{g}(x, y) = -4\pi^2 \frac{\cos(\pi x)}{\sin(\pi x)} \mathbf{e}_y, \quad (40)$$

47  
48  
49  
50  
51 where  $\mathbf{e}_y$  is the vertical unit vector (pointing upwards). While the  $y$ -component of gravity  
52 becomes singular at  $x = 0$  and  $x = 1$ , the right-hand side of (1) only contains  $\rho \mathbf{g}$  and  
53 consequently remains non-singular. We avoid accidental division by zero when assembling the  
54 equations by additionally computing  $\rho \mathbf{g}$  on the particles before interpolating the product to  
55 the grid. For consistency with the annulus benchmark we also interpolate  $\rho$  when computing  
56 the interpolation error.  
57  
58  
59  
60

The Stokes system can then be solved and yields

$$\mathbf{u}(x, y) = \begin{bmatrix} \sin(\pi x) \cos(\pi y) \\ -\cos(\pi x) \sin(\pi y) \end{bmatrix}, \quad (41)$$

$$p(x, y) = 2\pi \cos(\pi x) \cos(\pi y) \quad (42)$$

for the velocity and pressure. The resulting flow field contains rotational and shear components and is tangential to all boundaries of the box. A detailed derivation and visualization of this solution can be found in Appendix B and Fig. A2.

All experiments for this benchmark show the error between the (stationary) exact solution  $\mathbf{u}$ ,  $p$ , and  $\rho$  and the (time-dependent) numerical approximation  $\mathbf{u}_h$ ,  $p_h$ , and  $\rho_h$  at time  $t = 0.1$ , which equals  $\frac{1}{20}$  of a complete revolution of the center of the model. We did not run the benchmark for a full revolution, because as described in an earlier study [Samuel(2018)] the found flow field requires a particle rebalancing algorithm as regions of the model are sufficiently stretched to lose all particles. To avoid the complication of measuring the accuracy of particle splitting/merging algorithms we limited the model time.

The results of this benchmark setup are consistent with the results described for the annulus geometry in Section 5.2. The particle interpolation algorithm plays a crucial role in retaining the expected convergence order of the finite-element, and the particle advection scheme can limit the convergence order if its convergence order is lower than the one of the interpolation scheme. For lack of new information the corresponding figures are presented in Appendix C. This experiment shows that the interpretations of Section 5.2 are independent of model geometry.

## 6 CONCLUSIONS

In this manuscript we have used existing and developed new benchmarks to measure the accuracy and convergence rate of hybrid finite element/particle-in-cell methods and provided reference results for these benchmarks obtained with the geodynamic modeling code ASPECT. In particular, we have presented the first analytical benchmarks that measure the accuracy and convergence order of a time-dependent flow problem in a 2D spherical annulus or a 2D unit box using particles to carry material properties. Since the two benchmarks are simple to derive and implement, they can be used as a convenient measure for the correctness of future implementations of similar algorithms, or as a common model for code comparisons.

Additionally, we have investigated the influence of different interpolation algorithms for transferring information from the particles to the cells and determined that in order to retain

1  
2  
3 36 *R. Gassmöller, H. Lokavarapu, W. Bangerth, E. G. Puckett*  
4

5 the optimal convergence rate of high-order finite element formulations, one needs to use a  
6 sufficiently high-order particle interpolation algorithm. Of course the overall convergence rate  
7 of a model is also bounded by the application in question: models with discontinuous material  
8 properties are limited to lower order accuracy if the mesh is not aligned with the discontinu-  
9 ities. This assertion is backed up by a theoretical analysis of the error contributions, predicting  
10 the observed convergence orders of the presented benchmark cases. Among the error contri-  
11 butions are (i) the discretization error due to using finite element methods on meshes of finite  
12 cell size, (ii) the error introduced by replacing the exact density and viscosity functions with  
13 ones obtained by interpolating information from particles to (low-order) polynomial spaces,  
14 and (iii) the error introduced by using a finite number of particles per cell.  
15  
16  
17  
18  
19  
20  
21  
22  
23

24 The design of better and more accurate methods than the ones we have presented here will  
25 need to address all of these error sources. For the first of the error contributions mentioned  
26 above, this may involve the use of higher order finite element methods and/or finer meshes;  
27 both of these options are well understood and frequently used. The second error would involve  
28 interpolating data from particle locations onto polynomials of degree larger than one, for  
29 example onto quadratic polynomials ( $r = 3$ ) rather than the constant ( $r = 1$ ) or linear ones  
30 ( $r = 2$ ) used here. However, this has substantial drawbacks, for example the fact that it  
31 is often difficult to determine in practice whether a quadratic function in two or three space  
32 dimensions is strictly positive, as one would hope the density and viscosity are; more generally,  
33 the question of minimizing unwanted variability of the interpolant needs to be addressed. For  
34 the third error source, the experiments we have shown suggest that one may need to increase  
35 the number of particles per cell as one refines the mesh, and we have provided guidance on how  
36 many particles per cell to choose for smooth problems to retain the intended convergence rate.  
37 Nevertheless, while the exact number of particles per cell necessary to achieve the designed  
38 convergence rate may be problem-dependent, the fact that it is resolution dependent to begin  
39 with raises the question of the scalability of the method, since either a loss of convergence  
40 rate (e.g., with a constant number of particles per cell) needs to be accepted; or the number  
41 of particles will need to increase substantially faster than the number of cells, resulting in  
42 computations in which operations on particles account for the vast majority of CPU cycles  
43 spent on a simulation. As shown by the error analysis, this error source does not disappear  
44 just because one uses a higher order interpolation scheme to transfer data from particles to  
45 the mesh. As a consequence, we are not aware of a simple, cheap, and obvious method to reach  
46 high convergence rates using such particle-in-cell methods with higher-order finite elements,  
47  
48  
49  
50  
51  
52  
53  
54  
55  
56  
57  
58  
59  
60

although it is quite possible that the methods we have presented yield an accuracy that is sufficient for practical geodynamic simulations.

## ACKNOWLEDGMENTS

All models were computed with the open source software ASPECT [Bangerth et al.(2018), <https://aspect.geodynamics.org>] version 2.1.0.pre (git commit hash a42335f33, the time dependent box benchmark was added later in commit hash 67f2623f3). ASPECT is published under the GPL2 license, and the necessary data to reproduce the models is included in the software. We thank the Computational Infrastructure for Geodynamics (<https://geodynamics.org>) – which is funded by the National Science Foundation under awards EAR-0949446 and EAR-1550901 – for supporting the development of ASPECT.

W.B., R.G., H.L. and E.G.P. jointly wrote the manuscript; E.G.P., R.G. and H.L. derived the time-dependent benchmark setups; H.L. and R.G. performed the computations; R.G., E.G.P., and H.L. analyzed the benchmark results. W.B. developed the theoretical error analysis.

R. Gassmüller and W. Bangerth were partially supported by the National Science Foundation under award OCI-1148116 as part of the Software Infrastructure for Sustained Innovation (SI2) program; and by the Computational Infrastructure in Geodynamics initiative (CIG), through the National Science Foundation under Awards No. EAR-0949446, EAR-1550901 and The University of California – Davis. W. Bangerth was also supported by the National Science Foundation under Award OAC-1835673.

E. G. Puckett was supported by the National Science Foundation under Award ACI-1440811 as part of the SI2 Scientific Software Elements (SSE) program.

The computational resources were provided by the Computational Infrastructure for Geodynamics. Computations were run on the distributed computing cluster Peloton of the U.C. Davis Division of Mathematical and Physical Sciences, and the Stampede2 system at the Texas Advanced Computing Center (TACC).

## REFERENCES

- Bangerth, W., Dannberg, J., Gassmüller, R., Heister, T., et al., 2018. ASPECT: Advanced Solver for Problems in Earth's ConvecTion, User Manual, doi:10.6084/m9.figshare.4865333.
- Bercovier, M. & Pironneau, O., 1979. Error estimates for finite element method solution of the stokes problem in the primitive variables, *Numerische Mathematik*, **33**(2), 211–224.

1  
2  
3  
4 38 *R. Gassmüller, H. Lokavarapu, W. Bangerth, E. G. Puckett*

5 Brenner, S. & Scott, R., 2007. *The mathematical theory of finite element methods*, vol. 15, Springer  
6 Science & Business Media.

7  
8 Brooks, A. N. & Hughes, T. J., 1982. Streamline upwind/petrov-galerkin formulations for convection  
9 dominated flows with particular emphasis on the incompressible navier-stokes equations, *Computer  
10 methods in applied mechanics and engineering*, **32**(1-3), 199–259.

11  
12  
13 Dannberg, J. & Gassmüller, R., 2018. Chemical trends in ocean islands explained by plume–slab  
14 interaction, *Proceedings of the National Academy of Sciences*, **115**(17), 4351–4356.

15  
16 Dannberg, J., Eilon, Z., Faul, U., Gassmüller, R., Moulik, P., & Myhill, R., 2017. The importance of  
17 grain size to mantle dynamics and seismological observations, *Geochemistry, Geophysics, Geosys-  
18 tems*, **18**(8), 3034–3061.

19  
20 Deubelbeiss, Y. & Kaus, B., 2008. Comparison of eulerian and lagrangian numerical techniques for the  
21 stokes equations in the presence of strongly varying viscosity, *Physics of the Earth and Planetary  
22 Interiors*, **171**(1-4), 92–111.

23  
24 Donea, J. & Huerta, A., 2003. *Finite element methods for flow problems*, John Wiley & Sons.

25  
26 Duretz, T., May, D. A., Gerya, T. V., & Tackley, P. J., 2011. Discretization errors and free surface  
27 stabilization in the finite difference and marker-in-cell method for applied geodynamics: A numerical  
28 study, *Geochemistry, Geophysics, Geosystems*, **12**(7), Q07004.

29  
30 Edwards, E. & Bridson, R., 2012. A high-order accurate particle-in-cell method, *International Journal  
31 for Numerical Methods in Engineering*, **90**(9), 1073–1088.

32  
33 Evans, M. W., Harlow, F. H., & Bromberg, E., 1957. The particle-in-cell method for hydrodynamic  
34 calculations, Tech. rep., Los Alamos National Laboratory.

35  
36 Fischer, R. & Gerya, T., 2016. Early earth plume-lid tectonics: A high-resolution 3d numerical mod-  
37 elling approach, *Journal of Geodynamics*, **100**, 198–214.

38  
39 Gassmüller, R., Dannberg, J., Bredow, E., Steinberger, B., & Torsvik, T. H., 2016. Major influence  
40 of plume-ridge interaction, lithosphere thickness variations, and global mantle flow on hotspot  
41 volcanism—the example of tristan, *Geochemistry, Geophysics, Geosystems*, **17**(4), 1454–1479.

42  
43 Gassmüller, R., Lokavarapu, H., Heien, E., Puckett, E. G., & Bangerth, W., 2018. Flexible and  
44 scalable particle-in-cell methods with adaptive mesh refinement for geodynamic computations,  
45 *Geochemistry, Geophysics, Geosystems*, **19**(9), 3596–3604.

46  
47 Gerya, T., 2009. *Introduction to numerical geodynamic modelling*, Cambridge University Press.

48  
49 Gerya, T. V. & Yuen, D. A., 2003. Characteristics-based marker-in-cell method with conservative  
50 finite-differences schemes for modeling geological flows with strongly variable transport properties,  
51 *Physics of the Earth and Planetary Interiors*, **140**(4), 293–318.

52  
53 Gilbarg, D. & Trudinger, N. S., 1983. *Elliptic Partial Differential Equations of Second Order*, Springer,  
54 Heidelberg, 2nd edn.

55  
56  
57 Guermond, J.-L. & Pasquetti, R., 2011. Entropy viscosity method for high-order approximations of  
58 conservation laws, in Spectral and high order methods for partial differential equations, pp. 411–  
59 60

*Evaluating hybrid finite element mesh/particle-in-cell methods* 39

418, Springer.

Harlow, F. H. & Welch, J. E., 1965. Numerical calculation of time-dependent viscous incompressible flow of fluid with free surface, *The Physics of Fluids*, **8**(12), 2182–2189.

Heister, T., Dannberg, J., Gassmüller, R., & Bangerth, W., 2017. High accuracy mantle convection simulation through modern numerical methods – II: Realistic models and problems, *Geophys. J. Int.*, **210**(2), 833–851.

Hirt, C. W. & Nichols, B. D., 1981. Volume of fluid (VOF) method for the dynamics of free boundaries, *Journal of Computational Physics*, **39**(1), 201–225.

Ismail-Zadeh, A. & Tackley, P., 2010. *Computational methods for geodynamics*, Cambridge University Press.

Kronbichler, M., Heister, T., & Bangerth, W., 2012. High accuracy mantle convection simulation through modern numerical methods, *Geophysical Journal International*, **191**(1), 12–29.

McNamara, A. K. & Zhong, S., 2004. Thermochemical structures within a spherical mantle: Superplumes or piles?, *Journal of Geophysical Research*, **109**(B7), 1–14.

McNamara, A. K. & Zhong, S., 2005. Thermochemical structures beneath Africa and the Pacific Ocean, *Nature*, **437**(7062), 1136.

Meyer, D. & Jenny, P., 2004. Conservative velocity interpolation for pdf methods, in PAMM: Proceedings in Applied Mathematics and Mechanics, vol. 4, pp. 466–467, Wiley Online Library.

Moresi, L., Dufour, F., & Mühlhaus, H. B., 2003. A Lagrangian integration point finite element method for large deformation modeling of viscoelastic geomaterials, *Journal of Computational Physics*, **184**, 476–497.

Mulyukova, E. & Bercovici, D., 2018. Collapse of passive margins by lithospheric damage and plunging grain size, *Earth and Planetary Science Letters*, **484**, 341–352.

Poliakov, A. & Podladchikov, Y., 1992. Diapirism and topography, *Geophysical Journal International*, **109**(3), 553–564.

Popov, A. A. & Sobolev, S. V., 2008. SLIM3D: A tool for three-dimensional thermomechanical modeling of lithospheric deformation with elasto-visco-plastic rheology, *Physics of the Earth and Planetary Interiors*, **171**, 55–75.

Puckett, E. G., Turcotte, D. L., Kellogg, L. H., He, Y., Robey, J. M., & Lokavarapu, H., 2017. New numerical approaches for modeling thermochemical convection in a compositionally stratified fluid, *arXiv preprint arXiv:1703.02202*.

Pusok, A. E., Kaus, B. J., & Popov, A. A., 2017. On the quality of velocity interpolation schemes for marker-in-cell method and staggered grids, *Pure and Applied Geophysics*, **174**(3), 1071–1089.

Revenaugh, J. & Parsons, B., 1987. Dynamic topography and gravity anomalies for fluid layers whose viscosity varies exponentially with depth, *Geophysical Journal International*, **90**(2), 349–368.

Rozel, A., Ricard, Y., & Bercovici, D., 2011. A thermodynamically self-consistent damage equation for grain size evolution during dynamic recrystallization, *Geophysical Journal International*, **184**(2),



- 1  
2  
3  
4 40 *R. Gassmöller, H. Lokavarapu, W. Bangerth, E. G. Puckett*  
5  
6 719–728.
- 7 Samuel, H., 2018. A deformable particle-in-cell method for advective transport in geodynamic mod-  
8 elling, *Geophysical Journal International*, **214**(3), 1744–1773.
- 9 Schubert, G., Turcotte, D. L., & Olson, P., 2001. *Mantle Convection in the Earth and Planets, Part*  
10 *1*, Cambridge University Press.
- 11 Tackley, P. J., 1998. Thermo-chemical basal boundary layer: D"? , *The core-mantle boundary region*,  
12 p. 231.
- 13 Tackley, P. J. & King, S. D., 2003. Testing the tracer ratio method for modeling active compositional  
14 fields in mantle convection simulations, *Geochemistry, Geophysics, Geosystems*, **4**(4).
- 15 Taylor, C. & Hood, P., 1973. A numerical solution of the Navier-Stokes equations using the finite  
16 element technique, *Computers & Fluids*, **1**(1), 73–100.
- 17 Thielmann, M., May, D. A., & Kaus, B. J. P., 2014. Discretization errors in the hybrid finite element  
18 particle-in-cell method, *Pure and Applied Geophysics*, **171**(9), 2165–2184.
- 19 Thielmann, M., Rozel, A., Kaus, B., & Ricard, Y., 2015. Intermediate-depth earthquake generation and  
20 shear zone formation caused by grain size reduction and shear heating, *Geology*, **43**(9), 791–794.
- 21 van Keken, P. E., King, S. D., Schmeling, H., Christensen, U. R., Neumeister, D., & Doin, M.-P., 1997.  
22 A comparison of methods for the modeling of thermochemical convection, *Journal of Geophysical*  
23 *Research: Solid Earth*, **102**(B10), 22477–22495.
- 24 Wang, H., Agrusta, R., & Hunen, J., 2015. Advantages of a conservative velocity interpolation (CVI)  
25 scheme for particle-in-cell methods with application in geodynamic modeling, *Geochemistry, Geo-*  
26 *physics, Geosystems*, **16**(6).
- 27 Zhong, S., 1996. Analytic solutions for Stokes' flow with lateral variations in viscosity, *Geophysical*  
28 *Journal International*, **124**(1), 18–28.
- 29  
30  
31  
32  
33  
34  
35  
36  
37  
38  
39  
40  
41

## 42 APPENDIX A: DERIVATION OF AN INCOMPRESSIBLE STOKES 43 SOLUTION ON AN ANNULUS 44

45  
46 In order to derive the solution of the Stokes problem discussed in Section 5.1, we consider  
47 the Stokes equations (1)–(2) in polar coordinates. Since we will impose Dirichlet boundary  
48 conditions along all boundaries, and since we only consider an isoviscous fluid with  $\eta = 1$ , the  
49 equations can be simplified to  
50

$$51 \quad -\Delta \mathbf{u} + \nabla p = \rho \mathbf{g}, \quad (\text{A.1})$$

$$52 \quad \nabla \cdot \mathbf{u} = 0. \quad (\text{A.2})$$

53  
54  
55 In a polar coordinate system with  $r = \sqrt{x^2 + y^2}$  and  $\theta = \arctan \frac{y}{x}$ , we can express the  
56 Laplace operator, gradient, and divergence operators in terms of  $\frac{\partial}{\partial r}$  and  $\frac{\partial}{\partial \theta}$ . The incompressible  
57  
58  
59  
60

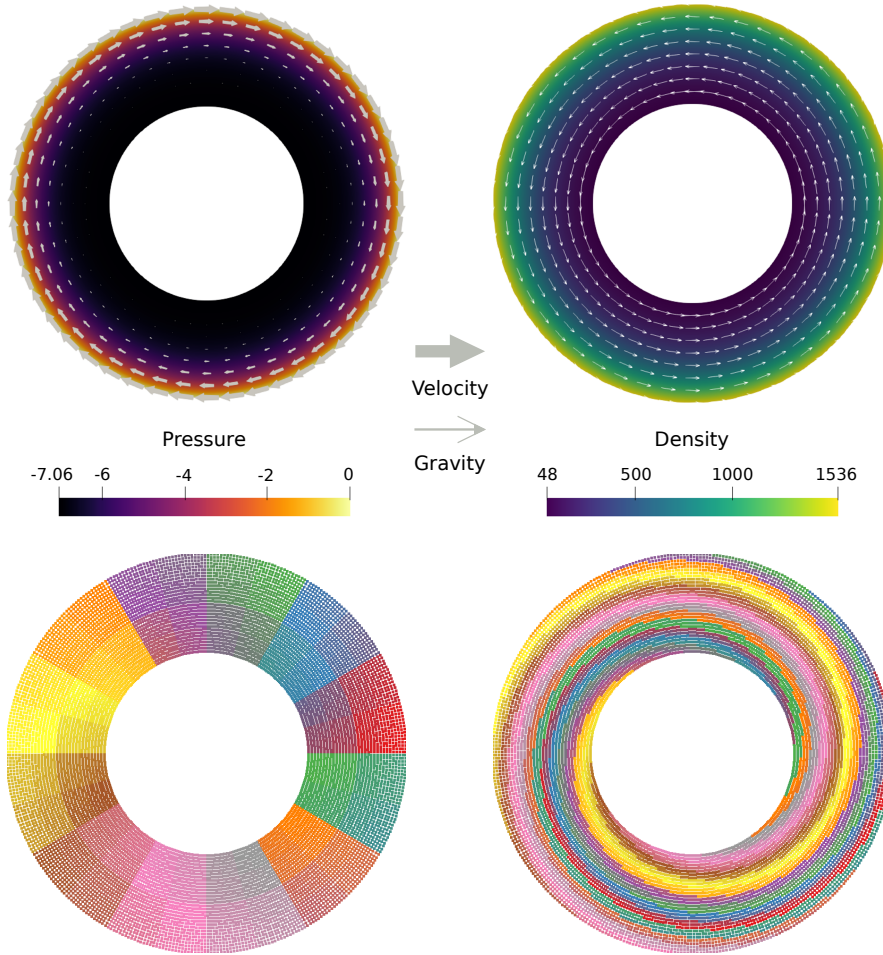


**Figure A1.** Solution of the annular flow benchmark. Top left: The velocity and pressure solution of the benchmark. Top right: Density and gravity fields that determine the right hand side of the Stokes system. Bottom row: Initial and final particle distributions after one full revolution of the outer edge, colored by particle index.

Stokes equations (A.1) and (A.2) then become

$$-\left(\frac{\partial^2 u_r}{\partial r^2} + \frac{1}{r} \frac{\partial u_r}{\partial r} + \frac{1}{r^2} \frac{\partial^2 u_r}{\partial \theta^2} - \frac{1}{r^2} u_r - \frac{2}{r^2} \frac{\partial u_\theta}{\partial \theta}\right) + \frac{\partial p}{\partial r} = \rho g_r, \quad (\text{A.3})$$

$$-\left(\frac{\partial^2 u_\theta}{\partial r^2} + \frac{1}{r} \frac{\partial u_\theta}{\partial r} + \frac{1}{r^2} \frac{\partial^2 u_\theta}{\partial \theta^2} - \frac{1}{r^2} u_\theta + \frac{2}{r^2} \frac{\partial u_r}{\partial \theta}\right) + \frac{1}{r} \frac{\partial p}{\partial \theta} = \rho g_\theta, \quad (\text{A.4})$$

$$\frac{1}{r} \frac{\partial(r u_r)}{\partial r} + \frac{1}{r} \frac{\partial u_\theta}{\partial \theta} = 0. \quad (\text{A.5})$$

We can find a solution by introducing the “stream function”  $\psi(r, \theta)$ , and expressing the

42 *R. Gassmöller, H. Lokavarapu, W. Bangerth, E. G. Puckett*

velocity through it:

$$u_r = \frac{1}{r} \frac{\partial \psi}{\partial \theta} \quad \text{and} \quad u_\theta = -\frac{\partial \psi}{\partial r}. \quad (\text{A.6})$$

By this construction, the velocity field  $\mathbf{u}$  then automatically satisfies the continuity equation (A.5).

We proceed by assuming that the the stream function is separable, i.e., that it can be expressed in the form  $\psi(r, \theta) = F(r)G(\theta)$  for functions  $F, G$  still to be determined. This form then immediately implies  $u_r = \frac{1}{r}F(r)G'(\theta)$  and  $u_\theta = -F'(r)G(\theta)$ . Thus, equations (A.3) and (A.4) become

$$\begin{aligned} & -\left(\frac{1}{r}F''G' + \frac{1}{r^2}F'G' + \frac{1}{r^3}FG'\right. \\ & \left. + \frac{1}{r^3}FG''' - \frac{1}{r^3}FG' + \frac{2}{r^2}F'G'\right) = -\frac{\partial p}{\partial r} + \rho g_r, \end{aligned} \quad (\text{A.7})$$

$$\begin{aligned} & -\left(-F'''G - \frac{1}{r}F''G - \frac{1}{r^2}F'G''\right. \\ & \left. + \frac{1}{r^2}F'G + \frac{2}{r^3}FG''\right) = -\frac{1}{r}\frac{\partial p}{\partial \theta} + \rho g_\theta. \end{aligned} \quad (\text{A.8})$$

We can obtain a solution of this set of equations in the spirit of manufactured solutions by choosing  $F(r) = \frac{1}{8c}r^8$  and  $G(\theta) = c$  where  $c$  can be any nonzero constant. This corresponds to a flow field with no radial component  $u_r = 0$  and a constant (but radially variable) angular velocity  $u_\theta = -r^7$ . Since  $F$  and  $G$  always appear as a product,  $c$  can be chosen arbitrarily and we will set it to  $c = 1$ .

Using this form then still requires us to find appropriate expressions for the pressure  $p(r, \theta)$ , the density  $\rho(r, \theta)$ , and the gravity vector  $\mathbf{g} = (g_r, g_\theta)$  to satisfy the governing equations. Since  $\rho$  only appears in a product with the gravity vector, we set

$$\rho(r, \theta) = 48r^5, \quad (\text{A.9})$$

ensuring that it is spatially variable but constant along streamlines.

Further substituting all of these expressions into (A.7)–(A.8) then yields

$$0 = -\frac{\partial p}{\partial r} + 48r^5 g_r, \quad (\text{A.10})$$

$$48r^5 = -\frac{1}{r}\frac{\partial p}{\partial \theta} + 48r^5 g_\theta. \quad (\text{A.11})$$

If we assume a radially outward gravity component  $g_r = \frac{r^3}{384}$ , this implies that

$$0 = -\frac{\partial p}{\partial r} + \frac{r^8}{8}. \quad (\text{A.12})$$

Integrating with respect to  $r$  and normalizing the pressure such that at the outer boundary

$r = R_2 = 2$  we have  $p(r = R_2, \theta) = 0$ , yields

$$p(r, \theta) = \frac{r^9}{72} - \frac{512}{72}. \quad (\text{A.13})$$

Given this pressure, the final remaining equation, (A.11), is

$$48r^5 = 48r^5 g_\theta. \quad (\text{A.14})$$

This results in  $g_\theta = 1$ .

In summary, our constructed solution is as follows:

$$\mathbf{u} = \begin{bmatrix} 0 \\ -r^7 \end{bmatrix}, \quad (\text{A.15})$$

$$p = \frac{r^9}{72} - \frac{512}{72}, \quad (\text{A.16})$$

$$\rho = 48r^5, \quad (\text{A.17})$$

$$\mathbf{g} = \begin{bmatrix} \frac{r^3}{384} \\ 1 \end{bmatrix}. \quad (\text{A.18})$$

## APPENDIX B: DERIVATION OF AN INCOMPRESSIBLE STOKES SOLUTION IN A BOX

In order to derive the solution of the Stokes problem discussed in Section 5.1, we consider the Stokes equations (1)–(2) in Cartesian coordinates. As before, we only consider an isoviscous fluid with  $\eta = 1$ . The equations are then

$$-\Delta \mathbf{u} + \nabla p = \rho \mathbf{g}, \quad (\text{B.1})$$

$$\nabla \cdot \mathbf{u} = 0. \quad (\text{B.2})$$

We find a solution by introducing a variation of a previously described stream function  $\psi(x, y) = \frac{1}{\pi} \sin(\pi x) \sin(\pi y)$  [van Keken et al.(1997), Samuel(2018)], and expressing the velocity through it:

$$u_x = \frac{\partial \psi}{\partial y} = \sin(\pi x) \cos(\pi y) \quad (\text{B.3})$$

$$u_y = -\frac{\partial \psi}{\partial x} = -\cos(\pi x) \sin(\pi y). \quad (\text{B.4})$$

Using this construction, the velocity field  $\mathbf{u}$  automatically satisfies the continuity equation (B.2), is tangential to all boundaries of a unit box, and contains both shear and rotational components.

Completing the solution then requires us to find appropriate expressions for the pressure

44 *R. Gassmöller, H. Lokavarapu, W. Bangerth, E. G. Puckett*

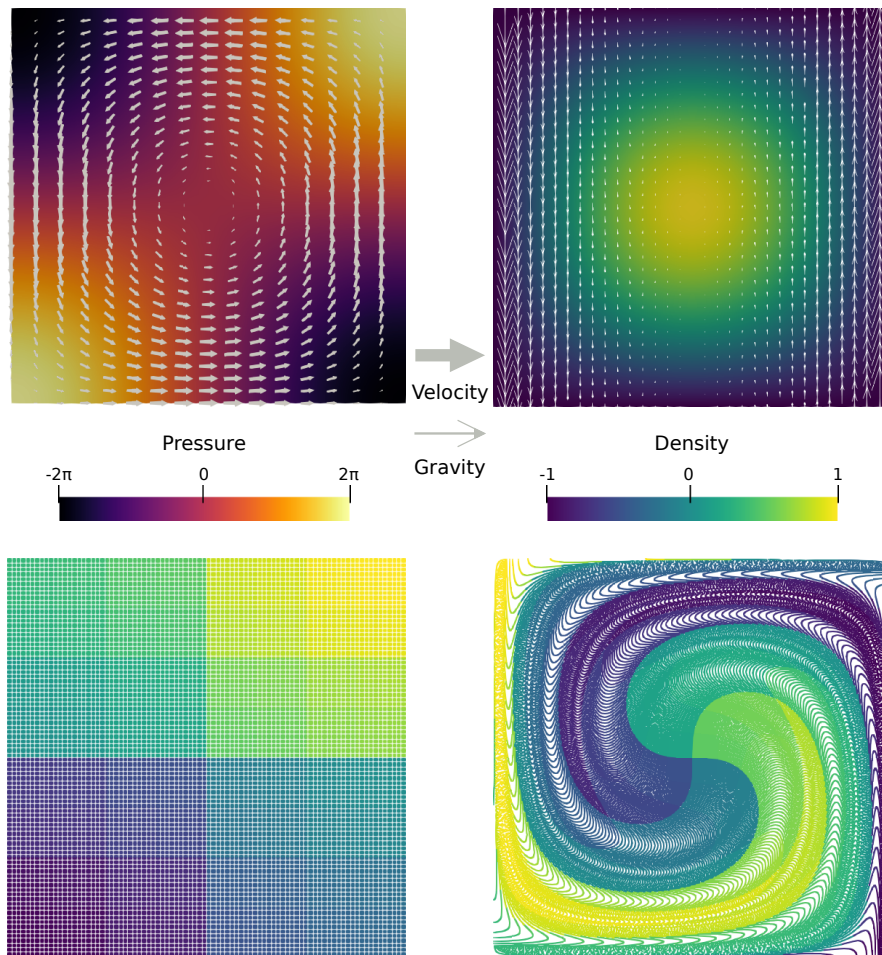


**Figure A2.** Solution of the rigid shear benchmark. Top left: The velocity and pressure solution of the benchmark. Top right: Density and gravity fields that determine the right hand side of the Stokes system. Bottom row: Initial ( $t = 0$ ) and final particle distributions after one full revolution of the center ( $t = 2$ ), colored by particle index.

$p(x, y)$ , the density  $\rho(x, y)$ , and the gravity vector  $\mathbf{g} = (g_x, g_y)$  to satisfy the governing equations. Since there are two equations to satisfy ( $x$  and  $y$  component of (B.1)), but four functions to choose, we can choose two of these functions arbitrarily. As for the spherical case, because we want the benchmark to be stationary, we choose a density  $\rho(x, y)$  that is constant along streamlines, and for convenience we choose  $\rho(x, y) = \pi\psi(x, y) = \sin(\pi x) \sin(\pi y)$ . Additionally, we arbitrarily set  $g_x = 0$ . Substituting all of these expressions into (A.1) then yields

$$2\pi^2 \sin(\pi x) \cos(\pi y) + \frac{\partial p}{\partial x} = 0, \quad (\text{B.5})$$

$$-2\pi^2 \cos(\pi x) \sin(\pi y) + \frac{\partial p}{\partial y} = \rho g_y, \quad (\text{B.6})$$

and integrating (B.5) for  $x$  gives us the pressure:

$$p(x, y) = 2\pi \cos(\pi x) \cos(\pi y) + c. \quad (\text{B.7})$$

Similarly, differentiating (B.7) and substituting in (B.6) results in the  $y$ -component of gravity:

$$g_y = -4\pi^2 \frac{\cos(\pi x)}{\sin(\pi x)}. \quad (\text{B.8})$$

In summary, our constructed solution is as follows:

$$\mathbf{u} = \begin{bmatrix} \sin(\pi x) \cos(\pi y) \\ -\cos(\pi x) \sin(\pi y) \end{bmatrix}, \quad (\text{B.9})$$

$$p = 2\pi \cos(\pi x) \cos(\pi y), \quad (\text{B.10})$$

$$\rho = \sin(\pi x) \sin(\pi y), \quad (\text{B.11})$$

$$\mathbf{g} = \begin{bmatrix} 0 \\ -4\pi^2 \frac{\cos(\pi x)}{\sin(\pi x)} \end{bmatrix}. \quad (\text{B.12})$$

## APPENDIX C: RESULTS OF THE TIME DEPENDENT BOX BENCHMARK

Figure A3 and Figure A4 present results for this second time-dependent benchmark, using an identical layout as for the spherical annulus case. Despite the changed geometry and different model solution, all measured convergence rates are consistent with the model of Section 5.1.

46 *R. Gassmöller, H. Lokavarapu, W. Bangerth, E. G. Puckett*

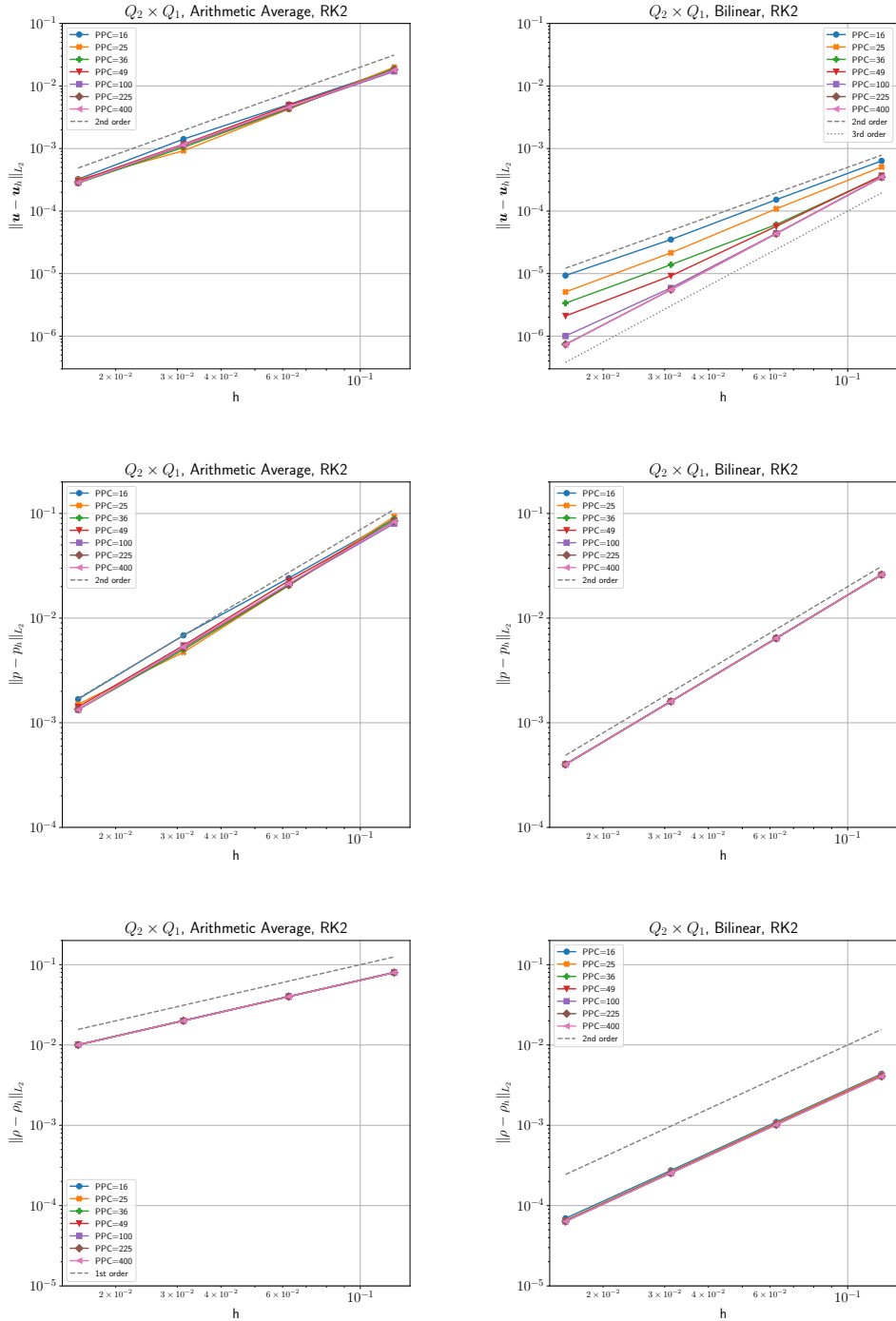


**Figure A3.** The convergence rate of  $\|u - u_h\|_{L_2}$  (top),  $\|p - p_h\|_{L_2}$  (middle), and  $\|\rho - \rho_h\|_{L_2}$  (bottom) measured at  $t = 0.1$  for the time dependent box benchmark. Density is carried on particles and is interpolated as cell-wise arithmetic average ( $r = 1$ , left) and bilinear least-squares interpolation ( $r = 2$ , right). All models use a  $Q_2 \times Q_1$  element ( $k = 2$ ) and RK2 to advect particles. Note that only with bilinear least-squares interpolation and an increasing number of particles per cell ( $PPC$ ) is the third order convergence rate of velocity recovered. In all cases,  $\|p - p_h\|_{L_2}$  converges at second-order rate with no apparent influence due to the number of  $PPC$  (i.e., all dots fall on each other), while the convergence rate of  $\|\rho - \rho_h\|_{L_2}$  depends on the interpolation scheme, but not on  $PPC$ .

## Evaluating hybrid finite element mesh/particle-in-cell methods 47

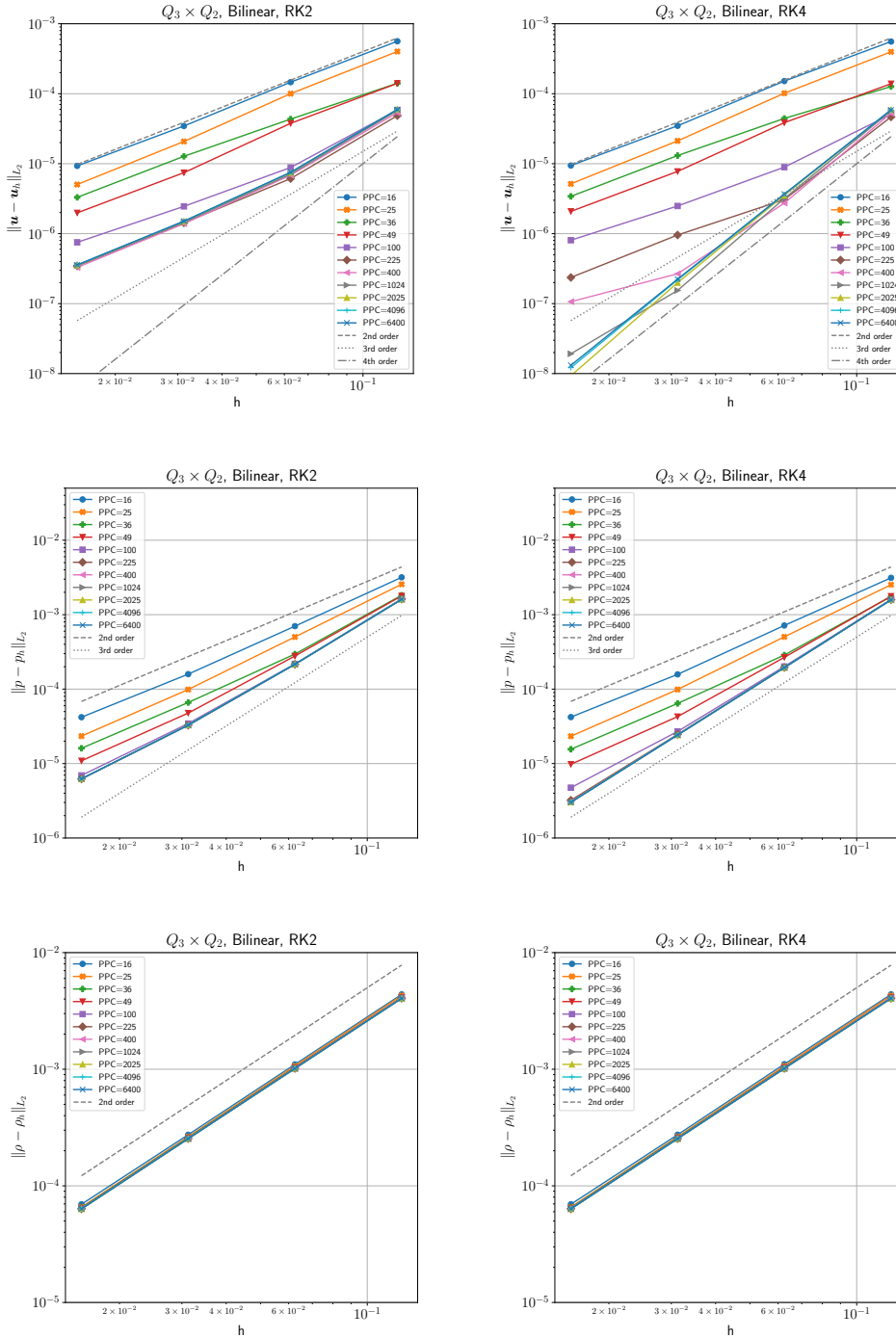


**Figure A4.** Panels as in Fig. A3, but for a  $Q_3 \times Q_2$  element ( $k = 3$ ). All models use the bilinear least squares interpolation ( $r = 2$ ). Columns represent RK2 (left) and RK4 (right) particle integration. Note that only with RK4, bilinear least-squares interpolation and an increasing number of particles per cell ( $PPC$ ) is the fourth order convergence rate of the velocity recovered. All properties with a design convergence rate higher than 2 require an increasing  $PPC$  to reach their design rate, while constant  $PPC$  only allows for second order convergence. The density is limited to second-order accuracy due to the chosen interpolation scheme ( $r = 2$ ).



1  
2  
3 submitted to *Geophys. J. Int.*  
4  
5  
6  
7

8  
9 **Evaluating the Accuracy of Hybrid Finite**  
10  
11 **Element/Particle-In-Cell Methods for Modeling**  
12  
13 **Incompressible Stokes Flow**  
14  
15  
16  
17  
18

19 Rene Gassmöller<sup>1,\*</sup>  
20

21 Harsha Lokavarapu<sup>1</sup>  
22  
23

24 Wolfgang Bangerth<sup>2</sup>  
25  
26  
27

28 Elbridge Gerry Puckett<sup>3</sup>  
29

30 <sup>1</sup> *Department of Earth and Planetary Science, U. C. Davis, Davis, CA 95616, USA.*

31 <sup>2</sup> *Department of Mathematics, Colorado State University, Fort Collins, CO 80523, USA.*

32 <sup>3</sup> *Department of Mathematics, U. C. Davis, Davis, CA 95616, USA.*

33 \* *Corresponding author.*  
34  
35  
36  
37  
38  
39

40 **SUMMARY**

41 Combining finite element methods for the incompressible Stokes equations with  
42 particle-in-cell methods is an important technique in computational geodynam-  
43 ics that has been widely applied in mantle convection, lithosphere dynamics, and  
44 crustal-scale modeling. In these applications, particles are used to transport along  
45 properties of the medium such as the temperature, chemical compositions, or other  
46 material properties; the particle methods are therefore used to reduce the advection  
47 equation to an ordinary differential equation for each particle, resulting in a problem  
48 that is simpler to solve than the original equation for which stabilization techniques  
49 are necessary to avoid oscillations.  
50  
51  
52  
53  
54  
55  
56  
57  
58

59 On the other hand, replacing field-based descriptions by quantities only defined at  
60

1  
2  
3  
4 2 *R. Gassmüller, H. Lokavarapu, W. Bangerth, E. G. Puckett*

5 the locations of particles introduces numerical errors. These errors have previously  
6 been investigated, but a complete understanding from both the theoretical and prac-  
7 tical sides was so far lacking. In addition, we are not aware of systematic guidance  
8 regarding the question of how many particles one needs to choose per mesh cell to  
9 achieve a certain accuracy.  
10

11 In this paper we modify two existing instantaneous benchmarks and present a new  
12 analytic benchmark for time-dependent incompressible Stokes flow in order to com-  
13 pare the convergence rate and accuracy of various combinations of finite element,  
14 particle advection, and particle interpolation methods. Using these benchmarks, we  
15 find that in order to retain the optimal accuracy of the finite element formulation,  
16 one needs to use a sufficiently accurate particle interpolation algorithm. Addition-  
17 ally, we observe and explain that for [our](#) higher-order finite-element methods it is  
18 necessary to increase the number of particles per cell as the mesh resolution increases  
19 (i.e., as the grid cell size decreases) to avoid a reduction in convergence order.  
20  
21

22 Our methods and results allow designing new particle-in-cell methods with specific  
23 convergence rates, and also provide guidance for the choice of common building  
24 blocks and parameters such as the number of particles per cell. In addition, our new  
25 time-dependent benchmark provides a simple test that can be used to compare dif-  
26 ferent implementations, algorithms, and for the assessment of new numerical meth-  
27 ods for particle interpolation and advection. We provide a reference implementation  
28 of this benchmark in ASPECT (the “Advanced Solver for Problems in Earth’s  
29 ConvecTion”), an open source code for geodynamic modeling.  
30  
31

32 **Key words:** Numerical approximations and analysis, Numerical solutions, Numer-  
33 ical modelling, Dynamics of lithosphere and mantle, Mantle processes  
34  
35  
36  
37  
38  
39  
40  
41  
42  
43  
44  
45  
46  
47

## 48 1 INTRODUCTION

49 Computational geodynamic models are important tools to understand the dynamic processes  
50 observed in the solid Earth; for example, to model mantle convection, lithosphere dynam-  
51 ics, and crustal deformation. Most of these models involve solving the Stokes equations with  
52  
53  
54  
55  
56  
57  
58  
59  
60

*Evaluating hybrid finite element mesh/particle-in-cell methods* 3

variable rock properties (such as viscosity and density) for the velocity and pressure. These equations are then coupled to the time evolution of an advection-diffusion equation for the temperature, and, more generally, the advection of additional quantities that influence rock properties, such as chemical composition [McNamara & Zhong(2005), Tackley(1998), Dannberg & Gassmüller(2018)], grain size [Rozel et al.(2011), Thielmann et al.(2015), Dannberg et al.(2017), Mulyukova & Bercovici(2018)], or melt fraction and depletion [Fischer & Gerya(2016), Gassmüller et al.(2016)].

Consequently, a number of different techniques, with various advantages and disadvantages, have been developed to solve advection or advection-diffusion equations. Among these are techniques that directly solve the advection equations using stabilized finite element or finite difference methods [Brooks & Hughes(1982), Guermond & Pasquetti(2011), Kronbichler et al.(2012)], volume-of-fluid methods [Hirt & Nichols(1981)], but notably also ones in which “particles” are used to describe the motion of the material with its associated properties. Among these latter methods are particle-in-cell or marker-and-cell methods [Evans et al.(1957), Harlow & Welch(1965)], and interface tracking methods such as marker-chain [Poliakov & Podladchikov(2003)]. For a recent comparison see [Puckett et al.(2017)].

Particle-in-cell (PIC) methods in particular have been widely used for geodynamic computations [Poliakov & Podladchikov(1992), Tackley & King(2003), Moresi et al.(2003), Gerya & Yuen(2003), McNamara & Zhong(2004), Tackley & King(2003), Moresi et al.(2003), Gerya & Yuen(2003), McNamara & Zhong(2004), Popov & Sobolev(2008)], since they are conceptually simple and do not require specialized algorithms or other techniques to stabilize the solution of the strongly advection-dominated equation. In PIC or related methods, the advected property is transported on a set of discrete particles that are advected with the flow. Since each particle’s movement is independent of all of the other particles, this converts the partial differential equation for the advection of the quantity or quantities carried by the particles into a set of ordinary differential equations for each particle’s location and, possibly, the evolution of the quantity. When the particles’ properties are required for the solution of the Stokes equations for the next time step, they are interpolated or projected back onto the discrete grid. After the Stokes solve, the locations and properties of the particles are updated, e.g. by interpolating the newly computed solution or an appropriately determined update back onto the particles.

Despite the long history of researchers using PIC methods in geodynamic codes, many challenges continue to exist in the implementation and application of these methods. Among these are that PIC methods are difficult to combine with adaptively refined and dynamically changing meshes, since the number of particles per cell may vary widely during a computation

1  
2  
3  
4 4 *R. Gassmöller, H. Lokavarapu, W. Bangerth, E. G. Puckett*

5 and the numerical error and convergence properties of the method are difficult to determine  
6 precisely (see also [Gassmöller et al.(2018)]). At a more fundamental level, we are not aware  
7 of a systematic study that considers the different contributions to the overall numerical error  
8 in a PIC scheme. The excellent paper by Thielmann, May, and Kaus [Thielmann et al.(2014)]  
9 provides many answers in this regard, but leaves open others that relate, in particular, to the  
10 question of what convergence orders one can expect in time-dependent Stokes flow, and when  
11 appropriately varying the number of particles per cell. A separate recent study by Samuel  
12 (see [Samuel(2018)]) is concerned with improvements of the PIC method for time-dependent  
13 shear flow and reducing the required number of particles, but does not quantify the influence  
14 of the accumulated particle error on the Stokes solution. We therefore consider the current  
15 study an extension of [Thielmann et al.(2014)] in which we provide both a theoretical analysis  
16 and numerical evidence that support each other, and complementary to [Samuel(2018)] in  
17 that we investigate the particle error contributions on time-dependent flow.  
18  
19  
20  
21  
22  
23  
24  
25  
26

27 Specifically, we quantitatively determine the accuracy of particle-in-cell methods cou-  
28 pled to finite element-based Stokes solvers in order to untangle the influence of the following  
29 building blocks of PIC methods on the accuracy of the solution: (1) the number and dis-  
30 tribution of particles, (2) the interpolation of particle-based properties to field-based prop-  
31 erties, and (3) the integration of the motion of the particles over time. In order to achieve  
32 this we start by reproducing the instantaneous benchmark results SolCx and SolKz [Duretz  
33 et al.(2011), Zhong(1996)], and discuss how the convergence rate of the computed solution  
34 depends on different finite element and interpolation algorithm combinations. Our numeri-  
35 cal results generally reproduce our theoretical predictions and demonstrate that in order to  
36 recover the intrinsic convergence rate of a given finite element, we need both a sufficiently  
37 accurate particle interpolation algorithm and sufficiently many particles per cell. Crucially,  
38 however, we also show that for the chosen algorithms the number of particles per cell needs  
39 to grow with the mesh resolution in order to retain the optimal convergence order for higher  
40 order elements, leading to a method in which the cost of particle advection grows faster than  
41 the cost of the mesh-based computations if higher accuracy is required.  
42  
43  
44  
45  
46  
47  
48  
49  
50  
51

52 We then extend these considerations to the time-dependent case by developing a new  
53 benchmark, and using it to evaluate the coupled finite element/PIC scheme. All of our re-  
54 sults are implemented in the open-source geodynamic modeling code ASPECT [Kronbichler  
55 et al.(2012), Heister et al.(2017)]. It is our intention that these results will act as reference  
56 results for future code comparison studies of time-independent or time-dependent PIC advec-  
57  
58  
59  
60

*Evaluating hybrid finite element mesh/particle-in-cell methods* 5

tion algorithms, and will allow researchers to design PIC methods that use a combination of techniques to ensure optimal accuracy of the numerical method as a whole.

This paper continues as follows: In Section 2, we present the continuous model we wish to solve. Section 3 then describes in detail how we compute numerical approximations to the solution of the model, and we end the section with a theoretical analysis of error contributions and the convergence orders one can predict using this analysis. Section 4 then uses stationary benchmarks to confirm that the theoretical analysis indeed correctly describes what one sees in practical computations. Section 5 extends these results to time-dependent problems: we first present a new, *time-dependent* benchmark (the derivation of which may be found in Appendix A) with an analytical solution. This benchmark then allows us to evaluate the error and convergence rates for time-dependent computations of incompressible Stokes flow coupled to a PIC advection method. We conclude in Section 6.

## 2 GOVERNING EQUATIONS

Geologic deformation over long time scales is commonly modeled by the incompressible Stokes equations for a slow-moving fluid, using a spatially and temporally variable viscosity that depends nonlinearly on both the strain rate and pressure of the fluid, as well as temperature, chemical composition, and possibly other factors. The driving force for the flow is provided by a buoyancy term that results from the spatial variability of the density, again due to temperature, pressure, and chemical composition differences.

The incompressible Stokes equations that describe this type of flow are given by a force balance and a mass continuity equation:

$$-\nabla \cdot (2\eta \varepsilon(\mathbf{u})) + \nabla p = \rho \mathbf{g}, \quad (1)$$

$$\nabla \cdot \mathbf{u} = 0, \quad (2)$$

where  $\mathbf{u}$  is the velocity,  $p$  the pressure,  $\rho$  the density,  $\eta$  the viscosity, and  $\mathbf{g}$  the gravity. Furthermore,  $\varepsilon(\mathbf{u}) = \frac{1}{2}(\nabla \mathbf{u} + \nabla \mathbf{u}^T)$  is the symmetric gradient of the velocity and denotes the strain rate within the fluid.

In more realistic applications, the mass continuity equation (2) has to be replaced by an equation that allows for compressible effects. However, as this is tangential to the purpose of the current paper, we will simply assume that the fluid is incompressible. In either case, the equations above are augmented by appropriate boundary conditions.

A complete description of mantle convection would couple the equations above to a set of advection-diffusion equations for the temperature and chemical compositions, as well as

6 *R. Gassmüller, H. Lokavarapu, W. Bangerth, E. G. Puckett*

possibly other relevant quantities such as grain size distributions, frozen stress tensors, etc., all of which are transported along with the velocity  $\mathbf{u}$  (see [Schubert et al.(2001)]). If we denote (the components of) these fields by  $\phi_c = \phi_c(\mathbf{x}, t)$ ,  $c = 1, \dots, C$ , then each such  $\phi_c$  typically satisfies an advection-diffusion equation of the form

$$\frac{D\phi_c}{Dt} - \nabla \cdot (\kappa_c \nabla \phi_c) = \frac{\partial \phi_c}{\partial t} + \mathbf{u} \cdot \nabla \phi_c - \nabla \cdot (\kappa_c \nabla \phi_c) = H_c, \quad (3)$$

augmented by appropriate initial conditions  $\phi_c(\mathbf{x}, 0) = \phi_{c,0}(\mathbf{x})$  and, if necessary, boundary conditions.  $H_c$  is a source term that in general depends both on the flow variables as well as some or all of the other  $\phi_{c'}$ . For example, if  $\phi_c$  denotes the temperature, then the source term might include contributions due to friction heating and adiabatic compression, while if  $\phi_c$  represents a particular material type's volume fraction, it might increase its value at the cost of that of other materials.

The importance of these additional fields lies in the fact that in realistic descriptions of convection in the Earth, the viscosity  $\eta$  and density  $\rho$  in the Stokes equations above not only depend on strain rate  $\varepsilon(\mathbf{u})$  and pressure  $p$ , but also on these additional variables  $\phi_c$ . Consequently, the resulting set of equations is coupled, nonlinear, and time dependent. An accurate solution of the complete model therefore requires an accurate way of advecting along these additional quantities.

In typical applications the equation is dominated by the advection term  $\mathbf{u} \cdot \nabla \phi_c$ , and the contributions by the diffusion term  $-\nabla \cdot (\kappa_c \nabla \phi_c)$  are rather small (if  $\phi_c$  denotes the temperature) or are completely negligible (for example if  $\phi_c$  denotes a chemical composition). In this paper, we are concerned with solving these equations for quantities for which the diffusion term can be neglected; in this case, the equation above simplifies to

$$\frac{D\phi_c}{Dt} = \frac{\partial \phi_c}{\partial t} + \mathbf{u} \cdot \nabla \phi_c = H_{c\underline{.}}. \quad (4)$$

Consequently, this paper is devoted to solving the coupled set of Stokes and advection equations, (1)–(2) and (4), accurately. In particular, we will consider approximating the solution of (4) using particle methods and how these methods affect the accuracy of solving (1)–(2) using field-based finite element methods when the two approaches are coupled.

In the following sections, we will not make use of the fact that we may, in fact, have more than one additional property. As a consequence, we will drop the index  $c$  on the quantities  $\phi_c$ . However, everything we will say below remains true for cases with multiple such properties.

### 3 NUMERICAL METHODOLOGY

Equations (1)–(2) and (4) can be solved by direct discretization via finite element, finite volume, or finite difference methods, or a variety of other methods (see, for example [Donea & Huerta(2003), Deubelbeiss & Kaus(2008), Gerya(2009), Ismail-Zadeh & Tackley(2010)]).

However, discretizing advection problems such as (4) without introducing oscillations or excessive diffusion is not trivial. As discussed above, many mantle convection codes have instead used particle schemes to advect along properties of rocks. In these schemes, a number of particles  $k = 1 \dots N$  are characterized by their location  $\mathbf{x}_k(t)$  and associated properties  $\phi_k(t)$ . Their location and value then evolves according to the ordinary differential equation

$$\frac{d}{dt}\mathbf{x}_k(t) = \mathbf{u}(\mathbf{x}_k(t), t), \quad \mathbf{x}_k(0) = \mathbf{x}_{k,0}, \quad (5)$$

$$\frac{d}{dt}\phi_k(t) = H, \quad \phi_k(0) = \phi_{k,0}, \quad (6)$$

where  $H$  is a function of both particle-based quantities  $[\mathbf{x}_k(t), \phi_k(t)]$ , field-based quantities  $[\mathbf{u}(\mathbf{x}_k(t), t), \varepsilon(\mathbf{u}(\mathbf{x}_k(t), t)), p(\mathbf{x}_k(t), t)]$ , and possibly other variables such as the time  $t$ . Conversely, coefficients in the Stokes system (1)–(2) such as the viscosity  $\eta$  and density  $\rho$  at arbitrary points  $\mathbf{x}$  (e.g., at quadrature points) may depend not only on field quantities such as velocity and pressure at  $\mathbf{x}$ , but also on the quantities  $\phi_k$  of particles located “close” to  $\mathbf{x}$ .

While conceptually simple to implement, this approach requires (i) transferring data from field-based quantities to particle locations when evaluating the right hand sides of (5) and (6) at  $\mathbf{x}_k$ , (ii) integrating particle locations and properties in time according to (5) and (6), and finally (iii) transferring data back from particle locations to quadrature points when evaluating coefficients of (1)–(2) at arbitrary locations  $\mathbf{x}$  during assembly of matrices and right hand sides for the Stokes equation.

All of these three steps introduce errors into the solution process: In the first step, the exact solution  $\mathbf{u}(t)$  is not available, and one has to use numerical approximations  $\mathbf{u}_h(t^n)$  that were found by approximating the solution of the Stokes equations at discrete times  $t^n$ . This error therefore depends on the accuracy of the spatial discretization used for the computed velocity field, and of the time-stepping scheme. In the second step, the numerical integration of (5) yields a trajectory  $\mathbf{x}_h(t)$  that is different from  $\mathbf{x}(t)$  even if the velocity were known exactly, depending on the accuracy of the ODE solver scheme; likewise, we obtain an approximation  $\phi_{h,k}(t)$  different from the exact solution  $\phi_k(t)$  of (6). Finally, no particle will typically be located on a quadrature point  $\mathbf{x}$  at time  $t$ , and the required property  $\phi(\mathbf{x}, t)$  will need to be interpolated in one of many possible, approximate ways from the properties  $\phi_k(t)$  of nearby particles.

8 *R. Gassmüller, H. Lokavarapu, W. Bangerth, E. G. Puckett*

We will assess these errors quantitatively in Section 4 and Section 5 in a number of benchmarks, for different Stokes discretizations, different initial particle locations, ODE solvers, and particle interpolation methods, all of which we will describe in remainder of this section.

### 3.1 Discretization of the Stokes system

The advection of particles can only be as accurate as the underlying velocity field that is used to advect them. In this work, the velocity is obtained by using finite elements to discretize and solve the Stokes equations. Specifically, we will employ the common  $Q_k \times Q_{k-1}$  “Taylor-Hood” element [Taylor & Hood(1973)] in which the velocity and pressure are discretized by continuous finite elements of degrees  $k$  and  $k - 1$  on quadrilaterals or hexahedra, respectively. For comparison to the existing results of [Thielmann et al.(2014)], we will also use  $Q_k \times P_{-(k-1)}$  elements in which the pressure is discretized using discontinuous polynomials of (total) degree  $k - 1$ . Based on finite-element theory we expect both the  $Q_k \times Q_{k-1}$  and the  $Q_k \times P_{-(k-1)}$  elements to show optimal convergence order [Bercovier & Pironneau(1979)]; i.e., to show a decay of the velocity and pressure errors, when measured in the  $L_2$  norm, as  $h^{k+1}$  and  $h^k$ , respectively, where  $h$  is the element size of the mesh. We show in Section 4 and 5 that this is indeed the case for our implementation and model setups. In all of our experiments we assume that the Stokes equation is solved either with a direct solver, or with a sufficiently tight tolerance on an iterative solver, so that the only remaining error stems from the spatial discretization of the flow field intrinsic to the used finite-element.

### 3.2 Generation of particles

In time dependent problems, particles are transported along with the flow; after some time, they will no longer be at specific locations. Therefore, algorithms that reconstruct coefficients from particles’ properties need to be general and deal with both arbitrary particle numbers and locations on each cell. However, the test cases we will consider in Section 4, will only solve a single time step without advecting particles. Thus, the particles are located where they were created, and we need to make sure not to rely on a ~~particular-specific~~ particle distribution that controls our results.

We will consider two strategies for choosing the initial particle locations  $\mathbf{x}_k(0) = \mathbf{x}_{k,0}$ :

(i) Create a number of particles  $N_K$  on a regular grid of points within the cell  $\hat{K}$  in the reference domain, from where they are mapped to the corresponding points on each cell  $K$  of the triangulation.



*Evaluating hybrid finite element mesh/particle-in-cell methods* 9

(ii) Create a number of particles  $N_K$  within each cell  $K$ , with locations drawn from a uniform probability distribution on  $K$ ; here,  $N_K$  is equal to the fraction of the volume occupied by cell  $K$  relative to the volume of the global domain  $\Omega$ , times the global number of particles  $N$ .

The practical implementation of both algorithms in arbitrary geometries is described in [Gassmüller et al.(2018)]. Note, that approach (i) will lead to a constant particle count per cell, while approach (ii) will lead to a roughly constant particle density per area.

Choosing between the two strategies allows us to determine the influence of different particle distributions on the accuracy of the solution. As we will see, for our benchmarks models with uniform mesh resolution these differences are in fact pretty small, although they would become important for adaptive meshes, and after a finite amount of shear. Furthermore, for the time-dependent benchmark cases in Section 5, initial particle locations are less critical as particles are moving from their starting positions; for simplicity easier reproducibility, we therefore always generate particles at regular grid locations (approach (i)) in the time dependent cases.

### 3.3 Advection of particles

As described above, the advection of particles involves solving (5) for their position, which we do using a Runge-Kutta method of second (RK2) or fourth order (RK4). As expected and as shown for our implementation before (see supporting information of [Gassmüller et al.(2018)]) the error of particle positions for a given static flow field reduces as  $\Delta t^2$  and  $\Delta t^4$  for RK2 and RK4 respectively. However, because we will use a second order accurate BDF2 time-stepping scheme for our Stokes solution, any particle advection method is limited for a time-varying velocity field to be second order accurate in time. Since the exact solution of the benchmark in Section 5 is time-independent, this will not be a limiting factor for our experiments. Nevertheless, this limitation has to be considered for realistic applications. We also note that our discrete velocity solutions are only divergence-free in an integral sense, and evaluating the velocity at the particle locations introduces a spurious velocity divergence that can lead to the clustering of particles in certain flow patterns. This phenomenon can be improved using velocity corrections known as conservative velocity interpolation ~~[Wang et al.(2015), Pusok et al.(2017)]~~ [Meyer & Jenny(2004), Wang et al.(2015), Pusok et al.(2017)]. However, even perfectly known and divergence free velocities can form shear patterns that lead to particle clustering; this can be addressed with appropriate particle weighting, splitting, and merging schemes [Samuel(2018)]. We did not employ such methods in our benchmarks, as we ~~did not observe this clustering~~ limited

10 *R. Gassmöller, H. Lokavarapu, W. Bangerth, E. G. Puckett*

11 [our benchmarks to moderate strain](#), and we were mostly concerned with the optimal conver-  
12 gence rate possible with the unmodified advection schemes. Nevertheless, it would be an in-  
13 teresting future study to quantify the influence of such velocity modifications on the accuracy  
14 of the particle advection, [while ensuring that they do not affect the convergence rate](#).

### 15 3.4 Interpolation of particle data

16 Since particles carry material properties  $\phi_k$  that enter the assembly of the linear systems used  
17 to solve for the field-based quantities, we need to define how these material properties can be  
18 evaluated at quadrature points  $\mathbf{x}$  that do not, in general, coincide with the location of any  
19 of the particles. This operation is often called “interpolation” from particle locations to the  
20 mesh, though a better term may in fact be “projection”; we will use the terms interchangeably.  
21 In particular, let  $K$  be a cell,  $I_K \subseteq [1, N]$  be the set of ~~indices of those particles~~ [those particle](#)  
22 [indices \(among the overall  \$N\$  particles\)](#) that are located on  $K$ , and  $N_K = |I_K|$  be their number.  
23 Then we consider the following two strategies to evaluate property  $\phi$  at an arbitrary location  
24  $\mathbf{x}$  based on the information  $\{\phi_k\}_{k \in I_K}$  that is available on  $K$  alone:

25 (i) Piecewise constant averages: To obtain  $\phi(\mathbf{x})$  on cell  $K$ , we average the material proper-  
26 ties among all particles located on  $K$ :

$$27 \phi|_K = \frac{1}{N_K} \sum_{k \in I_K} \phi_k. \quad (7)$$

28 The value  $\phi(\mathbf{x})$  is then computed by finding the cell  $K$  within which  $\mathbf{x}$  is located, and taking  
29 the local average on  $K$ . In theory one could use different averaging schemes than arithmetic  
30 averaging, for example harmonic or geometric averaging. However, since it was shown be-  
31 fore that these schemes converge with the same order (though varying absolute accuracy)  
32 to the correct solution [Thielmann et al.(2014)] (see also the related discussion in [Heister  
33 et al.(2017)]), here we limit ourselves to arithmetic averaging.

34 (ii) Least squares (bi-/tri-)linear interpolation: In this algorithm, we seek a function  $\phi$  that  
35 is (bi-/tri-)linear on each cell  $K$ . We will allow it to be discontinuous between cells, and in  
36 that case it can be computed locally on each cell independently. Specifically, we seek  $\phi|_K$  so  
37 that it minimizes the squared error,

$$38 \epsilon^2 = \sum_{k \in I_K} [\phi|_K(\mathbf{x}_k) - \phi_k]^2, \quad (8)$$

39 where  $\mathbf{x}_k$  is the location of particle  $k$  with associated property  $\phi_k$ .

40 The minimizer  $\phi|_K$  is found by solving a  $4 \times 4$  matrix in 2 dimensions, or an  $8 \times 8$  matrix  
41 in three dimensions, for the coefficients of the (bi-/tri-)linear least-squares approximation.

1  
2  
3  
4  
5  
6  
7  
8  
9  
10  
11  
12  
13  
14  
15  
16  
17  
18  
19  
20  
21  
22  
23  
24  
25  
26  
27  
28  
29  
30  
31  
32  
33  
34  
35  
36  
37  
38  
39  
40  
41  
42  
43  
44  
45  
46  
47  
48  
49  
50  
51  
52  
53  
54  
55  
56  
57  
58  
59  
60

To obtain material property values at an arbitrary  $\mathbf{x}$  in  $K$  then only requires evaluating  $\phi|_K(\mathbf{x})$ , i.e., evaluating the (bi-/tri-)linear shape functions of the approximand times their corresponding coefficient values. As observed before [Thielmann et al.(2014)] this algorithm generates over-/undershooting close to strong property gradients, which need to be handled in some form, for example by a strict limiter for the interpolated property. However, all of the benchmark results we show below are either sufficiently smooth or have property gradients aligned with the mesh, therefore we did not need to apply the limiter here. Note that in contrast to [Thielmann et al.(2014)] we include the mixed polynomial terms  $xy$  (and, in three space dimensions,  $xz$ ,  $yz$ ,  $xyz$ ) in the interpolation function to stay consistent with the polynomial space of our pressure element. This modification potentially explains why our method performs better for lower number of particles per cell, as discussed in Section 4.1.

### 3.5 An error analysis

In this section, let us provide some theoretical considerations for how the particle-based scheme outlined above might affect the overall error in the finite element solution of the Stokes problem. Our goal here is to derive error convergence orders for the  $L_2$  norm errors in velocity and pressure, i.e., for

$$\|\mathbf{u} - \mathbf{u}_h\|_{L_2} = \left( \int |\mathbf{u}(\mathbf{x}, t) - \mathbf{u}_h(\mathbf{x}, t)|^2 dx \right)^{1/2}, \quad (9)$$

$$\|p - p_h\|_{L_2} = \left( \int |p(\mathbf{x}, t) - p_h(\mathbf{x}, t)|^2 dx \right)^{1/2}. \quad (10)$$

We will test the statements we will derive in computational experiments in the sections to follow.

Before stating concrete error inequalities, let us present the conceptual framework in which these are presented. In particular, in Section 4 we will consider the numerical approximation of the solution of a stationary Stokes problem (1)–(2) using the finite element method in which we do not know the exact density  $\rho$  and viscosity  $\eta$ , but only have this information available at the locations of particles. (In Section 5, where we consider time dependent benchmarks, we will in fact only know the exact density and viscosity at points  $\mathbf{x}_k$  whose coordinates are only approximately known; we ignore this for the moment.) This can be stated as follows: In the numerical problem that we will solve using the finite element method, we will use a density  $\rho_h = I_h R_h \rho$  and viscosity  $\eta_h = I_h R_h \eta$ , where the operator  $R_h f$  restricts the values of a function  $f$  to the locations of particles, and the operator  $I_h$  interpolates the values of a function defined only at particle locations to the entire domain so that it can be evaluated

12 *R. Gassmöller, H. Lokavarapu, W. Bangerth, E. G. Puckett*

at arbitrary quadrature points for use in the finite element method;  $I_h$  can be one of the two options discussed in the previous subsection. The question is how the replacement of  $\rho, \eta$  by  $\rho_h, \eta_h$  affects the accuracy with which we can compute numerical approximations  $\mathbf{u}_h, p_h$  via the finite element method.

Let us then concisely define what problem we solve. In particular, let  $\mathcal{L}_\eta$  be the solution operator of the Stokes equations (1)–(2), i.e., for a given right hand side  $\rho\mathbf{g}$  and viscosity  $\eta$ , we have that  $\{\mathbf{u}, p\} = \mathcal{L}_\eta(\rho\mathbf{g})$  solves the Stokes equations. Furthermore, let  $\mathcal{L}_\eta^h$  be the *discrete* solution operator, i.e.,  $\{\mathbf{u}_h, p_h\} = \mathcal{L}_\eta^h(\rho\mathbf{g})$  is the finite element solution of these equations. The question we want to answer is how the exact solution  $\mathcal{L}_\eta(\rho\mathbf{g})$  relates to the finite element approximation  $\mathcal{L}_{\eta_h}^h(\rho_h\mathbf{g})$  in which we have replaced density and viscosity as discussed above. Specifically, we will measure this error in the “energy norm”:

$$\|\mathcal{L}_\eta(\rho\mathbf{g}) - \mathcal{L}_{\eta_h}^h(\rho_h\mathbf{g})\|^2 = \eta_0 \|\nabla(\mathbf{u} - \mathbf{u}_h)\|_{L_2}^2 + \|p - p_h\|_{L_2}^2, \quad (11)$$

where  $\eta_0$  is a suitably chosen reference viscosity that ensures that the two terms are appropriately balanced and have matching physical units. We will later relate this norm to the  $L_2$  norms of both the velocity and pressure errors (instead of the  $H^1$  seminorm of the velocity and the  $L_2$  norm of the pressure).

To answer the question about the size of the error, let us first consider the following auxiliary problem: It is well known that replacing a sufficiently smooth function  $\rho$  or  $\eta$  by a suitable (i) piecewise constant or (ii) piecewise (bi-/tri-)linear approximation on a mesh of maximal mesh size  $h$  incurs an error proportional to  $h$  and  $h^2$ , respectively, when measuring the error in the  $L_2$  norm. In other words, if we denote these approximants by  $P_h\rho$  and  $P_h\eta$ , then

$$\begin{aligned} \|\rho - P_h\rho\|_{L_2} &= \mathcal{O}(h^r), \\ \|\eta - P_h\eta\|_{L_2} &= \mathcal{O}(h^r), \end{aligned} \quad (12)$$

where  $r = 1$  for approximation option (i) and  $r = 2$  for option (ii) of the previous subsection. Concisely, we define  $P_h$  locally on each cell  $K$  as follows, when applied to an arbitrary function  $f$ :

$$\begin{aligned} \text{option (i): } P_h f|_K &= \frac{1}{|K|} \int_K f \\ \text{option (ii): } P_h f|_K &= \arg \min_{\varphi_h \in Q_1(K)} \frac{1}{2} \|f - \varphi_h\|_{L_2(K)}^2 \end{aligned} \quad (13)$$

Note that  $P_h$  is equal to  $I_h R_h$  if one were to consider infinitely many particles equally distributed on each cell  $K$  because then the points-based least-squares approximations (7) and (8) agree with the integral-based least-squares approximations in (13). Below, we will also

need estimates such as (12) in other norms, and consequently state the following results:

$$\begin{aligned}\|f - P_h f\|_{H^1} &= \mathcal{O}(h^{r-1}), \\ \|f - P_h f\|_{H^{-1}} &= \mathcal{O}(h^{r+1}),\end{aligned}\tag{14}$$

where the first denotes the error in the gradient of  $f$ .

Using this argument, we can now decompose the overall error into four components. Namely, we will write the error as follows:

$$(\eta_0 \|\nabla(\mathbf{u} - \mathbf{u}_h)\|_{L_2}^2 + \|p - p_h\|_{L_2}^2)^{1/2}\tag{15}$$

$$= \|\mathcal{L}_\eta(\rho \mathbf{g}) - \mathcal{L}_{\eta_h}^h(\rho_h \mathbf{g})\|\tag{16}$$

$$\leq \underbrace{\|\mathcal{L}_\eta(\rho \mathbf{g}) - \mathcal{L}_\eta(P_h \rho \mathbf{g})\|}_{(1)}\tag{17}$$

$$+ \underbrace{\|\mathcal{L}_\eta(P_h \rho \mathbf{g}) - \mathcal{L}_{P_h \eta}(P_h \rho \mathbf{g})\|}_{(2)}\tag{18}$$

$$+ \underbrace{\|\mathcal{L}_{P_h \eta}(P_h \rho \mathbf{g}) - \mathcal{L}_{\eta_h}(\rho_h \mathbf{g})\|}_{(3)}\tag{19}$$

$$+ \underbrace{\|\mathcal{L}_{\eta_h}(\rho_h \mathbf{g}) - \mathcal{L}_{\eta_h}^h(\rho_h \mathbf{g})\|}_{(4)}.\tag{20}$$

Here, the four norm terms on the right correspond, respectively, to (1) the error introduced by replacing  $\rho$  by the projection  $P_h \rho$  when solving the continuous Stokes equations, (2) the error introduced by replacing  $\eta$  by the projection  $P_h \eta$  when solving the continuous Stokes equations, (3) the error introduced by further substituting  $P_h \rho, P_h \eta$  by  $\rho_h = I_h R_h \rho, \eta_h = I_h R_h \eta$  when solving the continuous Stokes equations, and (4) the error introduced by the finite element solution instead of the exact solution of two problems with the same coefficients. Let us determine the size of these terms individually, in increasing order of difficulty.

For the discretization error, (4), it is well known that when using either  $Q_k \times Q_{k-1}$  or  $Q_k \times P_{-(k-1)}$  finite elements, we have

$$\|\mathcal{L}_{\eta_h}(\rho_h \mathbf{g}) - \mathcal{L}_{\eta_h}^h(\rho_h \mathbf{g})\| = \mathcal{O}(h^k),\tag{21}$$

where  $h$  is the diameter of the largest cell of the mesh. It is worth mentioning that this statement is only correct if the solution is sufficiently smooth (for example,  $\mathbf{u} \in H^{k+1}$  and  $p \in H^k$ ).

The replacement error for the density (1) is also easy. To this end, one needs to know that

1  
2  
3  
4 14 *R. Gassmöller, H. Lokavarapu, W. Bangerth, E. G. Puckett*

5 the Stokes operator is linear and stable in the  $H^{-1}$  norm, i.e., that

$$6 \quad \|\mathcal{L}_\eta f_1 - \mathcal{L}_\eta f_2\| = \|\mathcal{L}_\eta(f_1 - f_2)\| \leq C \|f_1 - f_2\|_{H^{-1}}. \quad (22)$$

7  
8 with some constant  $C < \infty$ . Since  $f_1 = \rho$  and  $f_2 = P_h \rho$ , we can use (14) to obtain that the  
9 first error term satisfies

$$10 \quad \|\mathcal{L}_\eta(\rho \mathbf{g}) - \mathcal{L}_\eta(P_h \rho \mathbf{g})\| = \mathcal{O}(h^{r+1}). \quad (23)$$

11  
12 The replacement error for the viscosity, (2), is more difficult to analyze. However, it is  
13 reasonable to assume that the solutions of two Stokes equations with viscosities  $\eta_1, \eta_2$  differ  
14 by an amount proportional to  $\|\eta_1 - \eta_2\|_{L_2}$ . This would here suggest, invoking (12), that

$$15 \quad \|\mathcal{L}_{P_h \eta}(P_h \rho \mathbf{g}) - \mathcal{L}_\eta(P_h \rho \mathbf{g})\| \leq D \|\eta - P_h \eta\|_{L_2} = \mathcal{O}(h^r), \quad (24)$$

16 again with some constant  $D$ . We have no proof of this statement, though it seems reason-  
17 able using standard arguments in the analysis of elliptic PDEs (see, for example, [Gilbarg &  
18 Trudinger(1983)]). (The use of the  $L_2$  norm – or maybe the  $L_\infty$  norm, for which one obtains  
19 the same estimate – seems natural when analyzing PDE solutions this way. One might be  
20 tempted to ask whether one could replace  $\|\eta - P_h \eta\|_{L_2}$  by  $\|\eta - P_h \eta\|_{H^{-1}}$  and thereby gain an  
21 order of convergence. But it will turn out, based on our numerical examples, that the estimate  
22 is indeed correct as stated regarding the order of convergence. †)

23  
24 This leaves the error (3) due to replacing the projections  $P_h \rho, P_h \eta$  by the interpolants  
25  $\rho_h = I_h R_h \rho, \eta_h = I_h R_h \eta$ . Similar arguments as for the errors (1) and (2) yield that

$$26 \quad \begin{aligned} & \|\mathcal{L}_{P_h \eta}(P_h \rho \mathbf{g}) - \mathcal{L}_{\eta_h}(\rho_h \mathbf{g})\| \\ & \leq C \|P_h \rho - I_h R_h \rho\|_{H^{-1}} + D \|P_h \eta - I_h R_h \eta\|_{L_2}. \end{aligned}$$

$$27 \quad \begin{aligned} & \|\mathcal{L}_{P_h \eta}(P_h \rho \mathbf{g}) - \mathcal{L}_{\eta_h}(\rho_h \mathbf{g})\| \\ & \leq C \|P_h \rho - I_h R_h \rho\|_{H^{-1}} + D \|P_h \eta - I_h R_h \eta\|_{L_2}. \end{aligned} \quad (25)$$

28  
29 The exact size of these terms depends on how many particle locations we have on each cell,  
30 as well as how they are located. All we know is that if we increase the number of points, and  
31 if these points are uniformly distributed, then  $I_h R_h \rightarrow P_h$  and consequently the entire error  
32 term goes to zero. For finite numbers of particles per cell (*PPC*), we will simply denote the  
33 right hand side as  $E(h, PPC)$  with the expectation that asymptotically  $E(h, PPC) \rightarrow 0$  as  
34  $PPC \rightarrow \infty$  or  $h \rightarrow 0$ .

35 Taking all of this together then yields that we should expect the following error behavior

in the energy norm of the Stokes problem:

$$\begin{aligned} & \underline{\underline{(\eta_0 \|\nabla(\mathbf{u} - \mathbf{u}_h)\|_{L_2}^2 + \|p - p_h\|_{L_2}^2)^{1/2}}} \\ & \underline{\underline{= \mathcal{O}(h^{r+1}) + \mathcal{O}(h^r) + \mathcal{O}(E(h, PPC)) + \mathcal{O}(h^k)}}. \end{aligned} \quad (26)$$

This immediately yields the desired behavior of the pressure error in the  $L_2$  norm:

$$\|p - p_h\|_{L_2} = \mathcal{O}(h^{r+1}) + \mathcal{O}(h^r) + \mathcal{O}(E(h, PPC)) + \mathcal{O}(h^k). \quad (27)$$

The velocity error in the  $L_2$  norm requires marginally more work. Using the standard Nitsche trick [Brenner & Scott(2007)] to obtain the  $L_2$  error from the  $H^1$  error provides us with an extra power of  $h$  and then yields

$$\begin{aligned} \|\mathbf{u} - \mathbf{u}_h\|_{L_2} &= \mathcal{O}(h^{r+2}) + \mathcal{O}(h^{r+1}) \\ &+ \mathcal{O}(h E(h, PPC)) + \mathcal{O}(h^{k+1}). \end{aligned} \quad (28)$$

The next section of this paper is in essence an exploration of these last two relationships using concrete testcases.

#### 4 INSTANTANEOUS BENCHMARKS

The first set of benchmarks we will consider only solves a single time step; thus, the positions of particles are known *exactly*. The benchmarks are therefore intended to test the influence of initial particle distributions, Stokes discretizations, and the transfer of information from particles to field-based quantities.

Specifically, we will consider the SolKz and SolCx benchmarks [Revenaugh & Parsons(1987), Zhong(1996)] that have previously been used to test the accuracy of Stokes solvers in the presence of a spatially variable viscosity [Duretz et al.(2011), Kronbichler et al.(2012)]. For both benchmarks, an exact solution for the velocity and pressure fields is available. We can then compare the convergence order we obtain if (i) we use the exact density and viscosity when assembling the finite element linear system for the Stokes system, or (ii) we use viscosity and density values that are interpolated from a set of nearby particles that have each been initialized using the exact values at their respective location. In the first of these cases, only

1  
2  
3  
4 16 *R. Gassmöller, H. Lokavarapu, W. Bangerth, E. G. Puckett*

5 contribution (4) of the errors considered in Section 3.5 is present, whereas in the second case,  
6 all four contributions matter.  
7

8 As we will show, and as anticipated in Section 3.5, the way we interpolate from nearby  
9 particles to quadrature points greatly matters in retaining (or not retaining) the convergence  
10 order of the finite element scheme. To assess this quantitatively, we will evaluate the difference  
11 between the known, exact solution and the computed, approximate solution in the  $L_2$  norm as  
12 defined in Section 3.5, considering both the velocity and pressure. The involved integrals are  
13 approximated through quadrature using a Gauss formula with two more quadrature points in  
14 each coordinate direction than the polynomial degree of the velocity element; this guarantees  
15 both an accurate evaluation of the integral and avoids inadvertent super-convergence effects.  
16  
17  
18  
19  
20

21 We will defer to the next section a discussion of time dependent cases where we also have  
22 to deal with the additional error introduced by inexact advection of particle locations.  
23  
24  
25

#### 26 4.1 SolKz

27  
28 The SolKz benchmark [Durez et al.(2011)] uses a smoothly varying viscosity on a 2D square  
29 domain with height and width of one. It uses tangential boundary conditions on the boundary,  
30 a vertical gravity of 1, and chooses the density field in such a way that one can construct an  
31 exact solution for the Stokes equation with the given viscosity.  
32  
33

34 Specifically, the viscosity varies with depth  $y$  as

$$35 \eta(x, y) = e^{2By}, \quad (29)$$

36  
37 where  $B$  is chosen such that the viscosity ratio between top and bottom is  $10^6$ . The density  
38 is given by  
39  
40

$$41 \rho(x, y) = -\sin(2y) \cos(3\pi x). \quad (30)$$

42  
43 We begin by investigating the influence of the initial particle locations on the convergence  
44 rate of the velocity and pressure solution for either of the two interpolation methods discussed  
45 before. We show these results in Table 1 for different mesh resolutions. The methods converge  
46 with different rates, and indeed at the rates predicted by (27) and (28). The initial particle  
47 locations do not influence the convergence rate significantly, though the absolute errors are  
48 somewhat larger for random particle locations, likely because some cells receive unfavorable  
49 particle locations (e.g., a high particle density in only a small volume of the cell). We also  
50 observe that for smaller numbers of particles per cell than the one shown here, the difference  
51 between the results obtained using regular and random particle locations is larger. This is  
52 intuitive, as for an infinite number of particles the two methods should generate similar particle  
53  
54  
55  
56  
57  
58  
59  
60



**Table 1.** Velocity errors  $\|\mathbf{u} - \mathbf{u}_h\|_{L_2}$  and pressure errors  $\|p - p_h\|_{L_2}$  for the SolKz benchmark using the  $Q_2 \times P_{-1}$  Stokes element ( $k = 2$ ), for arithmetic averaging ( $r = 1$ ) and bilinear least squares ( $r = 2$ ) interpolation methods, and for regular and random particle distributions as discussed in Section 3.2.  $PPC$  (particles per cell),  $k$ , and  $r$  are as defined in Section 3.5.

Arithmetic average ( $r = 1$ )					
$h$	$PPC$	regular		random	
		$\ \mathbf{u} - \mathbf{u}_h\ _{L_2}$	rate	$\ \mathbf{u} - \mathbf{u}_h\ _{L_2}$	rate
$\frac{1}{8}$	100	$7.05 \cdot 10^{-6}$	-	$7.08 \cdot 10^{-6}$	-
$\frac{1}{16}$	100	$1.86 \cdot 10^{-6}$	1.92	$1.95 \cdot 10^{-6}$	1.86
$\frac{1}{32}$	100	$4.81 \cdot 10^{-7}$	1.95	$4.87 \cdot 10^{-7}$	2.00
$\frac{1}{64}$	100	$1.22 \cdot 10^{-7}$	1.98	$1.29 \cdot 10^{-7}$	1.92
$\frac{1}{128}$	100	$3.05 \cdot 10^{-8}$	2.00	$2.93 \cdot 10^{-8}$	2.13
$\frac{1}{256}$	100	$7.63 \cdot 10^{-9}$	2.00	$7.91 \cdot 10^{-9}$	1.89
		$\ p - p_h\ _{L_2}$		$\ p - p_h\ _{L_2}$	
$\frac{1}{8}$	100	$1.91 \cdot 10^{-2}$	-	$1.92 \cdot 10^{-2}$	-
$\frac{1}{16}$	100	$1.24 \cdot 10^{-2}$	0.62	$1.24 \cdot 10^{-2}$	0.63
$\frac{1}{32}$	100	$6.57 \cdot 10^{-3}$	0.92	$6.60 \cdot 10^{-3}$	0.91
$\frac{1}{64}$	100	$3.33 \cdot 10^{-3}$	0.98	$3.35 \cdot 10^{-3}$	0.98
$\frac{1}{128}$	100	$1.67 \cdot 10^{-3}$	1.00	$1.68 \cdot 10^{-3}$	1.00
$\frac{1}{256}$	100	$8.37 \cdot 10^{-4}$	1.00	$8.40 \cdot 10^{-4}$	1.00
Bilinear least squares ( $r = 2$ )					
$h$	$PPC$	regular		random	
		$\ \mathbf{u} - \mathbf{u}_h\ _{L_2}$	rate	$\ \mathbf{u} - \mathbf{u}_h\ _{L_2}$	rate
$\frac{1}{8}$	100	$1.72 \cdot 10^{-6}$	-	$1.68 \cdot 10^{-6}$	-
$\frac{1}{16}$	100	$2.46 \cdot 10^{-7}$	2.81	$2.49 \cdot 10^{-7}$	2.75
$\frac{1}{32}$	100	$3.50 \cdot 10^{-8}$	2.81	$3.52 \cdot 10^{-8}$	2.82
$\frac{1}{64}$	100	$4.56 \cdot 10^{-9}$	2.94	$4.71 \cdot 10^{-9}$	2.90
$\frac{1}{128}$	100	$5.95 \cdot 10^{-10}$	2.94	$6.55 \cdot 10^{-10}$	2.85
$\frac{1}{256}$	100	$8.41 \cdot 10^{-11}$	2.82	$1.05 \cdot 10^{-10}$	2.64
		$\ p - p_h\ _{L_2}$		$\ p - p_h\ _{L_2}$	
$\frac{1}{8}$	100	$4.53 \cdot 10^{-3}$	-	$4.72 \cdot 10^{-3}$	-
$\frac{1}{16}$	100	$1.30 \cdot 10^{-3}$	1.80	$1.33 \cdot 10^{-3}$	1.83
$\frac{1}{32}$	100	$3.42 \cdot 10^{-4}$	1.93	$3.49 \cdot 10^{-4}$	1.93
$\frac{1}{64}$	100	$8.67 \cdot 10^{-5}$	1.98	$8.84 \cdot 10^{-5}$	1.98
$\frac{1}{128}$	100	$2.17 \cdot 10^{-5}$	2.00	$2.22 \cdot 10^{-5}$	1.99
$\frac{1}{256}$	100	$5.43 \cdot 10^{-6}$	2.00	$5.54 \cdot 10^{-6}$	2.00

locations, namely particles in every possible location, while for few particles all of them could be randomly generated in a very small part of the cell, leaving a large region unsampled. Having established that the choice of initial particle locations does not influence the achieved

18 *R. Gassmöller, H. Lokavarapu, W. Bangerth, E. G. Puckett*

**Table 2.** Velocity errors  $\|\mathbf{u} - \mathbf{u}_h\|_{L_2}$  and pressure errors  $\|p - p_h\|_{L_2}$  for the SolKz benchmark using the  $Q_2 \times P_{-1}$  (top rows), and  $Q_3 \times Q_2$  (bottom rows) Stokes elements. *PPC* (particles per cell),  $k$ , and  $r$  are as defined in Section 3.5.

$Q_2 \times P_{-1}$ ( $k = 2$ )									
$\ \mathbf{u} - \mathbf{u}_h\ _{L_2}$	direct method ( $r = \infty$ )		arithmetic average ( $r = 1$ )			bilinear least squares ( $r = 2$ )			
	$h$	error	rate	<i>PPC</i>	error	rate	<i>PPC</i>	error	rate
$\frac{1}{8}$	$1.51 \cdot 10^{-6}$	-	4	$6.32 \cdot 10^{-6}$	-	4	$2.24 \cdot 10^{-6}$	-	
$\frac{1}{16}$	$2.50 \cdot 10^{-7}$	2.60	4	$1.61 \cdot 10^{-6}$	1.97	4	$3.61 \cdot 10^{-7}$	2.63	
$\frac{1}{32}$	$3.52 \cdot 10^{-8}$	2.80	4	$4.15 \cdot 10^{-7}$	1.96	9	$4.62 \cdot 10^{-8}$	2.97	
$\frac{1}{64}$	$4.53 \cdot 10^{-9}$	3.00	4	$1.05 \cdot 10^{-7}$	1.98	25	$5.3 \cdot 10^{-9}$	3.12	
$\frac{1}{128}$	$5.7 \cdot 10^{-10}$	3.00	4	$2.63 \cdot 10^{-8}$	2.00	49	$6.75 \cdot 10^{-10}$	2.97	
$\frac{1}{256}$	$7.23 \cdot 10^{-11}$	3.00	4	$6.58 \cdot 10^{-9}$	2.00	100	$8.41 \cdot 10^{-11}$	3.00	
$\frac{1}{512}$	$9.14 \cdot 10^{-12}$	3.00	4	$1.64 \cdot 10^{-10}$	2.00	196	$1.05 \cdot 10^{-11}$	3.00	
$\ p - p_h\ _{L_2}$									
$\frac{1}{8}$	$5.02 \cdot 10^{-3}$	-	4	$1.93 \cdot 10^{-2}$	-	4	$4.58 \cdot 10^{-3}$	-	
$\frac{1}{16}$	$1.33 \cdot 10^{-3}$	1.90	4	$1.24 \cdot 10^{-2}$	0.64	4	$1.31 \cdot 10^{-3}$	1.80	
$\frac{1}{32}$	$3.44 \cdot 10^{-4}$	2.00	4	$6.58 \cdot 10^{-3}$	0.92	9	$3.43 \cdot 10^{-4}$	1.94	
$\frac{1}{64}$	$8.68 \cdot 10^{-5}$	2.00	4	$3.33 \cdot 10^{-3}$	0.98	25	$8.67 \cdot 10^{-5}$	1.98	
$\frac{1}{128}$	$2.17 \cdot 10^{-5}$	2.00	4	$1.67 \cdot 10^{-3}$	1.00	49	$2.17 \cdot 10^{-5}$	2.00	
$\frac{1}{256}$	$5.43 \cdot 10^{-6}$	2.00	4	$8.37 \cdot 10^{-4}$	1.00	100	$5.43 \cdot 10^{-6}$	2.00	
$\frac{1}{512}$	$1.36 \cdot 10^{-6}$	2.00	4	$4.19 \cdot 10^{-4}$	1.00	196	$1.36 \cdot 10^{-6}$	2.00	
$Q_3 \times Q_2$ ( $k = 3$ )									
$\ \mathbf{u} - \mathbf{u}_h\ _{L_2}$	direct method ( $r = \infty$ )		arithmetic average ( $r = 1$ )			bilinear least squares ( $r = 2$ )			
	$h$	error	rate	<i>PPC</i>	error	rate	<i>PPC</i>	error	rate
$\frac{1}{8}$	$3.1 \cdot 10^{-7}$	-	4	$5.78 \cdot 10^{-6}$	-	9	$1.26 \cdot 10^{-6}$	-	
$\frac{1}{16}$	$2.48 \cdot 10^{-8}$	3.64	4	$1.36 \cdot 10^{-6}$	2.08	9	$1.64 \cdot 10^{-7}$	2.94	
$\frac{1}{32}$	$1.59 \cdot 10^{-9}$	3.96	4	$3.34 \cdot 10^{-7}$	2.03	16	$2.09 \cdot 10^{-8}$	2.97	
$\frac{1}{64}$	$9.9 \cdot 10^{-11}$	4.00	4	$8.27 \cdot 10^{-8}$	2.01	36	$2.27 \cdot 10^{-9}$	3.20	
$\frac{1}{128}$	$6.23 \cdot 10^{-12}$	3.99	4	$2.06 \cdot 10^{-8}$	2.01	81	$2.52 \cdot 10^{-10}$	3.17	
$\frac{1}{256}$			4	$5.13 \cdot 10^{-9}$	2.00	169	$3.01 \cdot 10^{-11}$	3.07	
$\frac{1}{512}$			4	$1.28 \cdot 10^{-9}$	2.00	361	$3.66 \cdot 10^{-12}$	3.04	
$\ p - p_h\ _{L_2}$									
$\frac{1}{8}$	$7.04 \cdot 10^{-4}$	-	4	$1.86 \cdot 10^{-2}$	-	9	$1.37 \cdot 10^{-3}$	-	
$\frac{1}{16}$	$1.15 \cdot 10^{-4}$	2.61	4	$8.27 \cdot 10^{-3}$	1.17	9	$1.18 \cdot 10^{-3}$	0.21	
$\frac{1}{32}$	$1.68 \cdot 10^{-5}$	2.78	4	$3.06 \cdot 10^{-3}$	1.43	16	$3.52 \cdot 10^{-4}$	1.74	
$\frac{1}{64}$	$2.3 \cdot 10^{-6}$	2.89	4	$1.11 \cdot 10^{-3}$	1.47	36	$9.19 \cdot 10^{-5}$	1.94	
$\frac{1}{128}$	$3.03 \cdot 10^{-7}$	2.92	4	$3.99 \cdot 10^{-4}$	1.48	81	$2.32 \cdot 10^{-5}$	1.98	
$\frac{1}{256}$	$3.89 \cdot 10^{-8}$	2.96	4	$1.43 \cdot 10^{-4}$	1.48	169	$5.83 \cdot 10^{-6}$	2.00	
$\frac{1}{512}$	$4.94 \cdot 10^{-9}$	2.98	4	$5.07 \cdot 10^{-5}$	1.49	361	$1.46 \cdot 10^{-6}$	2.00	

*Evaluating hybrid finite element mesh/particle-in-cell methods* 19

convergence rate, we will conduct all other experiments with a regular particle distribution, as this delivers more ~~reproducible~~ reproducible model results.

Given that both viscosity and density in this benchmark are smooth, we expect the velocity and pressure fields to also be sufficiently smooth for a finite element method to obtain the optimal convergence order if the coefficients are evaluated exactly at each quadrature point during the assembly of linear systems. In accordance with earlier studies [Thielmann et al.(2014)] we will call this the “*direct method*”, and in the notation of Section 3.5 and Equation (12) it corresponds to  $r = \infty$  because the projection of the coefficients onto the function that is actually evaluated is the identity operation. The results of Section 3.5 then predict that, for both the  $Q_k \times Q_{k-1}$  and the  $Q_k \times P_{-(k-1)}$  elements, the velocity and pressure errors decay as  $h^{k+1}$  and  $h^k$ , respectively. Indeed, we show this experimentally in the leftmost columns of Table 2 for  $Q_2 \times P_{-1}$  (in the top rows), and for  $Q_3 \times Q_2$  (in the bottom rows). These results – as well as those in the remainder of the paper – omit data points where the error is less than approximately  $10^{-12}$ , since at that point round-off errors, ill-conditioning of the linear systems, and the finite tolerance of iterative solvers begin to dominate the overall error.

Next, we investigate the case where the viscosity and density are not obtained from an exactly prescribed function, but are instead interpolated from nearby particles. The corresponding convergence orders for the velocity and pressure errors are shown in the second and third set of columns in Table 2. For these results, we use between 4 and 361 particles per cell (*PPC*), distributed on a regular, equidistant grid. For models in which results depend on increasing *PPC* we always choose the smallest, most efficient number of particles that reaches the largest possible convergence rate.

The table then shows that a cellwise arithmetic average interpolation for the  $Q_2 \times P_{-1}$  element reduces the convergence of the velocity error to second order. We have verified that this remains so if the number of particles per cell were larger than the one used in the table. In other words using a cell-wise constant averaging is suboptimal by one order no matter how many *PPC* are used, and this also makes sense in view of the discussion in Section 3.5 that suggests that the best order that can be achieved is  $\min\{k + 1, r + 1\}$  for the velocity and  $\min\{k, r\}$  for the pressure (see equations (27) and (28)). For the element used here, we have  $k = 2$ , and cellwise constant interpolation implies  $r = 1$ , so we need to expect the observed reduction in convergence order. Using a bilinear least-squares interpolation ( $r = 2$ ) shows an interesting behavior that was briefly observed, but not fully explored before [Thielmann et al.(2014)]: At low resolutions and for a constant number of particles per cell the velocity

20 *R. Gassmöller, H. Lokavarapu, W. Bangerth, E. G. Puckett*

error decreases with nearly the expected rate of the direct method, but then degrades to second order convergence (not shown in the table, but see Figure 1 and compare also Figure 6b of [Thielmann et al.(2014)]). However, here we show that increasing the number of particles per cell approximately linearly with increasing resolution recovers the expected convergence rate of the Stokes element (last set of columns in Table 2 and Figure 1, top). This is a behavior that to our knowledge has not been described using geodynamic benchmark results before. We also note that our implementation seems to be less sensitive to the number of particles per cell since our convergence rate remains optimal to  $h = \frac{1}{512}$  for  $PPC = 256$ , while the implementation in [Thielmann et al.(2014)] degrades to second order at  $h \approx \frac{1}{128}$  for the same number of particles per cell. We speculate that this is caused by our use of a bilinear approximation, instead of a linear one, as discussed in Section 3.4. The pressure error for the  $Q_2 \times P_{-1}$  element shown in Table 2 behaves as expected, it is suboptimal by one order for the arithmetic averaging and is identical to the direct method for the bilinear least squares interpolation; both results are independent of  $PPC$  (not shown in the table). All of these results are of course consistent with the predictions of Section 3.5 if one assumes a specific relationship for  $E(h, PPC)$  as further discussed below.

Recomputing the results above for the  $Q_3 \times Q_2$  Stokes element reveals some similarities, but also noteworthy variations. For the velocity, the direct method decreases the error with the expected fourth order. The arithmetic average interpolation method again achieves second order accuracy, which for this element is sub-optimal by two orders. The bilinear least-squares interpolation results in second order convergence with constant  $PPC$  (not shown in Table 2, but shown in Figure 1, bottom), and third order convergence with increasing  $PPC$ . However, as expected it is impossible to recover the ~~expected~~ fourth order convergence rate of the direct method with increasing  $PPC$ . ~~As before;~~ this is consistent with the theoretical prediction that the velocity error converges at best with a rate of  $\min\{k+1, r+1\}$ , for  $k=3$  and  $r=2$ . As for the  $Q_2 \times P_{-1}$  element, these results are all consistent with the predictions of equations (27) and (28); the exception is that for arithmetic averaging, one would expect a first order convergence order for the pressure when in fact we observe order 1.5.

To further clarify the effect of the number of particles per cell on the convergence rate when using the bilinear interpolation scheme ( $r = 2$ ), Fig. 1 shows convergence data for the velocity error  $\|\mathbf{u} - \mathbf{u}_h\|_{L_2}$  as a function of both the mesh resolution ( $h$ ) and the number of particles per cell ( $PPC$ ). The plots show that the optimal convergence order can indeed be recovered for the  $Q_2 \times P_{-1}$  – but not the  $Q_3 \times Q_2$  – element, if one uses sufficiently many particles per cell. For both elements, the velocity error is well described by

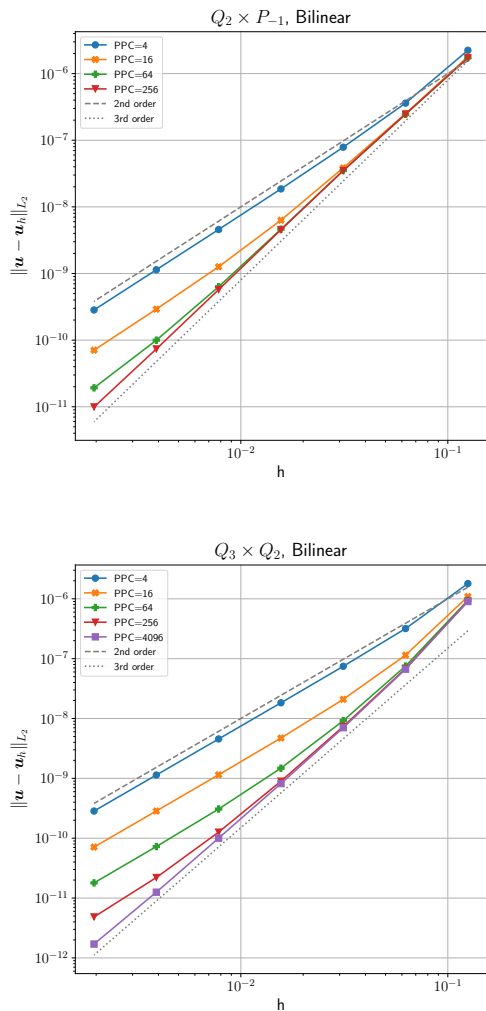


**Figure 1.** Velocity errors  $\|\mathbf{u} - \mathbf{u}_h\|_{L_2}$  for the SolKz benchmark for the  $Q_2 \times P_{-1}$  element ( $k = 2$ , top) and for the  $Q_3 \times Q_2$  element ( $k = 3$ , bottom), using bilinear interpolation ( $r = 2$ ). The error is plotted as a function of both mesh resolution ( $h$ ) and number of particles per cell ( $PPC$ ).

the approximation  $\|\mathbf{u} - \mathbf{u}_h\|_{L_2} = \mathcal{O}(h^3) + \mathcal{O}(h^2 PPC^{-1})$ . This can be compared with (28), predicting  $\mathcal{O}(h^{\min\{k+1, r+1\}}) + \mathcal{O}(h E(h, PPC))$ , to postulate a specific form for  $E(h, PPC)$ , namely  $E(h, PPC) = h PPC^{-1}$ . For the two parts of Fig. 1, we have  $k = 2$  or  $3$  and  $r = 2$ .

Figure 1 only shows velocity errors. We do not show corresponding figures for convergence data for the pressure error because for a bilinear reconstruction, the pressure converges at a fixed rate and is essentially independent of the number of particles per cell. Increasing the number of particles therefore does not increase the accuracy of the pressure, unlike for the velocity.

As a consequence of all of these considerations, for a fixed number of particles per cell

22 *R. Gassmöller, H. Lokavarapu, W. Bangerth, E. G. Puckett*

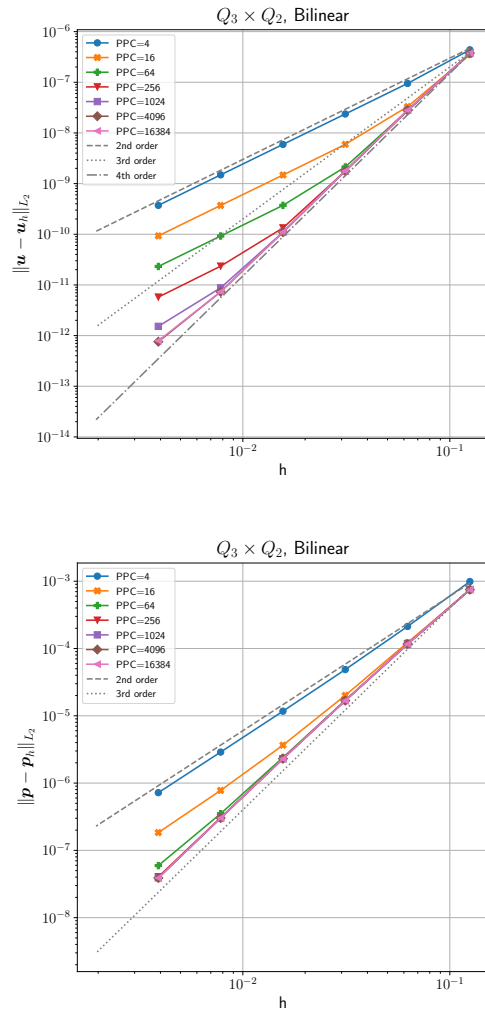


**Figure 2.** Velocity errors  $\|\mathbf{u} - \mathbf{u}_h\|_{L_2}$  (top) and pressure errors  $\|p - p_h\|_{L_2}$  (bottom) for the SolKz benchmark for the  $Q_3 \times Q_2$  element ( $k = 3$ ) and bilinear interpolation ( $r = 2$ ). The error is plotted as a function of both mesh resolution ( $h$ ) and number of particles per cell ( $PPC$ ). In contrast to Fig. 1, here we interpolate only the density from particles (that is, we use the exact viscosity in the assembly of the finite element linear system), and we recover 4th order convergence rate in velocity and 3rd order in pressure.

– i.e., the only case that can be considered scalable to large problems with fine meshes –, both elements only yield an asymptotic convergence rate of  $\|\mathbf{u} - \mathbf{u}_h\|_{L_2} = \mathcal{O}(h^2)$ . In addition, it is worth mentioning that using 196, 361, or even 4,096 particles per cell would make particle advection in time dependent problems far more expensive than solving the Stokes equation, and that using the corresponding  $14^3 = 2,744$ ,  $19^3 = 6,859$  or even  $64^3 = 262,144$  particles per cell in three space dimensions is

not a realistic option. Consequently, unless additional measures are taken, any practical use of particle methods combined with higher order finite elements will be prohibitively expensive for high mesh resolutions, or suffer from a sub-optimal convergence rate.

~~Figure 1 only shows velocity errors. We do not show corresponding figures for convergence data for the pressure error because for a bilinear reconstruction, the pressure converges at a fixed rate and is essentially independent of the number of particles per cell. Increasing the number of particles therefore does not increase the accuracy of the pressure, unlike for the velocity.~~

## 4.2 SolCx

The second instantaneous benchmark we investigate is SolCx, where the viscosity is described by

$$\eta(x, y) = \begin{cases} 1 & \text{if } x < 0.5 \\ 10^6 & \text{if } x \geq 0.5, \end{cases} \quad (31)$$

and the density by

$$\rho(x, y) = -\sin(\pi y) \cos(\pi x), \quad (32)$$

all again on the unit square  $\Omega = (0, 1)^2$ . The complete derivation of the exact solution uses a propagator matrix method and is described in [Zhong(1996)]. The defining property of this benchmark is that the discontinuous viscosity implies a nearly discontinuous pressure field and a velocity field that has a kink. Consequently, we can generally not expect optimal convergence rates unless (i) the mesh is aligned with the discontinuity and (ii) we use a pressure finite element that is discontinuous. While these properties reduce the usefulness of the benchmark for general problems, it is useful for our investigation for an unrelated reason: While the density of the benchmark problem can only be approximated with the expected accuracy of the particle interpolation methods mentioned in Section 3.4 (namely  $O(h)$  for arithmetic averaging and  $O(h^2)$  for the bilinear least squares method), the viscosity is cell-wise constant if one uses a mesh that is aligned with the interface, as we will do here. The viscosity can therefore be interpolated exactly from particles to cells independent of the interpolation method. This allows us to separate influences from density and viscosity errors on the pressure and velocity solution. Specifically, within the analysis of Section 3.5, this implies that the error contribution labeled (2) does not exist for this benchmark and that,

24 *R. Gassmüller, H. Lokavarapu, W. Bangerth, E. G. Puckett*

**Table 3.** Velocity errors  $\|\mathbf{u} - \mathbf{u}_h\|_{L_2}$  and pressure errors  $\|p - p_h\|_{L_2}$  for the SolCx benchmark using the  $Q_2 \times P_{-1}$  Stokes element (top rows), and the  $Q_3 \times Q_2$  Stokes element (bottom rows). *PPC* (particles per cell),  $k$ , and  $r$  are as defined in Section 3.5.

$Q_2 \times P_{-1} (k = 2)$								
$\ \mathbf{u} - \mathbf{u}_h\ _{L_2}$	direct method ( $r = \infty$ )		arithmetic average ( $r = 1$ )			bilinear least squares ( $r = 2$ )		
$h$	error	rate	<i>PPC</i>	error	rate	<i>PPC</i>	error	rate
$\frac{1}{8}$	$1.32 \cdot 10^{-5}$	-	4	$3.16 \cdot 10^{-5}$	-	4	$1.36 \cdot 10^{-5}$	-
$\frac{1}{16}$	$1.66 \cdot 10^{-6}$	2.99	4	$7.30 \cdot 10^{-6}$	2.12	4	$1.93 \cdot 10^{-6}$	2.81
$\frac{1}{32}$	$2.08 \cdot 10^{-7}$	3.00	4	$1.79 \cdot 10^{-6}$	2.03	9	$2.36 \cdot 10^{-7}$	3.03
$\frac{1}{64}$	$2.60 \cdot 10^{-8}$	3.00	4	$4.44 \cdot 10^{-7}$	2.01	25	$2.79 \cdot 10^{-8}$	3.08
$\frac{1}{128}$	$3.26 \cdot 10^{-9}$	3.00	4	$1.11 \cdot 10^{-7}$	2.00	49	$3.50 \cdot 10^{-9}$	3.00
$\frac{1}{256}$	$4.08 \cdot 10^{-10}$	3.00	4	$2.77 \cdot 10^{-8}$	2.00	100	$4.39 \cdot 10^{-10}$	3.00
$\frac{1}{512}$	$5.13 \cdot 10^{-11}$	3.00	4	$6.92 \cdot 10^{-9}$	2.00	196	$5.87 \cdot 10^{-11}$	2.90
$\ p - p_h\ _{L_2}$								
$\frac{1}{8}$	$1.48 \cdot 10^{-3}$	-	4	$3.16 \cdot 10^{-3}$	-	4	$1.53 \cdot 10^{-3}$	-
$\frac{1}{16}$	$3.7 \cdot 10^{-4}$	2.00	4	$8.00 \cdot 10^{-4}$	1.99	4	$3.83 \cdot 10^{-4}$	2.00
$\frac{1}{32}$	$9.22 \cdot 10^{-5}$	2.00	4	$2.00 \cdot 10^{-4}$	2.00	9	$9.29 \cdot 10^{-5}$	2.05
$\frac{1}{64}$	$2.30 \cdot 10^{-5}$	2.00	4	$5.00 \cdot 10^{-5}$	2.00	25	$2.30 \cdot 10^{-5}$	2.01
$\frac{1}{128}$	$5.75 \cdot 10^{-6}$	2.00	4	$1.25 \cdot 10^{-5}$	2.00	49	$5.75 \cdot 10^{-6}$	2.00
$\frac{1}{256}$	$1.44 \cdot 10^{-6}$	2.00	4	$3.12 \cdot 10^{-6}$	2.00	100	$1.44 \cdot 10^{-6}$	2.00
$\frac{1}{512}$	$3.59 \cdot 10^{-7}$	2.00	4	$7.80 \cdot 10^{-7}$	2.00	196	$3.59 \cdot 10^{-7}$	2.00
$Q_3 \times Q_2 (k = 3)$								
$\ \mathbf{u} - \mathbf{u}_h\ _{L_2}$	direct method ( $r = \infty$ )		arithmetic average ( $r = 1$ )			bilinear least squares ( $r = 2$ )		
$h$	error	rate	<i>PPC</i>	error	rate	<i>PPC</i>	error	rate
$\frac{1}{8}$	$6.04 \cdot 10^{-7}$	-	4	$3.15 \cdot 10^{-5}$	-	100	$9.10 \cdot 10^{-7}$	-
$\frac{1}{16}$	$4.03 \cdot 10^{-8}$	3.90	4	$7.29 \cdot 10^{-6}$	2.11	400	$5.84 \cdot 10^{-8}$	3.96
$\frac{1}{32}$	$2.60 \cdot 10^{-9}$	4.00	4	$1.79 \cdot 10^{-6}$	2.03	1600	$3.70 \cdot 10^{-9}$	3.98
$\frac{1}{64}$	$1.67 \cdot 10^{-10}$	4.00	4	$4.44 \cdot 10^{-7}$	2.01	6400	$2.34 \cdot 10^{-10}$	3.97
$\frac{1}{128}$	$1.98 \cdot 10^{-11}$	3.10	4	$1.11 \cdot 10^{-7}$	2.00	25600	$1.93 \cdot 10^{-11}$	3.60
$\frac{1}{256}$			4	$2.77 \cdot 10^{-8}$	2.00			
$\ p - p_h\ _{L_2}$								
$\frac{1}{8}$	$8.81 \cdot 10^{-3}$	-	4	$8.87 \cdot 10^{-3}$	-	100	$8.89 \cdot 10^{-3}$	-
$\frac{1}{16}$	$6.22 \cdot 10^{-3}$	0.50	4	$6.18 \cdot 10^{-3}$	0.52	400	$6.22 \cdot 10^{-3}$	0.51
$\frac{1}{32}$	$4.39 \cdot 10^{-3}$	0.50	4	$4.38 \cdot 10^{-3}$	0.50	1600	$4.39 \cdot 10^{-3}$	0.50
$\frac{1}{64}$	$3.1 \cdot 10^{-3}$	0.50	4	$3.10 \cdot 10^{-3}$	0.50	6400	$3.1 \cdot 10^{-3}$	0.50
$\frac{1}{128}$	$2.19 \cdot 10^{-3}$	0.50	4	$2.19 \cdot 10^{-3}$	0.50	25600	$2.19 \cdot 10^{-3}$	0.50
$\frac{1}{256}$			4	$1.55 \cdot 10^{-3}$	0.50			

consequently, equations (27) and (28) can be replaced by

$$\|\mathbf{u} - \mathbf{u}_h\|_{L_2} = \mathcal{O}(h^{r+2}) + \mathcal{O}(h E(h, PPC)) + \mathcal{O}(h^{k+1}), \quad (33)$$

$$\|p - p_h\|_{L_2} = \mathcal{O}(h^{r+1}) + \mathcal{O}(E(h, PPC)) + \mathcal{O}(h^k). \quad (34)$$



*Evaluating hybrid finite element mesh/particle-in-cell methods* 25

In other words, as a function of the interpolation order  $r$ , the expected convergence order is one higher than in the general case represented by the SolKz benchmark discussed in the previous subsection.

Table 3 demonstrates convergence of the velocity and pressure for the  $Q_2 \times P_{-1}$  element (top rows), and the  $Q_3 \times Q_2$  element (bottom rows).

Starting with the  $Q_2 \times P_{-1}$  element ( $k = 2$ ) and the direct method ( $r = \infty$ , left-most columns of the top half of the table), the velocity error decreases with  $O(h^3)$  and the pressure error with  $O(h^2)$  as expected and as reported previously [Kronbichler et al.(2012)], although half an order higher than reported in [Thielmann et al.(2014)]. Similarly, and as predicted by (33) and (34) above, when using particles and bilinear reconstructions ( $r = 2$ , right-most columns of the table), we obtain the same convergence rates as for the direct method. The one exception that violates our theoretical predictions is when using particles and arithmetic averaging ( $r = 1$ , middle columns) where the theory predicts third and second order convergence for velocity and pressure, respectively, but we only obtain second order for both. The table shows this for a constant number of particles per cell, suggesting that perhaps the term involving  $E(h, PPC)$  limits the convergence order; however, we have verified that even with large values of  $PPC$ , the convergence rate remains at two for the velocity. While we lack an understanding of why theory and practice do not agree here, we note that our data are consistent with previous results in [Thielmann et al.(2014)].

As described before [Kronbichler et al.(2012), Thielmann et al.(2014)], using a continuous pressure element like  $Q_3 \times Q_2$  ( $k = 3$ ) in general does not result in the optimal convergence rate for the pressure error because of the discontinuity in the pressure solution. Indeed, all methods to evaluate coefficients (independently of  $PPC$  choice) now only reach a pressure convergence rate of  ~~$\mathcal{O}(h^{1/2})$~~   $\mathcal{O}(h^{1/2})$  as shown in the bottom half of Table 3. Nevertheless, as expected for this benchmark despite the suboptimal pressure solution, the velocity error is still able to converge with the expected rates for the direct method ( $r = \infty$ , left-most columns) and the bilinear least-squares method ( $r = 2$ , right-most columns), namely  $\mathcal{O}(h^4)$ . However, in order to obtain the latter result, we now need to increase  $PPC \propto h^{-2}$ : using a constant number of particles per cell yields a suboptimal convergence order of  $\mathcal{O}(h^2)$ , whereas using  $PPC \propto h^{-1}$  results in  $\mathcal{O}(h^3)$ .

The outlier is again the velocity error when using the piecewise constant averaging ( $r = 1$ ) where one would expect third order convergence but we only observe second order.

The convergence orders predicted for the bilinear interpolation of the density – using  $PPC \propto h^{-2}$  – were one order higher than we saw for the SolKz benchmark when using

26 *R. Gassmöller, H. Lokavarapu, W. Bangerth, E. G. Puckett*

27  $PPC \propto h^{-1}$ . This conclusion followed from the fact that the viscosity interpolation for SolCx  
 28 is exact, and remains unchanged if one tried to solve the benchmark with  $PPC \propto h^{-2}$ . In  
 29 order to verify that this interpretation is in fact correct, we repeat the SolKz benchmark  
 30 with a density that is interpolated from particles, but a viscosity that is exact (i.e., using the  
 31 particles for density, but the direct method for viscosity) – see the results shown in Fig. 2.  
 32 The  $Q_2 \times P_{-1}$  element shows no difference to the computations with interpolated viscosity,  
 33 as they already reached the convergence order implied by the discretization error (not shown  
 34 in the figure). However, the  $Q_3 \times Q_2$  element now also reaches the optimal convergence order  
 35 for velocity (namely, 4) and pressure (i.e., 3). Moreover, to achieve this, we now also require  
 36  $PPC \propto h^{-2}$  for the SolKz benchmark. All of this follows from the theoretical considerations  
 37 of Section 3.5 and shows the usefulness of separating the total error into components that can  
 38 be tested individually.

39 Finally, we have run additional tests in which the mesh cells are not aligned with the  
 40 viscosity jump (by using an odd number of cells in each direction), and have confirmed  
 41 previous results that a non-aligned jump limits the convergence order to  $\mathcal{O}(h^1)$  for the velocity  
 42 and  $\mathcal{O}(h^{1/2})$  for the pressure [Kronbichler et al.(2012), Thielmann et al.(2014)]. The choice of  
 43 finite element, particle method, and number of particles per cell does not influence this result  
 44 and does not limit the convergence order any further.

45 In summary, these experiments show the importance of the choice of  $PPC$  and particle  
 46 interpolation method in practical applications, and that their optimal choices differ depending  
 47 on whether the particles only carry density, or also viscosity information, and also depend on  
 48 the continuity of the viscosity. In particular, we may need to grow the number of particles per  
 49 cell as  $O(h^{-1})$  or even  $O(h^{-2})$  to retain the convergence order of the finite element scheme  
 50 if the expected convergence order is better than  $O(h^2)$ . This requires choosing between one  
 51 of three options: (i) One needs to use a potentially very large number of particles per cell to  
 52 retain the accuracy of the Stokes discretization, in particular if high accuracy is required or the  
 53 computations are in three space dimensions. This may be prohibitively expensive, however:  
 54 for example, in the  $Q_3 \times Q_2$  solution of the SolCx case with  $h = \frac{1}{128}$  and  ~~$PPC = 25,600$~~   
 55  $PPC = 25,600$  (see Table 3), the particle operations associated with the one time step we  
 56 solve account for some 95% of the overall run time. (ii) One accepts the loss of accuracy  
 57 by using too few particles per cell, although that then calls into question the use of higher  
 58 order polynomial spaces in the Stokes discretization. (iii) One develops methods with higher  
 59 accuracy to project properties from particle locations to fields. An alternative is to use field-  
 60 based – instead of a particle-based – descriptions of the temperature, chemical composition,

or other advected quantities as discussed in [Kronbichler et al.(2012)]; in that case, the effort for the Stokes solve and the advection solve is automatically balanced.

Finally, we want to emphasize that higher-order PIC (HOPIC) schemes with a constant number of particles per cell have been successfully developed for other applications like the shallow-water equation, and the vortex formulation of the Navier-Stokes equations [Edwards & Bridson(2012)]. In other words, we do not argue that the dependence on PPC is an intrinsic property of any higher-order PIC schemes, but is rather a consequence of the algorithmic differences between our methods and those implemented in [Edwards & Bridson(2012)]. It is apparent that determining the precise differences responsible provides a useful direction for future research.

## 5 TIME DEPENDENT BENCHMARKS

The previous section presented benchmarks that assess different strategies for the transfer of information from (stationary) particle locations back to the finite element mesh, along with the error that was introduced by this operation. On the other hand, in realistic applications, particles will be advected along, and consequently the overall error will contain contributions that are due to the transfer of particle information to the mesh, but also due to the fact that we only know particle locations up to the numerical error introduced in the integration of particle trajectories, as discussed in Section 3. We will here numerically test how large this overall error is, and what effect it has on the numerical solution of the Stokes equation when feeding information back to the Stokes solver.

To this end, we derive ~~a two different~~ time-independent ~~solution solutions~~ to the Stokes equations (1)–(2), in an annulus and in a box, in which the exact density  $\rho$  is constant on streamlines. As we noted before a spatially varying viscosity would limit the convergence rate we could achieve with our interpolation methods, and might obscure the error of the particle advection method; consequently, we choose a constant viscosity. If one were to solve the Stokes equations with this setup, the solution would of course not change with time: because  $\rho$  is constant along streamlines, and because it is advected along these streamlines, it does not actually change with time. However, if the density (as part of the right hand side) is inexactly interpolated from particles in each time step, and particles are inexactly advected along with the computed velocity, then the numerical solution *will* change with time, and we can assess the accuracy of the particle-in-cell algorithm using the difference between exact (time independent) and computed (time dependent) solution. In our experiments, we will

28 *R. Gassmöller, H. Lokavarapu, W. Bangerth, E. G. Puckett*

evaluate this numerical error for different values of the (largest) grid size  $h_{\max}$  and different numbers of particles per cell (*PPC*).

Given that we use a viscosity that is constant, the same considerations apply as for the SolCx benchmark in Section 4.2. Namely, one might expect that if the time discretization error is negligible, we could obtain the same convergence rates as shown in (33)–(34):

$$\begin{aligned} \|\mathbf{u}(t) - \mathbf{u}_h(t)\|_{L_2} &= \mathcal{O}(h^{\min\{k+1, r+2\}}) + \mathcal{O}(h E(h, PPC)), \\ \|p(t) - p_h(t)\|_{L_2} &= \mathcal{O}(h^{\min\{k, r+1\}}) + \mathcal{O}(E(h, PPC)). \end{aligned} \quad (35)$$

### 5.1 A time dependent benchmark in an annulus

For the first concrete realization of the approach outlined above, we need to construct a testcase with a steady-state velocity field that depends on a spatially non-constant density that we can advect along either as a field or with particles. ~~To make the situation not too trivial, we will choose~~ We start by choosing the domain as a two-dimensional annulus with inner and outer radii  $R_1 = 1$  and  $R_2 = 2$ , respectively.

In this situation, we can express the equations and the solution in a cylindrical coordinate system in terms of the radius  $r$  and the azimuthal angle  $\theta$ . A solution of equations (1)–(2) can then be obtained by setting

$$\eta = 1, \quad \rho(r, \theta) = 48r^5, \quad \mathbf{g}(r, \theta) = \frac{r^3}{384} \mathbf{e}_r + \mathbf{e}_\theta, \quad (36)$$

where  $\mathbf{e}_r$  and  $\mathbf{e}_\theta$  are the radial and azimuthal unit vectors, respectively. Such a gravity vector is not the gradient of a gravity potential and consequently not physical, but this is of no importance here. The Stokes system can then be solved using a separation of variables approach and yields

$$\mathbf{u}(r, \theta) = 0\mathbf{e}_r - r^7\mathbf{e}_\theta, \quad p(r, \theta) = \frac{r^9}{72} - \frac{512}{72}, \quad (37)$$

for the velocity and pressure. In other words, the flow field is circular around the center with a velocity that varies with radius. Importantly, while all solution fields in question are polynomials in  $r$  and  $\theta$ , their degrees are sufficiently high so as to not be in the finite element spaces we use. The benchmark is then completely defined by prescribing  $\eta$  and  $\mathbf{g}$  as above, along with prescribed tangential velocity boundary values on the inner and outer boundaries of the annulus, and the initial distribution of  $\rho$ . Note, that while it seems unintuitive for a gravity in  $e_\theta$  direction to cause a flow in  $-e_\theta$  direction, one can think of this flow as being driven by the prescribed tangential velocity at the outer boundary, which is gradually reduced

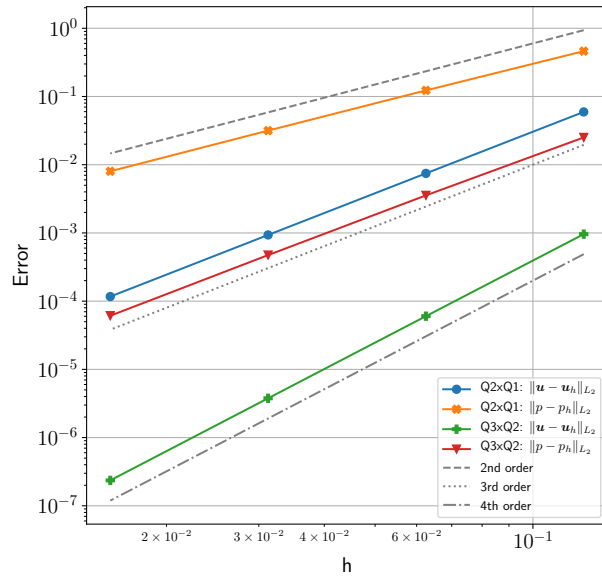


**Figure 3.** Convergence rates for the velocity  $\|\mathbf{u} - \mathbf{u}_h\|_{L_2}$  and pressure  $\|p - p_h\|_{L_2}$  for the time-dependent benchmark on the annulus using  $Q_2 \times Q_1$  and  $Q_3 \times Q_2$  element combinations, respectively. The results shown here use the exact density.

by the gravity with decreasing radius. A detailed derivation and visualization of this solution can be found in Appendix A and Fig. A1.

All experiments in this section show the error between the (stationary) exact solution  $\mathbf{u}$ ,  $p$ , and  $\rho$  and the (time-dependent) numerical approximation  $\mathbf{u}_h$ ,  $p_h$ , and  $\rho_h$  at time  $t = \frac{4\pi}{27} \approx 0.0982$ , which equals two complete revolutions of particles on the outer edge  $r = R_2$ .

## 5.2 ~~Convergence results~~ Results of the time dependent annulus benchmark

If we use the exact (and unchanging) density when computing the numerical solution of the Stokes equation, one expects convergence to the exact solution with an appropriate power of the mesh size. We verify that our solver achieves the expected convergence orders in Figure 3 for both  $Q_2 \times Q_1$  and  $Q_3 \times Q_2$  elements.

On the other hand, if the density in each time step is interpolated from particles to quadrature points, then the solution will vary from time step to time step due to the fact that particle locations are advected along with the numerical approximation of the velocity field  $\mathbf{u}$ .

Figure 4 shows convergence results for the  $Q_2 \times Q_1$  element ( $k = 2$ ) for the velocity and pressure. As was shown in the instantaneous benchmarks above (Section 4), the orders of

30 *R. Gassmüller, H. Lokavarapu, W. Bangerth, E. G. Puckett*

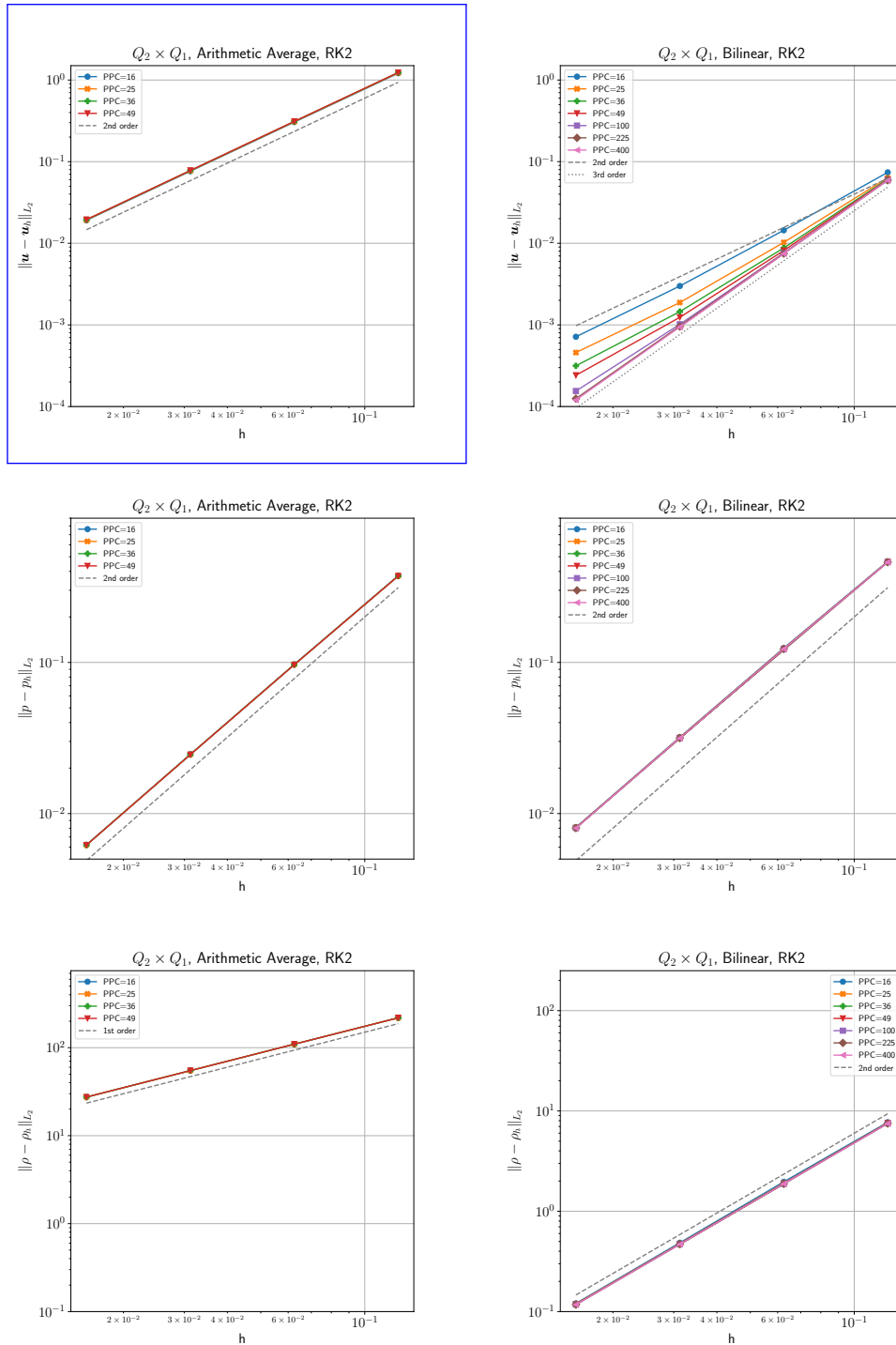


**Figure 4.** The convergence rate of  $\|u - u_h\|_{L_2}$  (top),  $\|p - p_h\|_{L_2}$  (middle), and  $\|\rho - \rho_h\|_{L_2}$  (bottom) measured at  $t = 4\pi/2^7$  for the time dependent benchmark. Density is carried on particles and is interpolated as cell-wise arithmetic average ( $r = 1$ , left) and bilinear least-squares interpolation ( $r = 2$ , right). All models use a  $Q_2 \times Q_1$  element ( $k = 2$ ) and RK2 to advect particles. Note that only with bilinear least-squares interpolation and an increasing number of particles per cell ( $PPC$ ) is the third order convergence rate of velocity recovered. In all cases,  $\|p - p_h\|_{L_2}$  converges at second-order rate with no apparent influence due to the number of  $PPC$  (i.e., all dots fall on each other), while the convergence rate of  $\|\rho - \rho_h\|_{L_2}$  depends on the interpolation scheme, but not on  $PPC$ .

convergence of the velocity and pressure error directly depend on the interpolation scheme, which also determines the convergence order for the error in density. The rates we observe in the figure exactly correspond to the predictions of (35) and (12), with one exception: For the velocity error with piecewise constant interpolation of the density (top left panel), we would have expected third order convergence ( $\min\{k + 1, r + 2\} = 3$ ) if the temporal error were negligible, whereas we only observe second order. Furthermore, this result is independent of *PPC*. We are unsure about the reasons for this, but note that it is consistent with observing the same phenomenon for the SolCx benchmark which uses a similar setup (see Section 4.2).

As expected, for the bilinear interpolation ( $r = 2$ ), the optimal convergence rate is only recovered if the number of particles per cell is increased as the mesh is refined and the number of cells increases. This observation is consistent with our instantaneous benchmarks above, and the observation in [Thielmann et al.(2014)] that the convergence rate is suboptimal for constant *PPC*. All of these results are identical for the RK2 and RK4, advection schemes, which is why we only present the RK2 results.

Figure 5 shows the corresponding results for the  $Q_3 \times Q_2$  element ( $k = 3$ ). For lack of any new information we omit the arithmetic averaging case ( $r = 1$ ) and instead compare the RK2 integration scheme to the RK4 integrator. We start by pointing out that the integration scheme (RK2 vs. RK4), the *PPC* (16 to 6400), and the finite element ( $Q_2 \times Q_1$  vs.  $Q_3 \times Q_2$ ) do not change the convergence rate of the density: it remains second-order accurate. However pressure and velocity show significant differences as predicted by (35). The only case where we obtain a lower convergence order than predicted by (35) is the velocity error when using the RK2 integrator (top left panel), which only reduces with third order where we would have expected fourth order ( $\min\{k + 1, r + 2\} = 4$ ). Interestingly, however, the expected order can be recovered by using the RK4 integrator and an increasing number of particles per cell (top right panel), suggesting that it is the temporal error that we neglected in deriving (35) that is responsible for the reduced order.

Figure 6 plots selected information from the two previous figures as velocity error over number of *PPC* for different finite elements, particle integration schemes, and mesh resolutions. In general all of the computations we made show a linear decrease of velocity error with increasing *PPC* (i.e.,  $E(h, PPC) \propto (PPC)^{-1}$  for fixed  $h$ ), which eventually transitions into a constant error at a model-specific number of *PPC* when the error sources (1), (2), and (4) of Section 3.5 begin to dominate over the error of the particle interpolation. The number of *PPC* at which the transition occurs can be interpreted as *optimal*, in the sense that it recovers the design rate of the finite element with the minimum number of particles. As can

32 *R. Gassmöller, H. Lokavarapu, W. Bangerth, E. G. Puckett*

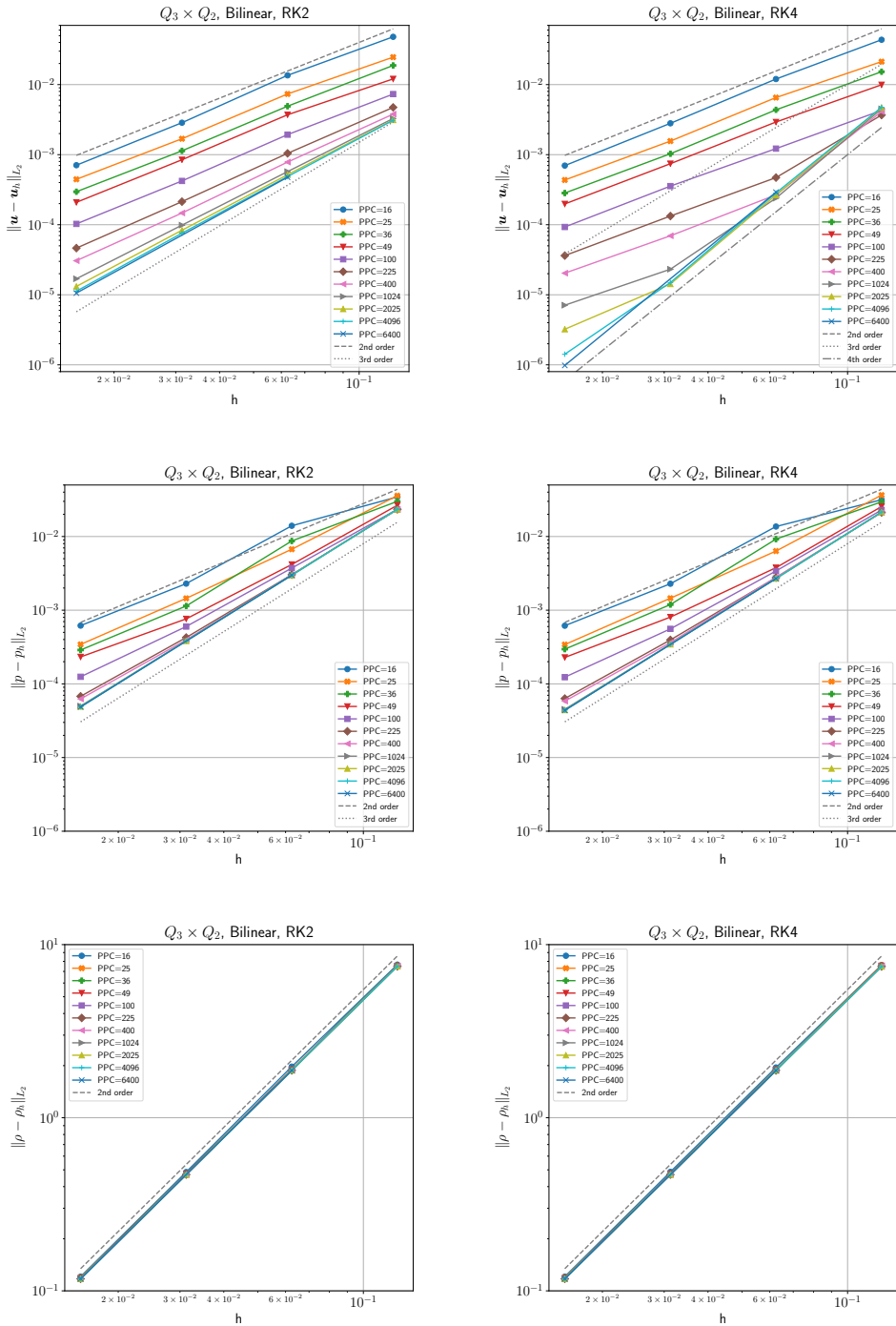


**Figure 5.** Panels as in Fig. 4, but for a  $Q_3 \times Q_2$  element ( $k = 3$ ). All models use the bilinear least squares interpolation ( $r = 2$ ). Columns represent RK2 (left) and RK4 (right) particle integration. Note that only with RK4, bilinear least-squares interpolation and an increasing number of particles per cell ( $PPC$ ) is the fourth order convergence rate of the velocity recovered. All properties with a design convergence rate higher than 2 require an increasing  $PPC$  to reach their design rate, while constant  $PPC$  only allows for second order accuracy. The density is limited to second-order accuracy due to the chosen interpolation scheme ( $r = 2$ ).



## Evaluating hybrid finite element mesh/particle-in-cell methods 33

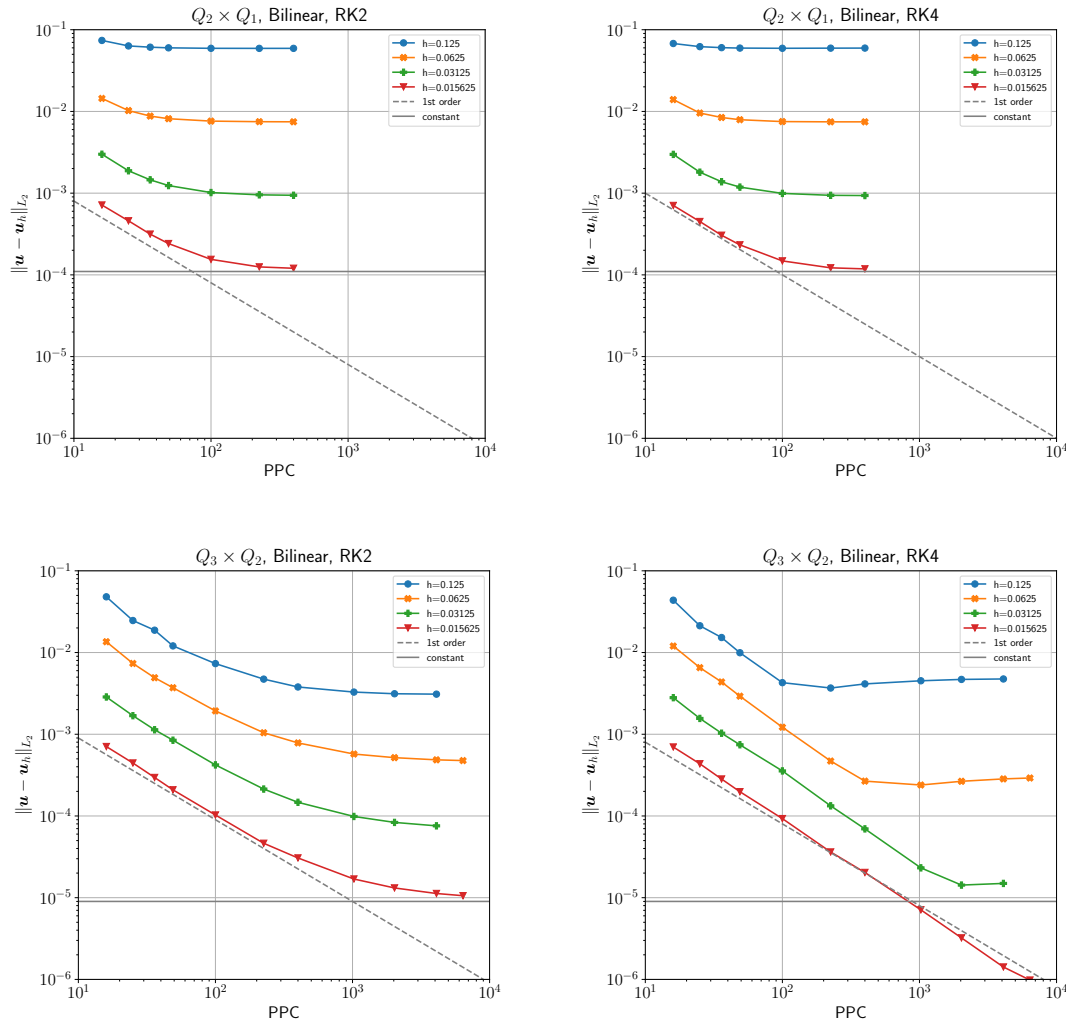


**Figure 6.** Convergence plots for velocity in the  $L_2$  norm for the time dependent annulus benchmark in dependence of the number of particles per cell ( $PPC$ ). Models were computed using a  $Q_2 \times Q_1$  finite element ( $k = 2$ , top) and  $Q_3 \times Q_2$  element ( $k = 3$ , bottom) respectively and particles were advected using a RK2 integration scheme (left) and RK4 integration scheme (right). Note that the required  $PPC$  to reach the minimum error for a given mesh refinement depends on the finite element and the mesh resolution  $h$  itself. The time integration scheme only plays a role if its convergence rate is lower than the convergence rate of the velocity element.

be seen from this figure, the optimal number of  $PPC$  is dependent on the finite element type and in the case of the  $Q_3 \times Q_2$  element also the particle integrator and in all configurations the mesh size. Most likely it will also depend on the problem one is solving. Therefore, the optimal number of  $PPC$  can not be accurately determined for practical applications except by performing a convergence series test with increasing  $PPC$  for the specific problem at the final resolution.

1  
2  
3  
4 34 *R. Gassmöller, H. Lokavarapu, W. Bangerth, E. G. Puckett*

5  
6 However, we propose that it is possible to determine a nearly optimal number of *PPC* for  
7 most problems on a coarse resolution, and then appropriately scale this number to the target  
8 resolution, considering the convergence order of the finite element ( $k$ ), the interpolation scheme  
9 ( $r$ ), and the type of properties carried on the particle (density or viscosity). To illustrate this  
10 consider the case presented in the top right panel of Figure 4, which uses the default values  
11 for  $k$  (namely, 2),  $r$  (2), and the RK2 integration scheme of our reference implementation  
12 in ASPECT. The series of models with increasing *PPC* shows that when using  $PPC = 16$ ,  
13 the error is already sufficiently close to the error when using larger numbers of *PPC* for  
14  $h = \frac{1}{8}$  to consider this number appropriate for this resolution. As determined above, the  
15 *PPC*-dependent error term discussed in Section 3.5 scales as  $E(h, PPC) = \mathcal{O}(h^2 PPC^{-1})$ ;  
16 consequently, we need to chose  $PPC \propto h^{-1}$  to achieve the expected velocity error convergence  
17 order of  $\mathcal{O}(h^3)$ . Thus, choosing  $PPC = 32$  for  $h = \frac{1}{16}$  is a natural choice, as is  $PPC = 64$  for  
18  $h = \frac{1}{32}$  (in fact we would have done so for the figure, but our particle generation algorithm  
19 requires *PPC* to be the square of a natural number, which is why we chose closeby numbers).  
20 We hypothesize that the optimal values of *PPC* that we have found in this section will be  
21 close to optimal values for a variety of smooth problems, at least for the two-dimensional  
22 cases we have considered here. Therefore, while Section 3.5 provided the maximum possible  
23 convergence order one could expect, this section provided guidance on how to choose *PPC*  
24 to actually achieve this convergence order.  
25  
26  
27  
28  
29  
30  
31  
32  
33  
34  
35

36 Concluding this section we want to emphasize that for higher-order methods and high  
37 mesh resolutions, choosing a higher *PPC* might be a more important and cheaper (though  
38 less visible) improvement in accuracy than a higher mesh resolution  $h$ . Conversely choosing a  
39 low *PPC* can result in a significant (but usually invisible) degradation of the accuracy of the  
40 solution.  
41  
42  
43  
44  
45  
46  
47  
48  
49  
50  
51  
52  
53

### 54 **5.3 A time dependent benchmark in a box**

55  
56 For the second realization of the time-dependent benchmark approach outlined above, we  
57 choose the domain as the two-dimensional unit box  $\Omega = (0, 1)^2$ .

59 For this situation, we can express the equations and the solution in a Cartesian coordinate  
60

system. A solution of equations (1)–(2) can then be obtained by setting

$$\eta = 1, \quad (38)$$

$$\rho(x, y) = \sin(\pi x) \sin(\pi y), \quad (39)$$

$$\mathbf{g}(x, y) = -4\pi^2 \frac{\cos(\pi x)}{\sin(\pi x)} \mathbf{e}_y, \quad (40)$$

where  $\mathbf{e}_y$  is the vertical unit vector (pointing upwards). While the  $y$ -component of gravity becomes singular at  $x = 0$  and  $x = 1$ , the right-hand side of (1) only contains  $\rho\mathbf{g}$  and consequently remains non-singular. We avoid accidental division by zero when assembling the equations by additionally computing  $\rho\mathbf{g}$  on the particles before interpolating the product to the grid. For consistency with the annulus benchmark we also interpolate  $\rho$  when computing the interpolation error.

The Stokes system can then be solved and yields

$$\mathbf{u}(x, y) = \begin{bmatrix} \sin(\pi x) \cos(\pi y) \\ -\cos(\pi x) \sin(\pi y) \end{bmatrix}, \quad (41)$$

$$p(x, y) = 2\pi \cos(\pi x) \cos(\pi y) \quad (42)$$

for the velocity and pressure. The resulting flow field contains rotational and shear components and is tangential to all boundaries of the box. A detailed derivation and visualization of this solution can be found in Appendix B and Fig. A2.

All experiments for this benchmark show the error between the (stationary) exact solution  $\mathbf{u}$ ,  $p$ , and  $\rho$  and the (time-dependent) numerical approximation  $\mathbf{u}_h$ ,  $p_h$ , and  $\rho_h$  at time  $t = 0.1$ , which equals  $\frac{1}{20}$  of a complete revolution of the center of the model. We did not run the benchmark for a full revolution, because as described in an earlier study [Samuel(2018)] the found flow field requires a particle rebalancing algorithm as regions of the model are sufficiently stretched to lose all particles. To avoid the complication of measuring the accuracy of particle splitting/merging algorithms we limited the model time.

The results of this benchmark setup are consistent with the results described for the annulus geometry in Section 5.2. The particle interpolation algorithm plays a crucial role in retaining the expected convergence order of the finite-element, and the particle advection scheme can limit the convergence order if its convergence order is lower than the one of the interpolation scheme. For lack of new information the corresponding figures are presented in Appendix C. This experiment shows that the interpretations of Section 5.2 are independent of model geometry.

1  
2  
3  
4 36 *R. Gassmöller, H. Lokavarapu, W. Bangerth, E. G. Puckett*

## 5 6 6 CONCLUSIONS

7  
8 In this manuscript we have used existing and developed new benchmarks to measure the  
9 accuracy and convergence rate of hybrid finite element/particle-in-cell methods and provided  
10 reference results for these benchmarks obtained with the geodynamic modeling code ASPECT.  
11 In particular, we have presented the first analytical ~~benchmark that measures benchmarks~~  
12 ~~that measure~~ the accuracy and convergence order of a time-dependent flow problem in a 2D  
13 spherical annulus ~~or a 2D unit box~~ using particles to carry material properties. Since the  
14 ~~benchmark is two benchmarks are~~ simple to derive and implement, ~~it they~~ can be used as a  
15 convenient measure for the correctness of future implementations of similar algorithms, or as  
16 a common model for code comparisons.  
17  
18  
19  
20  
21

22 Additionally, we have investigated the influence of different interpolation algorithms for  
23 ~~transferring transferring~~ information from the particles to the cells and determined that in order  
24 to retain the optimal convergence rate of high-order finite element formulations, one needs to  
25 use a sufficiently high-order particle interpolation algorithm. ~~Of course the overall convergence~~  
26 ~~rate of a model is also bounded by the application in question: models with discontinuous~~  
27 ~~material properties are limited to lower order accuracy if the mesh is not aligned with the~~  
28 ~~discontinuities.~~ This assertion is backed up by a theoretical analysis of the error contributions,  
29 predicting the observed convergence orders ~~of the presented benchmark cases~~. Among the error  
30 contributions are (i) the discretization error due to using finite element methods on meshes of  
31 finite cell size, (ii) the error introduced by replacing the exact density and viscosity functions  
32 with ones obtained by interpolating information from particles to (low-order) polynomial  
33 spaces, and (iii) the error introduced by using a finite number of particles per cell.  
34  
35  
36  
37  
38  
39  
40

41 The design of better and more accurate methods than the ones we have presented here will  
42 need to address all of these error sources. For the first of the error contributions mentioned  
43 above, this may involve the use of higher order finite element methods and/or finer meshes;  
44 both of these options are well understood and frequently used. The second error would involve  
45 interpolating data from particle locations onto polynomials of degree larger than one, for  
46 example onto quadratic polynomials ( $r = 3$ ) rather than the constant ( $r = 1$ ) or linear ones  
47 ( $r = 2$ ) used here. However, this has substantial drawbacks, for example the fact that it  
48 is often difficult to determine in practice whether a quadratic function in two or three space  
49 dimensions is strictly positive, as one would hope the density and viscosity are; more generally,  
50 the question of minimizing unwanted variability of the interpolant needs to be addressed. For  
51 the third error source, the experiments we have shown suggest that one may need to increase  
52 the number of particles per cell as one refines the mesh, and we have provided guidance on how  
53  
54  
55  
56  
57  
58  
59  
60

*Evaluating hybrid finite element mesh/particle-in-cell methods* 37

many particles per cell to choose for smooth problems to retain the intended convergence rate. Nevertheless, while the exact number of particles per cell necessary to achieve the designed convergence rate may be problem-dependent, the fact that it is resolution dependent to begin with raises the question of the scalability of the method, since either a loss of convergence rate (e.g., with a constant number of particles per cell) needs to be accepted; or the number of particles will need to increase substantially faster than the number of cells, resulting in computations in which operations on particles account for the vast majority of CPU cycles spent on a simulation. As shown by the error analysis, this error source does not disappear just because one uses a higher order interpolation scheme to transfer data from particles to the mesh. As a consequence, we are not aware of ~~an easy~~ a simple, cheap, and obvious ~~solution~~ method to reach high convergence rates using such particle-in-cell methods with higher-order finite elements, although it is quite possible that the methods we have presented yield an accuracy that is sufficient for practical ~~geodynamics~~ geodynamic simulations.

**ACKNOWLEDGMENTS**

All models were computed with the open source software ASPECT [Bangerth et al.(2018), <https://aspect.geodynamics.org>] version 2.1.0.pre (git commit hash a42335f33), ~~the time dependent box benchmark was added later in commit hash 67f2623f3~~. ASPECT is published under the GPL2 license, and the necessary data to reproduce the models is included in the software. We thank the Computational Infrastructure for Geodynamics (<https://geodynamics.org>) – which is funded by the National Science Foundation under awards EAR-0949446 and EAR-1550901 – for supporting the development of ASPECT.

W.B., R.G., H.L. and E.G.P. jointly wrote the manuscript; E.G.P., R.G. and H.L. derived the time-dependent benchmark ~~setup~~ setups; H.L. and R.G. performed the computations; R.G., E.G.P., and H.L. analyzed the benchmark results. W.B. developed the theoretical error analysis.

R. Gassmöller and W. Bangerth were partially supported by the National Science Foundation under award OCI-1148116 as part of the Software Infrastructure for Sustained Innovation (SI2) program; and by the Computational Infrastructure in Geodynamics initiative (CIG), through the National Science Foundation under Awards No. EAR-0949446, EAR-1550901 and The University of California – Davis. W. Bangerth was also supported by the National Science Foundation under Award OAC-1835673.

E. G. Puckett was supported by the National Science Foundation under Award ACI-1440811 as part of the SI2 Scientific Software Elements (SSE) program.

1  
2  
3  
4 38 *R. Gassmüller, H. Lokavarapu, W. Bangerth, E. G. Puckett*

5 The computational resources were provided by the Computational Infrastructure for Geo-  
6 dynamics. Computations were run on the distributed computing cluster Peloton of the U.C.  
7 Davis Division of Mathematical and Physical Sciences, and the Stampede2 system at the  
8 Texas Advanced Computing Center (TACC).  
9  
10  
11  
12  
13  
14

## 15 REFERENCES

- 16  
17 Bangerth, W., Dannberg, J., Gassmüller, R., Heister, T., et al., 2018. ASPECT: Advanced Solver for  
18 Problems in Earth's ConvecTion, User Manual, doi:10.6084/m9.figshare.4865333.  
19  
20 Bercovier, M. & Pironneau, O., 1979. Error estimates for finite element method solution of the stokes  
21 problem in the primitive variables, *Numerische Mathematik*, **33**(2), 211–224.  
22  
23 Brenner, S. & Scott, R., 2007. *The mathematical theory of finite element methods*, vol. 15, Springer  
24 Science & Business Media.  
25  
26 Brooks, A. N. & Hughes, T. J., 1982. Streamline upwind/petrov-galerkin formulations for convection  
27 dominated flows with particular emphasis on the incompressible navier-stokes equations, *Computer*  
28 *methods in applied mechanics and engineering*, **32**(1-3), 199–259.  
29  
30 Dannberg, J. & Gassmüller, R., 2018. Chemical trends in ocean islands explained by plume–slab  
31 interaction, *Proceedings of the National Academy of Sciences*, **115**(17), 4351–4356.  
32  
33 Dannberg, J., Eilon, Z., Faul, U., Gassmüller, R., Moulik, P., & Myhill, R., 2017. The importance of  
34 grain size to mantle dynamics and seismological observations, *Geochemistry, Geophysics, Geosys-*  
35 *tems*, **18**(8), 3034–3061.  
36  
37 Deubelbeiss, Y. & Kaus, B., 2008. Comparison of eulerian and lagrangian numerical techniques for the  
38 stokes equations in the presence of strongly varying viscosity, *Physics of the Earth and Planetary*  
39 *Interiors*, **171**(1-4), 92–111.  
40  
41 Donea, J. & Huerta, A., 2003. *Finite element methods for flow problems*, John Wiley & Sons.  
42  
43 Duretz, T., May, D. A., Gerya, T. V., & Tackley, P. J., 2011. Discretization errors and free surface  
44 stabilization in the finite difference and marker-in-cell method for applied geodynamics: A numerical  
45 study, *Geochemistry, Geophysics, Geosystems*, **12**(7), Q07004.  
46  
47 Edwards, E. & Bridson, R., 2012. A high-order accurate particle-in-cell method, *International Journal*  
48 *for Numerical Methods in Engineering*, **90**(9), 1073–1088.  
49  
50 Evans, M. W., Harlow, F. H., & Bromberg, E., 1957. The particle-in-cell method for hydrodynamic  
51 calculations, Tech. rep., Los Alamos National Laboratory.  
52  
53 Fischer, R. & Gerya, T., 2016. Early earth plume-lid tectonics: A high-resolution 3d numerical mod-  
54 elling approach, *Journal of Geodynamics*, **100**, 198–214.  
55  
56 Gassmüller, R., Dannberg, J., Bredow, E., Steinberger, B., & Torsvik, T. H., 2016. Major influence  
57 of plume-ridge interaction, lithosphere thickness variations, and global mantle flow on hotspot  
58 volcanism—the example of tristan, *Geochemistry, Geophysics, Geosystems*, **17**(4), 1454–1479.  
59  
60

*Evaluating hybrid finite element mesh/particle-in-cell methods* 39

- Gassmüller, R., Lokavarapu, H., Heien, E., Puckett, E. G., & Bangerth, W., 2018. Flexible and scalable particle-in-cell methods with adaptive mesh refinement for geodynamic computations, *Geochemistry, Geophysics, Geosystems*, **19**(9), 3596–3604.
- Gerya, T., 2009. *Introduction to numerical geodynamic modelling*, Cambridge University Press.
- Gerya, T. V. & Yuen, D. A., 2003. Characteristics-based marker-in-cell method with conservative finite-differences schemes for modeling geological flows with strongly variable transport properties, *Physics of the Earth and Planetary Interiors*, **140**(4), 293–318.
- Gilbarg, D. & Trudinger, N. S., 1983. *Elliptic Partial Differential Equations of Second Order*, Springer, Heidelberg, 2nd edn.
- Guermond, J.-L. & Pasquetti, R., 2011. Entropy viscosity method for high-order approximations of conservation laws, in *Spectral and high order methods for partial differential equations*, pp. 411–418, Springer.
- Harlow, F. H. & Welch, J. E., 1965. Numerical calculation of time-dependent viscous incompressible flow of fluid with free surface, *The Physics of Fluids*, **8**(12), 2182–2189.
- Heister, T., Dannberg, J., Gassmüller, R., & Bangerth, W., 2017. High accuracy mantle convection simulation through modern numerical methods – II: Realistic models and problems, *Geophys. J. Int.*, **210**(2), 833–851.
- Hirt, C. W. & Nichols, B. D., 1981. Volume of fluid (VOF) method for the dynamics of free boundaries, *Journal of Computational Physics*, **39**(1), 201–225.
- Ismail-Zadeh, A. & Tackley, P., 2010. *Computational methods for geodynamics*, Cambridge University Press.
- Kronbichler, M., Heister, T., & Bangerth, W., 2012. High accuracy mantle convection simulation through modern numerical methods, *Geophysical Journal International*, **191**(1), 12–29.
- McNamara, A. K. & Zhong, S., 2004. Thermochemical structures within a spherical mantle: Superplumes or piles?, *Journal of Geophysical Research*, **109**(B7), 1–14.
- McNamara, A. K. & Zhong, S., 2005. Thermochemical structures beneath Africa and the Pacific Ocean, *Nature*, **437**(7062), 1136.
- Meyer, D. & Jenny, P., 2004. Conservative velocity interpolation for pdf methods, in *PAMM: Proceedings in Applied Mathematics and Mechanics*, vol. 4, pp. 466–467, Wiley Online Library.
- Moresi, L., Dufour, F., & Muhlhaus, H. B., 2003. A Lagrangian integration point finite element method for large deformation modeling of viscoelastic geomaterials, *Journal of Computational Physics*, **184**, 476–497.
- Mulyukova, E. & Bercovici, D., 2018. Collapse of passive margins by lithospheric damage and plunging grain size, *Earth and Planetary Science Letters*, **484**, 341–352.
- Poliakov, A. & Podladchikov, Y., 1992. Diapirism and topography, *Geophysical Journal International*, **109**(3), 553–564.
- Popov, A. A. & Sobolev, S. V., 2008. SLIM3D: A tool for three-dimensional thermomechanical modeling

1  
2  
3  
4 40 *R. Gassmöller, H. Lokavarapu, W. Bangerth, E. G. Puckett*

5 of lithospheric deformation with elasto-visco-plastic rheology, *Physics of the Earth and Planetary*  
6 *Interiors*, **171**, 55–75.

7  
8  
9 Puckett, E. G., Turcotte, D. L., Kellogg, L. H., He, Y., Robey, J. M., & Lokavarapu, H., 2017. New  
10 numerical approaches for modeling thermochemical convection in a compositionally stratified fluid,  
11 *arXiv preprint arXiv:1703.02202*.

12  
13 Pusok, A. E., Kaus, B. J., & Popov, A. A., 2017. On the quality of velocity interpolation schemes for  
14 marker-in-cell method and staggered grids, *Pure and Applied Geophysics*, **174**(3), 1071–1089.

15  
16 Revenaugh, J. & Parsons, B., 1987. Dynamic topography and gravity anomalies for fluid layers whose  
17 viscosity varies exponentially with depth, *Geophysical Journal International*, **90**(2), 349–368.

18  
19 Rozel, A., Ricard, Y., & Bercovici, D., 2011. A thermodynamically self-consistent damage equation for  
20 grain size evolution during dynamic recrystallization, *Geophysical Journal International*, **184**(2),  
21 719–728.

22  
23 Samuel, H., 2018. A deformable particle-in-cell method for advective transport in geodynamic mod-  
24 elling, *Geophysical Journal International*, **214**(3), 1744–1773.

25  
26 Schubert, G., Turcotte, D. L., & Olson, P., 2001. *Mantle Convection in the Earth and Planets, Part*  
27 *1*, Cambridge University Press.

28  
29 Tackley, P. J., 1998. Thermo-chemical basal boundary layer: D"?, *The core-mantle boundary region*,  
30 p. 231.

31  
32 Tackley, P. J. & King, S. D., 2003. Testing the tracer ratio method for modeling active compositional  
33 fields in mantle convection simulations, *Geochemistry, Geophysics, Geosystems*, **4**(4).

34  
35 Taylor, C. & Hood, P., 1973. A numerical solution of the Navier-Stokes equations using the finite  
36 element technique, *Computers & Fluids*, **1**(1), 73–100.

37  
38 Thielmann, M., May, D. A., & Kaus, B. J. P., 2014. Discretization errors in the hybrid finite element  
39 particle-in-cell method, *Pure and Applied Geophysics*, **171**(9), 2165–2184.

40  
41 Thielmann, M., Rozel, A., Kaus, B., & Ricard, Y., 2015. Intermediate-depth earthquake generation and  
42 shear zone formation caused by grain size reduction and shear heating, *Geology*, **43**(9), 791–794.

43  
44 van Keken, P. E., King, S. D., Schmeling, H., Christensen, U. R., Neumeister, D., & Doin, M.-P., 1997.  
45 A comparison of methods for the modeling of thermochemical convection, *Journal of Geophysical*  
46 *Research: Solid Earth*, **102**(B10), 22477–22495.

47  
48 Wang, H., Agrusta, R., & Hunen, J., 2015. Advantages of a conservative velocity interpolation (CVI)  
49 scheme for particle-in-cell methods with application in geodynamic modeling, *Geochemistry, Geo-*  
50 *physics, Geosystems*, **16**(6).

51  
52 Zhong, S., 1996. Analytic solutions for Stokes' flow with lateral variations in viscosity, *Geophysical*  
53 *Journal International*, **124**(1), 18–28.  
54  
55  
56  
57  
58  
59  
60



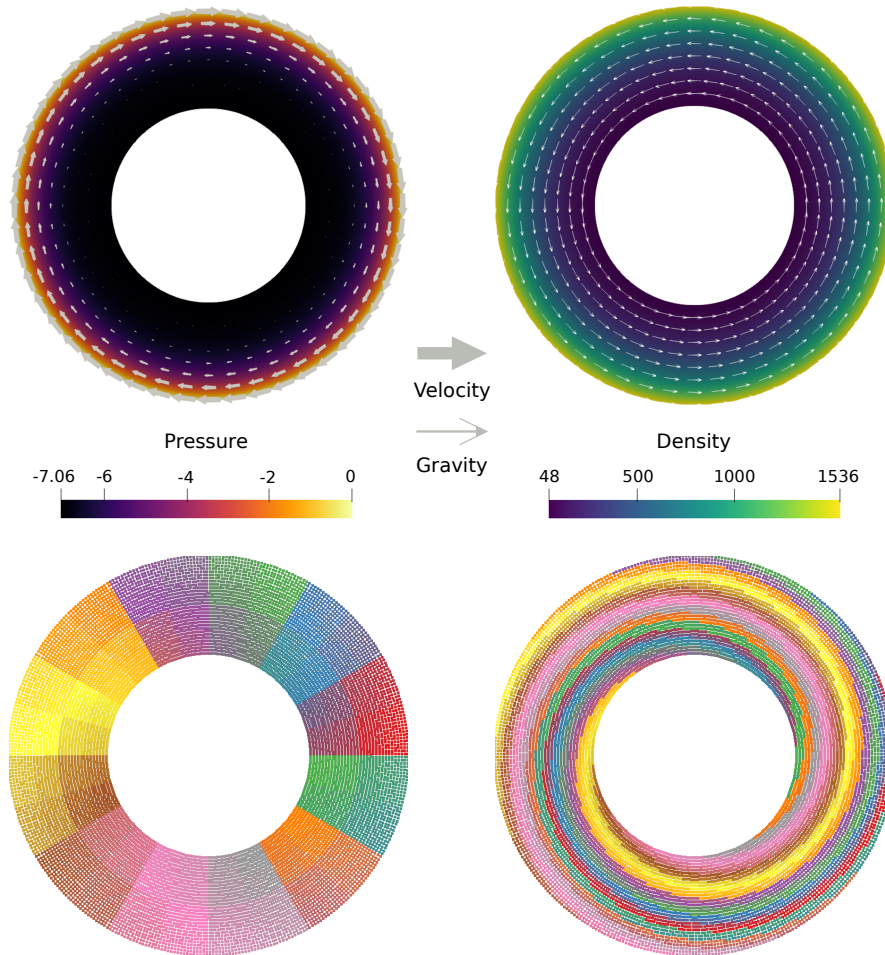


**Figure A1.** Solution of the annular flow benchmark. Top left: The velocity and pressure solution of the benchmark. Top right: Density and gravity fields that determine the right hand side of the Stokes system. Bottom row: Initial and final particle distributions after one full revolution of the outer edge, colored by particle index.

## APPENDIX A: DERIVATION OF AN INCOMPRESSIBLE STOKES SOLUTION ON AN ANNULUS

In order to derive the solution of the Stokes problem discussed in Section 5.1, we consider the Stokes equations (1)–(2) in polar coordinates. Since we will impose Dirichlet boundary conditions along all boundaries, and since we only consider an isoviscous fluid with  $\eta = 1$ , the equations can be simplified to

$$-\Delta \mathbf{u} + \nabla p = \rho \mathbf{g}, \quad (\text{A.1})$$

$$\nabla \cdot \mathbf{u} = 0. \quad (\text{A.2})$$

In a polar coordinate system with  $r = \sqrt{x^2 + y^2}$  and  $\theta = \arctan \frac{y}{x}$ , we can express the

42 *R. Gassmöller, H. Lokavarapu, W. Bangerth, E. G. Puckett*

Laplace operator, gradient, and divergence operators in terms of  $\frac{\partial}{\partial r}$  and  $\frac{\partial}{\partial \theta}$ . The incompressible Stokes equations (A.1) and (A.2) then become

$$\begin{aligned} & -\left(\frac{\partial^2 u_r}{\partial r^2} + \frac{1}{r} \frac{\partial u_r}{\partial r} + \frac{1}{r^2} \frac{\partial^2 u_r}{\partial \theta^2} - \frac{1}{r^2} u_r \right. \\ & \quad \left. - \frac{2}{r^2} \frac{\partial u_\theta}{\partial \theta}\right) + \frac{\partial p}{\partial r} = \rho g_r, \end{aligned}$$

$$\begin{aligned} & -\left(\frac{\partial^2 u_r}{\partial r^2} + \frac{1}{r} \frac{\partial u_r}{\partial r} + \frac{1}{r^2} \frac{\partial^2 u_r}{\partial \theta^2} - \frac{1}{r^2} u_r \right. \\ & \quad \left. - \frac{2}{r^2} \frac{\partial u_\theta}{\partial \theta}\right) + \frac{\partial p}{\partial r} = \rho g_r, \end{aligned} \tag{A.3}$$

$$\begin{aligned} & -\left(\frac{\partial^2 u_\theta}{\partial r^2} + \frac{1}{r} \frac{\partial u_\theta}{\partial r} + \frac{1}{r^2} \frac{\partial^2 u_\theta}{\partial \theta^2} - \frac{1}{r^2} u_\theta \right. \\ & \quad \left. + \frac{2}{r^2} \frac{\partial u_r}{\partial \theta}\right) + \frac{1}{r} \frac{\partial p}{\partial \theta} = \rho g_\theta, \end{aligned}$$

$$\begin{aligned} & -\left(\frac{\partial^2 u_\theta}{\partial r^2} + \frac{1}{r} \frac{\partial u_\theta}{\partial r} + \frac{1}{r^2} \frac{\partial^2 u_\theta}{\partial \theta^2} - \frac{1}{r^2} u_\theta \right. \\ & \quad \left. + \frac{2}{r^2} \frac{\partial u_r}{\partial \theta}\right) + \frac{1}{r} \frac{\partial p}{\partial \theta} = \rho g_\theta, \end{aligned} \tag{A.4}$$

$$\frac{1}{r} \frac{\partial(r u_r)}{\partial r} + \frac{1}{r} \frac{\partial u_\theta}{\partial \theta} = 0. \tag{A.5}$$

We can find a solution by introducing the “stream function”  $\psi(r, \theta)$ , and expressing the velocity through it:

$$u_r = \frac{1}{r} \frac{\partial \psi}{\partial \theta} \quad \text{and} \quad u_\theta = -\frac{\partial \psi}{\partial r}. \tag{A.6}$$

By this construction, the velocity field  $\mathbf{u}$  then automatically satisfies the continuity equation (A.5).

We proceed by assuming that the the stream function is separable, i.e., that it can be expressed in the form  $\psi(r, \theta) = F(r)G(\theta)$  for functions  $F, G$  still to be determined. This form then immediately implies  $u_r = \frac{1}{r} F(r)G'(\theta)$  and  $u_\theta = -F'(r)G(\theta)$ . Thus, equations (A.3) and (A.4) become

$$\begin{aligned} & -\left(\frac{1}{r} F'' G' + \frac{1}{r^2} F' G' + \frac{1}{r^3} F G' + \frac{1}{r^3} F G''' \right. \\ & \quad \left. - \frac{1}{r^3} F G' + \frac{2}{r^2} F' G'\right) = -\frac{\partial p}{\partial r} + \rho g_r, \end{aligned}$$

Evaluating hybrid finite element mesh/particle-in-cell methods 43

$$\underbrace{-\left(\frac{1}{r}F''G' + \frac{1}{r^2}F'G' + \frac{1}{r^3}FG'\right)}_{\text{blue wavy}} + \underbrace{\frac{1}{r^3}FG''' - \frac{1}{r^3}FG' + \frac{2}{r^2}F'G'}_{\text{blue wavy}} = -\frac{\partial p}{\partial r} + \rho g_r, \quad (\text{A.7})$$

$$\underbrace{-\left(-F'''G - \frac{1}{r}F''G - \frac{1}{r^2}F'G'' + \frac{1}{r^2}F'G\right)}_{\text{red wavy}} + \underbrace{\frac{2}{r^3}FG''}_{\text{red wavy}} = -\frac{1}{r}\frac{\partial p}{\partial \theta} + \rho g_\theta.$$

$$\underbrace{-\left(-F'''G - \frac{1}{r}F''G - \frac{1}{r^2}F'G''\right)}_{\text{blue wavy}} + \underbrace{\frac{1}{r^2}F'G + \frac{2}{r^3}FG''}_{\text{blue wavy}} = -\frac{1}{r}\frac{\partial p}{\partial \theta} + \rho g_\theta. \quad (\text{A.8})$$

We can obtain a solution of this set of equations in the spirit of manufactured solutions by choosing  $F(r) = \frac{1}{8c}r^8$  and  $G(\theta) = c$  where  $c$  can be any nonzero constant. This corresponds to a flow field with no radial component  $u_r = 0$  and a constant (but radially variable) angular velocity  $u_\theta = -r^7$ . Since  $F$  and  $G$  always appear as a product,  $c$  can be chosen arbitrarily and we will set it to  $c = 1$ .

Using this form then still requires us to find appropriate expressions for the pressure  $p(r, \theta)$ , the density  $\rho(r, \theta)$ , and the gravity vector  $\mathbf{g} = (g_r, g_\theta)$  to satisfy the governing equations. Since  $\rho$  only appears in a product with the gravity vector, we set

$$\rho(r, \theta) = 48r^5, \quad (\text{A.9})$$

ensuring that it is spatially variable but constant along streamlines.

Further substituting all of these expressions into (A.7)–(A.8) then yields

$$0 = -\frac{\partial p}{\partial r} + 48r^5 g_r, \quad (\text{A.10})$$

$$48r^5 = -\frac{1}{r}\frac{\partial p}{\partial \theta} + 48r^5 g_\theta. \quad (\text{A.11})$$

If we assume a radially outward gravity component  $g_r = \frac{r^3}{384}$ , this implies that

$$0 = -\frac{\partial p}{\partial r} + \frac{r^8}{8}. \quad (\text{A.12})$$

Integrating with respect to  $r$  and normalizing the pressure such that at the outer boundary  $r = R_2 = 2$  we have  $p(r = R_2, \theta) = 0$ , yields

$$p(r, \theta) = \frac{r^9}{72} - \frac{512}{72}. \quad (\text{A.13})$$

44 *R. Gassmöller, H. Lokavarapu, W. Bangerth, E. G. Puckett*

Given this pressure, the final remaining equation, (A.11), is

$$48r^5 = 48r^5 g_\theta. \quad (\text{A.14})$$

This results in  $g_\theta = 1$ .

In summary, our constructed solution is as follows:

$$\mathbf{u} = \begin{bmatrix} 0 \\ -r^7 \end{bmatrix}, \quad (\text{A.15})$$

$$p = \frac{r^9}{72} - \frac{512}{72}, \quad (\text{A.16})$$

$$\rho = 48r^5, \quad (\text{A.17})$$

$$\mathbf{g} = \begin{bmatrix} r^3 \\ \frac{384}{1} \end{bmatrix}. \quad (\text{A.18})$$

## APPENDIX B: DERIVATION OF AN INCOMPRESSIBLE STOKES SOLUTION IN A BOX

In order to derive the solution of the Stokes problem discussed in Section 5.1, we consider the Stokes equations (1)–(2) in Cartesian coordinates. As before, we only consider an isoviscous fluid with  $\eta = 1$ . The equations are then

$$-\Delta \mathbf{u} + \nabla p = \rho \mathbf{g}, \quad (\text{B.1})$$

$$\nabla \cdot \mathbf{u} = 0. \quad (\text{B.2})$$

We find a solution by introducing a variation of a previously described stream function  $\psi(x, y) = \frac{1}{\pi} \sin(\pi x) \sin(\pi y)$  [van Keken et al.(1997), Samuel(2018)], and expressing the velocity through it:

$$u_x = \frac{\partial \psi}{\partial y} = \sin(\pi x) \cos(\pi y) \quad (\text{B.3})$$

$$u_y = -\frac{\partial \psi}{\partial x} = -\cos(\pi x) \sin(\pi y). \quad (\text{B.4})$$

Using this construction, the velocity field  $\mathbf{u}$  automatically satisfies the continuity equation (B.2), is tangential to all boundaries of a unit box, and contains both shear and rotational components.

Completing the solution then requires us to find appropriate expressions for the pressure  $p(x, y)$ , the density  $\rho(x, y)$ , and the gravity vector  $\mathbf{g} = (g_x, g_y)$  to satisfy the governing equations. Since there are two equations to satisfy ( $x$  and  $y$  component of (B.1)), but four functions to choose, we can choose two of these functions arbitrarily. As for the spherical case, because

## Evaluating hybrid finite element mesh/particle-in-cell methods 45

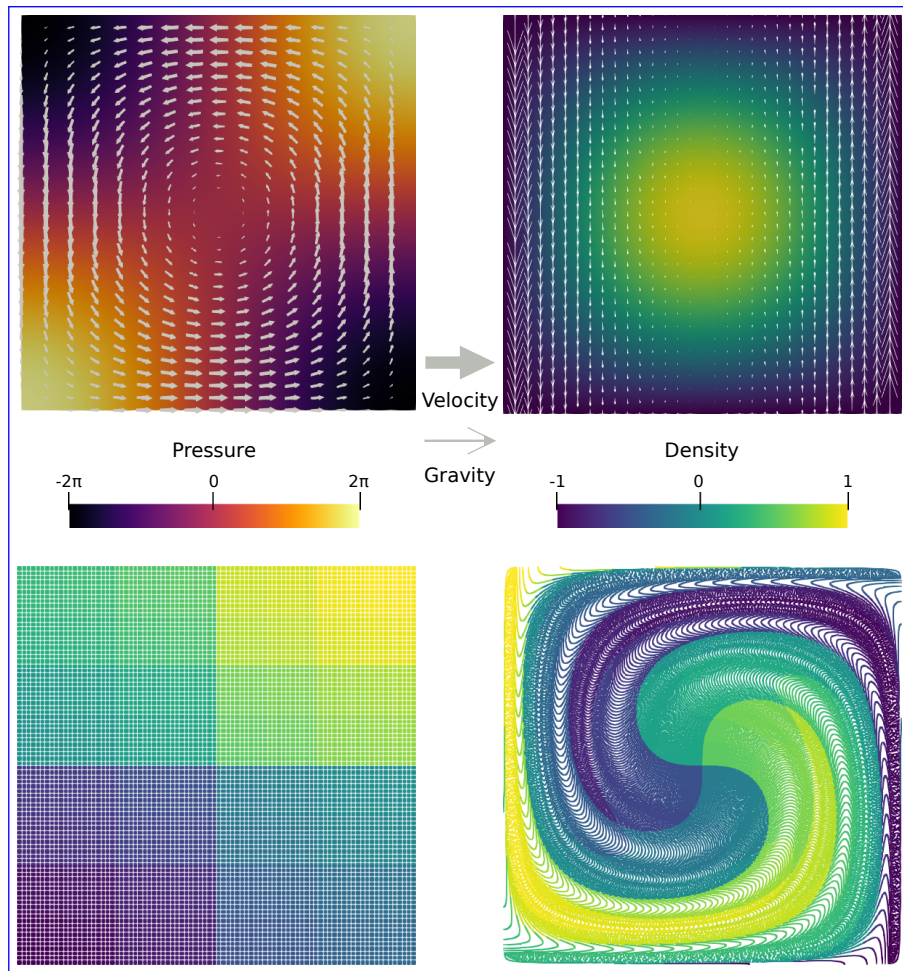


**Figure A2.** Solution of the rigid shear benchmark. Top left: The velocity and pressure solution of the benchmark. Top right: Density and gravity fields that determine the right hand side of the Stokes system. Bottom row: Initial ( $t = 0$ ) and final particle distributions after one full revolution of the center ( $t = 2$ ), colored by particle index.

we want the benchmark to be stationary, we choose a density  $\rho(x, y)$  that is constant along streamlines, and for convenience we choose  $\rho(x, y) = \pi\psi(x, y) = \sin(\pi x) \sin(\pi y)$ . Additionally, we arbitrarily set  $g_x = 0$ . Substituting all of these expressions into (A.1) then yields

$$\underline{2\pi^2 \sin(\pi x) \cos(\pi y) + \frac{\partial p}{\partial x} = 0,} \quad (\text{B.5})$$

$$\underline{-2\pi^2 \cos(\pi x) \sin(\pi y) + \frac{\partial p}{\partial y} = \rho g_y,} \quad (\text{B.6})$$

and integrating (B.5) for  $x$  gives us the pressure:

$$\underline{p(x, y) = 2\pi \cos(\pi x) \cos(\pi y) + c.} \quad (\text{B.7})$$

Similarly, differentiating (B.7) and substituting in (B.6) results in the  $y$ -component of gravity:

46 *R. Gassmöller, H. Lokavarapu, W. Bangerth, E. G. Puckett*

$$g_y = -4\pi^2 \frac{\cos(\pi x)}{\sin(\pi x)}. \quad (\text{B.8})$$

In summary, our constructed solution is as follows:

$$\underline{u} = \begin{bmatrix} \sin(\pi x) \cos(\pi y) \\ -\cos(\pi x) \sin(\pi y) \end{bmatrix}, \quad (\text{B.9})$$

$$p = 2\pi \cos(\pi x) \cos(\pi y), \quad (\text{B.10})$$

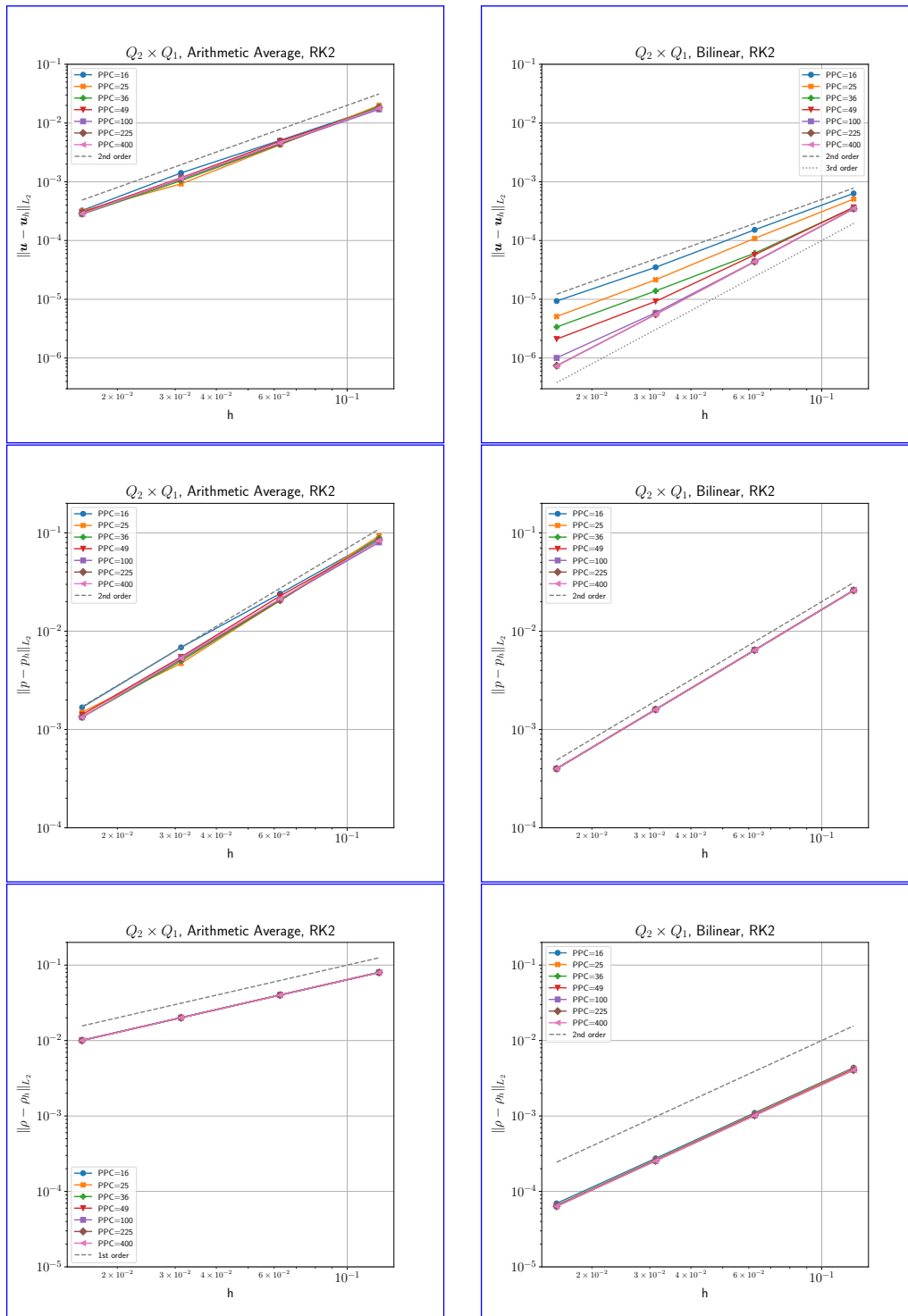
$$\rho = \sin(\pi x) \sin(\pi y), \quad (\text{B.11})$$

$$\underline{g} = \begin{bmatrix} 0 \\ -4\pi^2 \frac{\cos(\pi x)}{\sin(\pi x)} \end{bmatrix}. \quad (\text{B.12})$$

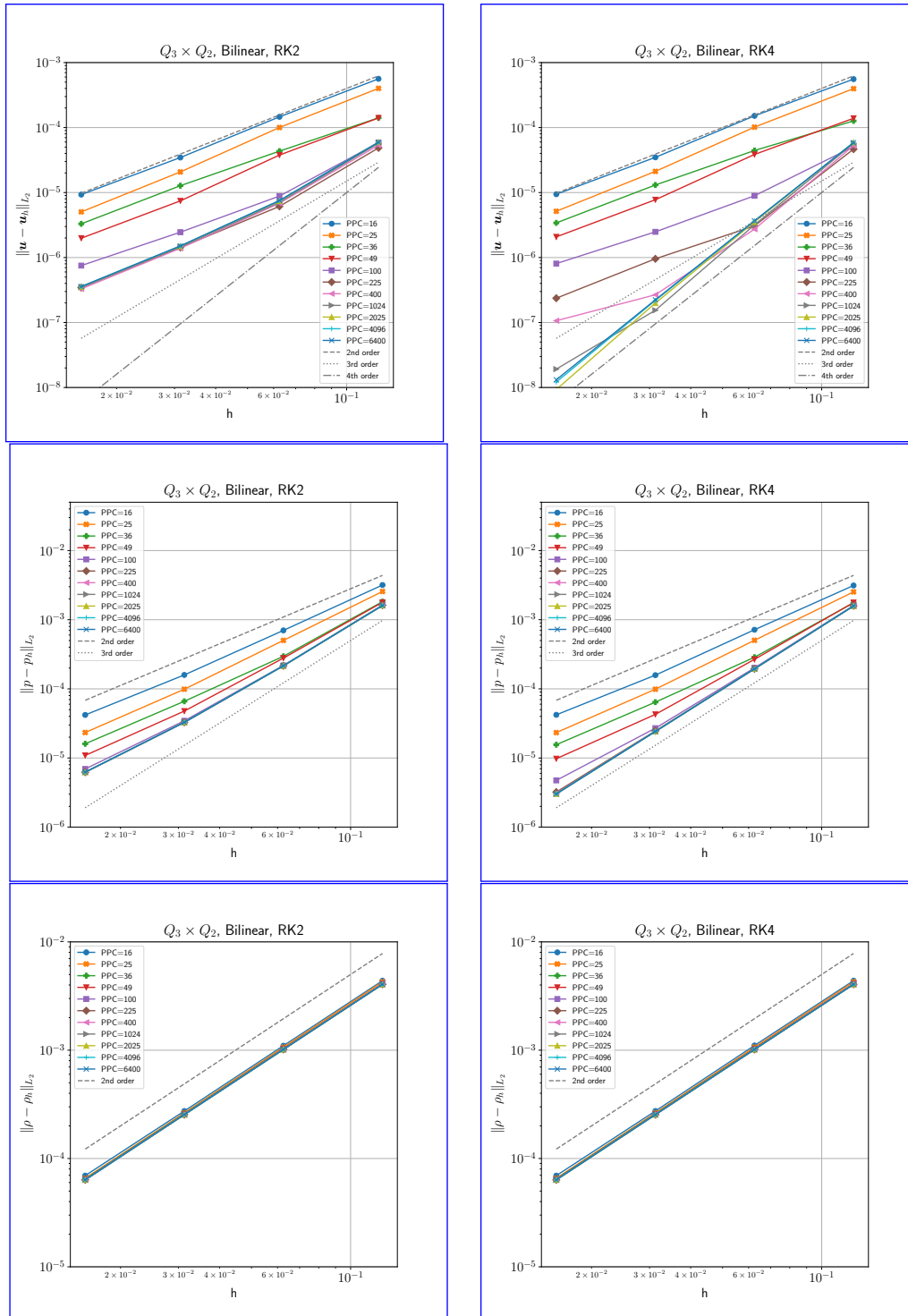
## APPENDIX C: RESULTS OF THE TIME DEPENDENT BOX BENCHMARK

Figure A3 and Figure A4 present results for this second time-dependent benchmark, using an identical layout as for the spherical annulus case. Despite the changed geometry and different model solution, all measured convergence rates are consistent with the model of Section 5.1.

Evaluating hybrid finite element mesh/particle-in-cell methods 47



**Figure A3.** The convergence rate of  $\|u - u_h\|_{L_2}$  (top),  $\|p - p_h\|_{L_2}$  (middle), and  $\|\rho - \rho_h\|_{L_2}$  (bottom) measured at  $t = 0.1$  for the time dependent box benchmark. Density is carried on particles and is interpolated as cell-wise arithmetic average ( $r = 1$ , left) and bilinear least-squares interpolation ( $r = 2$ , right). All models use a  $Q_2 \times Q_1$  element ( $k = 2$ ) and RK2 to advect particles. Note that only with bilinear least-squares interpolation and an increasing number of particles per cell ( $PPC$ ) is the third order convergence rate of velocity recovered. In all cases,  $\|p - p_h\|_{L_2}$  converges at second-order rate with no apparent influence due to the number of  $PPC$  (i.e., all dots fall on each other), while the convergence rate of  $\|\rho - \rho_h\|_{L_2}$  depends on the interpolation scheme, but not on  $PPC$ .

48 *R. Gassmüller, H. Lokavarapu, W. Bangerth, E. G. Puckett*

**Figure A4.** Panels as in Fig. A3, but for a  $Q_3 \times Q_2$  element ( $k = 3$ ). All models use the bilinear least squares interpolation ( $r = 2$ ). Columns represent RK2 (left) and RK4 (right) particle integration. Note that only with RK4, bilinear least-squares interpolation and an increasing number of particles per cell ( $PPC$ ) is the fourth order convergence rate of the velocity recovered. All properties with a design convergence rate higher than 2 require an increasing  $PPC$  to reach their design rate, while constant  $PPC$  only allows for second order convergence. The density is limited to second-order accuracy due to the chosen interpolation scheme ( $r = 2$ ).